OPTIMIZATION OF IONIC TRANSPORT IN ELECTROCHEMICAL DEVICES

By

Janna Marie Rathert

Dissertation

Submitted to the Faculty of the

Graduate School of Vanderbilt University

in partial fulfillment of the requirements

for the degree of

DOCTOR OF PHILOSOPHY

in

Mechanical Engineering

June 30, 2022

Nashville, Tennessee

Approved:

Jason G. Valentine, Ph.D.

Cary L. Pint, Ph.D.

Sharon M. Weiss, Ph.D.

David E. Cliffel, Ph.D.

Joshua D. Caldwell, Ph.D.

ACKNOWLEDGMENTS

This one's for you, Mom and Dad. Thank you for watering me, tending the vines, and making strong wine from a bold grape. Thank you also to my brother, Myles, and his partner, Jen, for being there to celebrate my successes and console me in my failures.

Thank you to the National Science Foundation for financial support under the Graduate Research Fellowship.

Thank you to Cary Pint for seeing something in me and for taking a chance in bringing me to Vanderbilt. You fought for me at every turn, even when it wasn't easy.

Thank you to Jason Valentine for adopting me into your group and broadening my horizons. I hope this makes you proud.

Thank you to Sharon Weiss, David Cliffel, and Josh Caldwell for taking the time out of your busy schedules to support me in my graduate career as a part of my committee. I hope we stay in touch for a long time.

Thank you to Sarah Ross and the rest of the VINSE staff for building a community I couldn't do without.

Thank you to Larry Cox and Barry Templeton for helping me to keep my electrochemistry space until the work was done.

Thank you to my labmates, past and present, for tolerating me in my least appealing moments. Special thanks to Kate Moyer and Elena Kovalik, my unstoppable partners in crime.

Thank you to Emily Matijevich for bringing me to Vanderbilt for the first time and giving me a chance to fall in love. I'm grateful to you for sharing your social circle and introducing me to a strong support network of lifelong friends.

Most of all, I am eternally grateful to be adored by Timothy Rathert, husband and cat dad. This program has tested our vows, as together we endured much of the "hardship" in "prosperity and hardship," but you never wavered. You shared your big, loving family with me and gave me a home away from home. You are the most hilarious, analytical, talented person I know. Thank you for all the little things you do to keep me sane and humble.

TABLE OF CONTENTS

LIST OF FIGURES

Chapter 1: Introduction

1.1. Motivation

The rapid increase in atmospheric greenhouse gas concentrations due to anthropogenic emissions poses imminent threats to Earth's climate system and its most vulnerable communities. There is no panacea for climate change; instead, a comprehensive approach is required, with sweeping policy changes and technological innovations to reform the way we generate, distribute, and use energy.

The implementation of renewable energy is widely regarded as an effective method of reducing CO_2 emissions. In 2020, renewable energy sources accounted for just 20% of all energy generation in the United States.[1] This number does not reflect the availability of renewable resources, in fact, less than 10,000 square miles of solar arrays alone would be sufficient to power the entire U.S. over a year.[2] Rather, it reflects the costs and challenges of integrating renewables into the power grid and the transportation sector.[3] The intermittent nature of wind and solar can introduce instability into power systems which is exacerbated at higher concentrations. Using energy storage for load-leveling plays a key role in increasing penetration of intermittent renewable energy generators into both the electrical grid and vehicle fleet.[4]

In addition to establishing sustainable methods of power generation and delivery, reduced power consumption is critical to any comprehensive approach to minimizing greenhouse gas emissions. Although certain corporations have attempted to offload this responsibility onto individual consumers, urging families to turn off the lights and recycle plastics, the amount of U.S. carbon emissions attributed to any individual is just 3×10^{-7} %.[5] On the other hand, innovation of efficient devices and systems can have a significant global impact.

1.2. Introduction to Electrochemistry

Electrochemical methods are a broad collection of techniques that involve the relationship between electrical energy and chemical reactions. In general, an electrochemical cell includes an ionically-conducting electrolyte, a barrier to force electrons around an external circuit, and at least two electrodes.

Under conditions where there is no charge transfer across the electrode interface, the process is non-faradaic. Energy is stored by a buildup of charge at the electrode interface in response to an applied bias, rather than in a chemical reaction. This behavior is analogous to charging a capacitor and has been leveraged for rapid energy storage and delivery, as in electrochemical supercapacitors.

When electrons are transferred across the electrode interface, the process is known as faradaic. For a faradaic process, the equilibrium cell potential describes the energy available to drive charge from one electrode to the other. It depends upon the change in Gibbs free energy, ΔG, between the initial and final states, as well as temperature (T), charge (n), and the relative thermodynamic activities (a) of reactant and product. Adding

additional energy to the system via external bias will shift the equilibrium between reactants and products, dictating a change in activity, or concentration, as defined by the Nernst Equation:

$$E = \frac{\Delta G}{-nF} + \frac{RT}{nF}\ln\left(\frac{a_O^{\nu_O}}{a_R^{\nu_R}}\right)$$

Equation 1

where ν is a stoichiometric coefficient[6]. When electrons are transferred, the valence state of the reduced species changes, usually influencing the bonding arrangement of molecules or compounds[7,8]. This could manifest as the transformation from a metal ion to a zerovalent metal solid, as in electrodeposition, or the incorporation of guest ions into a host matrix, as in alloying or intercalation

The rate of a heterogeneous reaction occurring at the electrode-electrolyte interface is reflected in the current density, *i*, which is related to the amount of reacted material by,

$$i = F\sum z_j N_j$$

Equation 2

where N_j is the molar flux of species *j*, z is the charge number of species *j*, and F is Faraday's constant.[9] The total current density is determined by contributions from mass transfer, electron transfer, reaction kinetics, and surface processes (e.g. adsorption). At steady-state, the rate of mass transfer is equal to the reaction kinetics, such that current density can be expressed in terms of two effective resistances in series:

$$i = \frac{1}{\frac{1}{n_s F k_m c_{R,b}} + \frac{1}{i_{O,b}\exp\left(\frac{\alpha_a F}{RT}\eta_s\right)}}$$

Equation 3

where the first term describes mass transfer and the second describes reaction kinetics.[9] Here, k_m is the mass transfer coefficient, $c_{R,b}$ is the concentration of reductants in the bulk, $i_{O,b}$ is the exchange current density, α_a is the anodic transfer coefficient, and η_s is the surface overpotential, which is the driving force for the reaction. In the limit of high overpotential, as in electrochemical devices operated at high rates, it follows that current is dominated by mass transport. In electrochemical systems, the contributions from ionic flux via migration, diffusion, and convection can be summed in the Nernst-Planck equation.

$$N_j = -z_j u_j F c_j \nabla\phi - D_j \nabla c_j + c_j v$$

Equation 4

The first term represents migration, where u_j is the mobility of species *j*, and $-z_j F c_j \nabla\phi$ is the force of an electric field on a charged species. The second term is derived from Fick's law, where the diffusivity, D, describes the rate of transport along a concentration gradient. The final term is for convection, where *v* is the

molar average velocity of a fluid in motion. Together with Equation 2, the Nernst-Planck equation gives the total electrical current.[9]

Power is given by the product of current and cell potential, equivalent to an amount of energy converted per unit time. It is often desirable to optimize the power consumption or power delivery of an electrochemical device. For example, an electric vehicle may require high power batteries to rapidly accelerate, though not at the expense of energy density or cycle life. At the other end of the spectrum, an eco-friendly sensor may be designed for low power consumption without sacrificing fast response rates. In this body of work, I seek to analyze the relationship between structure and reaction rates in electrochemical systems. I find that many of the devices in question demonstrate interesting behavior in the regime of high overpotential, where mass transport is the limiting rate step. I then implement engineering strategies to optimize electrochemical devices according to relevant metrics.

1.3. Sustainable Electrochemical Energy Storage

While energy storage comes in many forms, from pumped hydro to a pint of beer, electrochemical energy storage has enabled the safe, efficient electrification of vehicles and portable consumer devices. The considerable energy density of rechargeable lithium-ion batteries (LIBs) makes them the standard power source for cell phones, the Internet of Things, electric vehicles and more. However, to encourage uptake of renewable energy sources at home and on the road, battery costs must fall while energy density climbs, leading researchers to continue the pursuit of lithium (Li) metal batteries, next-generation lithium-sulfur and lithium-air chemistries, and "beyond-lithium" batteries utilizing the reversible migration of alternative elements, like sodium (Na) and magnesium (Mg).

In recent years, the rapid expansion of the LIB market has strained global supply chains,[10] an issue exacerbated by the fact that less than 5% of used LIBs make it to recycling centers.[11] Whereas it remains controversial to predict how this will impact LIB pack cost, the development of batteries utilizing alternative alkali and alkali-earth metals could improve the cost stability of raw materials under extreme scaling conditions. As the fourth most abundant element in the world, there exist over 47 billion tons of sodium precursor (soda ash) reserves worldwide, compared to only 62 million tons of lithium. In turn, sodium is a target for the extreme high volume scaling associated with penetration of grid-scale energy storage at residential levels.[12] Another promising alternative is magnesium, which is not only 300 times more abundant than lithium, but also stores nearly twice as much energy per volume (3833 mAh/cm^3 vs 2046 mAh/cm^3) due to its divalent charge.[13] This may be an attractive chemistry for space-limited applications, like augmented reality and other wearable devices. Considering the limited availability and geopolitical complications[10] of materials essential to LIB production, the development of both Na, Mg, and other alternative-ion batteries (i.e. K, Ca, Al) is important for ensuring clean energy security for years to come.

1.4. Using Less Energy: Electrochemistry for Low-Power Devices

Despite the plethora of recent advances in renewable energy, there is no substitute for simply consuming less. Photonics research is overflowing with opportunity for such energy-saving technologies. For example, state-of-the-art quantum computers have demonstrated five orders of magnitude less energy consumption than traditional supercomputers for equivalent operations [14]. Another recent illustration is the scalable formulation of metamaterials for radiative cooling during both day and night as a zero-energy alternative to air conditioning [15]. In an increasingly electrified world, innovation of energy-efficient systems is crucial to ensuring a sustainable future.

Electrochemistry and photonics go hand in hand. Their union led to the invention of the dye sensitized solar cell, artificial photosynthesis, and photocatalytic hydrogen generation, among other sustainable systems dedicated to the reduction of anthropogenic emissions. Inspired by these breakthrough technologies, I have applied my experience in electrochemical energy storage systems to the study of low-power active and adaptive metamaterials.

Metamaterials are made up of periodic arrays of scatterers with subwavelength dimensions called "meta-atoms" which independently manipulate the phase, amplitude, and polarization of passing wavelets in a way which depends principally upon geometry and effective permittivity, ε. For a metallic meta-atom much smaller than the free space wavelength, coupling to a localized surface plasmon resonance (LSPR) can impart an abrupt phase shift on the incoming light. In dielectric and semiconductor nanostructures, both magnetic and electric resonances are supported when a critical dimension is comparable to the wavelength of light inside the particle. In each case, the metamaterial is limited to interaction with a narrow band of incident electromagnetic energy by its geometry and material components[16].

As fabricated, geometry and permittivity are static properties, but it is often desirable to tune the scattered spectrum or intensity for a particular application. For this reason, metamaterials that actively respond to external stimulus are a burgeoning field of interest, particularly if they possess the property of self-adaptation. Adaptive metamaterials are a subset of active metamaterials that automatically adjust to the environment, either through a mechanism intrinsic to the structure[17–19], or through digital reconfiguration informed by external sensors[20,21].

From a mathematical standpoint, approaches to modulation can be separated into two categories: 1) mechanical reconfiguration of the geometry and arrangement of scatterers to induce a coordinate transformation of the phase profile; 2) manipulation of the optical properties of the scatterer or its environment for a resulting change in resonance frequency.[22] Although there are many paths to achieving modulation (i.e. liquid crystals[23,24], mechanical strain[25–27], electrostatic gating[28–30], phase change materials[31–33], etc.), electrochemistry is the only method that belongs to both categories of active metamaterials.

When applied to optical materials, electrochemical methods can trigger both electrical gating and phase change mechanisms to change the permittivity of a scattering nanostructure or its environment[34,35], while geometry of

nanostructures can be modified by electrodeposition and stripping[36] or volume changes of a host material in response to ion insertion[37]. The power of this technique is that large changes in carrier concentration are made possible by ionic diffusion and charge compensation, therein overcoming Debye screening effects[34].

Despite its many merits, electrochemistry has limitations when it comes to speed or refresh rates for photonic applications. Although charge compensation by ions at an interface can improve dynamic range, it typically necessitates the transport of ionic species to said interface. Depending on the properties of the electrolyte and electrode, such processes could take anywhere from milliseconds to days, but they cannot compete with the picosecond timescales of other approaches, like optical pumping[38]. For this reason, electrochemical modulation has not yet proven appropriate for telecommunications, although properly engineered systems, designed with principles of electrochemical transport in mind, may be well suited for applications like thermoregulation, stealth, encryption, sensing, or displays.

Given the widespread deployment of electronic displays to disseminate information, reflective displays are a promising alternative to their emissive counterparts for promoting energy savings. The power density of reflective technologies like e-paper can be reduced by an order of magnitude over OLED, LCD, and ELD screens[39], although a number of challenges remain. As a flexible platform for structural color generation, metamaterials are a promising approach to overcome limitations in brightness, contrast, chromaticity, resolution, and viewing angle.[40,41] In chapters 5 and 6, I apply engineering strategies to optimize mass transport in electrochemically actuated photonic devices, addressing issues of dynamic range, response time, and power consumption.

1.5. Outline

This dissertation is organized as follows:

Chapter 2 describes the complex interplay between kinetic and mass transport processes during the electrochemical deposition of metallic Mg for next-generation batteries. I uncover the relationship between sluggish diffusion and non-equilibrium growth morphologies that threaten cell safety. The overarching themes are relevant to electroplating of other multivalent metals.

Chapter 3 presents the upcycling of lead alloys from a used lead acid battery into a next-generation sodium-ion system for ultra-low-cost rechargeable batteries. Through evaluation of sodium storage capacity and rate capability, I unravel the rich interplay of alloy microstructure and properties which can be controlled through simple heat treatment of directly recycled electrodes to optimize power and cycle life.

Chapter 4 leverages the reversible electrochemical intercalation of lithium in TiO_2 to enable low-power, dynamic photonic devices with spectral shifts over 100 nm in the visible spectrum.

Chapter 5 evaluates opportunities for electrochemical, as well as photochemical, doping of TiO_2 nanoparticles to design tunable all-dielectric metasurfaces. The resulting devices achieve modulation depths up to 70% with

switching speeds on the order of 1 s and can be controlled using optical addressing.

Chapter 6 provides concluding statements.

Chapter 2: Kinetic versus Diffusion Driven Three-Dimensional Growth in Magnesium Metal Battery Anodes

2.1. Introduction

A key barrier toward realizing a high energy density Mg^{2+} battery has been the limited understanding of mechanisms governing multivalent metal electrodeposition. This, compounded with recent observations of Mg dendrites, highlights the need for better fundamental insight into multivalent systems. In this chapter, I present a comprehensive study of electrodeposition in practical coin cell configurations to evaluate the mechanisms of growth from common $Mg(TFSI)_2$-based electrolytes. I find that a transition from charge transfer-limited to diffusion-limited electrodeposition processes governs the morphological evolution of Mg deposits. My results highlight synergy with classical electrochemical theories for growth and lay groundwork for future approaches to achieve stable electroplated multivalent metal electrodes

2.2. Background

The defect that nearly destroyed the lithium battery following its debut – the dendrite – has been the target of persistent engineering efforts over the last forty years. In the area of lithium batteries, the transition to anodes incorporating metallic lithium has required researchers to identify, understand, prevent, eliminate, and most recently predict dendrites in batteries and this remains an ongoing area of rich scientific and applied interest.[42] Now, as researchers begin to venture from studying metallic lithium to alternative alkali and alkali-earth metal chemistries, the lessons learned regarding electrochemical nucleation and growth provide a blueprint from which to draw new ideas and direction. Of all alkali metals that have promise beyond lithium, magnesium stands out as it stores twice the volumetric energy as lithium, and it was originally lauded for enhanced safety over lithium when early studies suggested resistance to dendrite growth during electroplating.[43–45] These properties positioned magnesium rechargeable batteries (MRBs) as the ideal candidate for compact, high-performance energy storage systems relevant to electric vehicles, aerospace systems, or Internet of Things applications.

Although dendritic growth of Mg metal was reported by Gregory *et al* in 1990[46], recent studies from the Banerjee group and the Passerini group have reminded us that Mg metal dendrites remain a threat to the future of MRBs[47–49]. Despite strong evidence that dendrites exist, however, there remains controversy over the galvanostatic signature of failure in this and similar systems. With this said, common electrolytes for Mg electroplating such as the family of halogen-free electrolytes comprising magnesium bis(trifluoromethane sulfonyl)imide [$Mg(TFSI)_2$] in ether-based solvents, have been observed to exhibit galvanostatic transients featuring a high initial overpotential period which suddenly disappears after some duration.[47,50–53] Studies have shown that while $Mg(TFSI)_2$ is a popular electrolyte that is easily accessible and possesses excellent anodic stability (>3 V vs Mg/Mg^{2+}), it is also highly sensitive to contamination by water and prone to Mg surface

passivation.[51,54–57] In turn, early studies attributed the high overpotential to breakdown of such surface passivating films, likely under the assumption that Mg was resistant to dendrite formation during electroplating[43,44]. However, following recent observations of dendrite formation during Mg metal electroplating, there is a need to reevaluate growth mechanisms and understand the factors controlling non-equilibrium growth in halogen-free electrolytes.

To explain the mechanism for Mg dendrite formation, it has been shown that with high current density and poor surface properties, the electrochemical reaction rate can surpass the self-diffusion rate leading to dendritic growth of magnesium.[48,58] In addition, concentration gradients can be critical in dictating morphology, especially under constant current conditions so commonly used for the study of novel electrolytes and storage materials. Drawing a parallel to Li metal plating studies, it has been shown that electrolyte diffusion limitations are responsible for triggering the transition from root-growing mossy lithium to tip-growing dendritic lithium which penetrates separators to cause catastrophic failure.[59–63] In this area, recent work by the Dasgupta group used a combination of advanced galvanostatic techniques and microscopy to distinguish kinetic limited growth in early cycling of a Li-Li symmetric cell from mass-transport limited growth induced by accumulation of dead lithium in later cycles.[63,64] The transition from kinetic to mass-transfer limited growth is characterized by Sand's time, τ_{sand}, which proceeds as the inverse square of current density. For times greater than the Sand's time, onset and growth of ramified deposits are well-described by the models of Fleury, Chazalviel, Rosso, and colleagues, which expand upon the theory that dendrites result from diffusion limitations that create a space charge region.[65–67] Further, depletion of cations near the interface results in preferential deposition at regions of high curvature.[9,59,68,69] It is also possible to observe Sand-like behavior at unexpectedly low current densities due to inhomogeneities on the electrode surface causing local fluctuations in ion concentration.[69–71] 3D growth due to cation depletion can in turn be avoided by increasing the electrolyte concentration[72,73], pulse charging[74,75], or homogenizing ion flux[76–78].

Translating such ideas to Mg is challenging since existing studies of metallic magnesium electrodeposition either do not investigate the mechanistic underpinnings of shorting, or study processes in harsh Grignard reagents which are incompatible with conventional battery components, and purposely push the system to extreme limits.[48,49] In this article, we explore the regimes of the galvanostatic Mg metal electroplating curve and correlate voltage fluctuations to nucleation, growth, and shorting phenomena in practical coin cell configurations. Notably, our findings indicate that Mg metal nucleation and deposition from TFSI-based electrolytes does occur within the high polarization region previously attributed to Mg passivation layer breakdown, leading to eventual shorting of the cell. Our work shows that intermittent resting can modify the formation and growth of 3D Mg structures, supporting the hypothesis that slow Mg diffusion leads to partial electrolyte depletion at the substrate interface. Further, although there exist more liberal definitions of the term, we exercise the strict definition of "dendrite" as a fractal structure with well-defined branches in order to distinguish these from hemispherical deposits in describing magnesium morphologies deposited from halogen-free electrolytes, as the growth kinetics and prevention mechanisms are contradictory to those expected of

dendrites.

2.3. Experimental Methods

2.3.1. Electrochemical Testing

Galvanostatic testing was conducted in SS316 coin cells using an MTI BTS8-MA 8-channel Battery Analyzer using 0.1 M $Mg(TFSI)_2$ electrolyte in 1:1 v/v diglyme/dimethoxyethane. $Mg(TFSI)_2$ salt was purchased from Solvionic and dried under vacuum (1E-2 torr) overnight at 250°C. Diglyme and dimethoxyethane (Sigma Aldrich) were dried over 30% m/V molecular sieves for 48 hrs before electrolyte preparation in an argon glovebox (< 1 ppm O_2). Electrolytes were used within 48 hours of preparation. Electrolyte quality was assessed via cyclic voltammetry using polished Mg foil counter and reference electrodes, a polished Pt disc working electrode with diameter 0.25 mm, and a scan rate of 20 mV/s from -1 to 3V. The first cycle Coulombic efficiency was determined to be 32.6% with plating and stripping peak onsets of -0.65 V and 1.68 V, respectively (**Figure 1**). This result is consistent with other studies which measured water content less than 20 ppm.[79,80] For coin cells and three-electrode tee cells, 0.1 mm thick magnesium foil (MTI) was punched into 8 mm discs and polished using 220 grit, 400 grit, and 1000 grit sandpaper sequentially. Celgard™ 2325 trilayer separators were dried under vacuum overnight before inclusion in coin cells or tee cells. EIS was performed on coin cells prepared in the same manner using a Metrohm Autolab PG810 with FRA32M frequency response analyzer in the frequency range 0.1 MHz - 0.5 Hz with amplitude 10 mV.

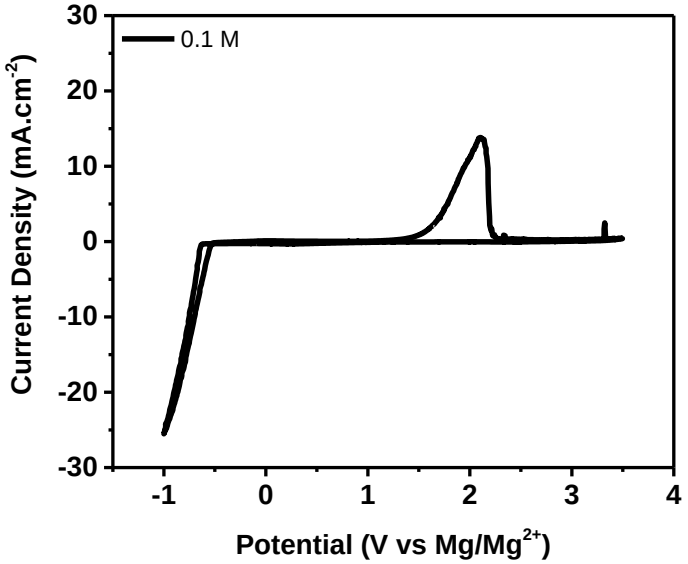

Figure 1: Cyclic voltammetry of 0.1 M Mg(TFSI)2 in 1:1 dimethyl ether:diglyme with Pt disc working electrode, polished Mg reference electrode, polished Mg counter electrode. Scan speed 20 mV/s.

2.3.2. Morphological Analysis

Coin cells were de-crimped, the electrode or separator of interest rinsed twice in dry DME, and stored in a sealed vial for transport to SEM. Samples were exposed to air during transfer. Imaging was conducted using a Zeiss Merlin SEM with EDS detector.

2.3.3. Measurement of Diffusion Coefficient

A potential step experiment was performed in a sealed, flooded, 3-electrode cell using polished Mg foil counter and reference electrodes, a polished Pt disc working electrode with diameter 0.25 mm. The voltage was set to -0.5 V vs Mg/Mg^{2+} for 300 s, then the resulting current was integrated over time to produce a line with slope related to the diffusion coefficient as defined by the Cottrell Equation:[68,81]

$$i(t) = \frac{nFAD_O^{\frac{1}{2}}C_O^*}{\pi^{\frac{1}{2}}}\left(\frac{1}{t^{\frac{1}{2}}}\right)$$

Equation 5

The transference number is extrapolated from data acquired by Sa *et al* using atomic absorption spectroscopy for t_+ vs concentration of $Mg(TFSI)_2$ in diglyme with a standard deviation of 0.108.

2.4. Results and Discussion

2.4.1. Electrodeposition Behavior in Mg Symmetric Cells

In recent years, multiple reports have demonstrated the electroplating of Mg metal onto surfaces using galvanostatic methods with very similar electrochemical responses.[47,50–53] The first step in our study was therefore to evaluate the electroplating behavior of Mg metal batteries under constant current discharge testing. The shape of a typical galvanostatic electroplating curve for a Mg/Mg symmetric cell is depicted in **Figure 2**a. Notable features include an initial spike followed by a period of negative potential which abruptly jumps to almost 0 V after some duration. Although the precise origin is unclear, the magnitude of the high overpotential plateau has been shown to be sensitive to a number of factors, including anode/cathode surface characteristics[54,55], electrolyte concentration[80,81], or contamination due to water.[54,79] Its sudden disappearance has been previously attributed to the first instance of magnesium stripping from an inhomogeneously passivated anode[50,52] or from the sudden removal of adsorbed species at the Mg-electrolyte interface which are overcome in the presence of large bias.[51,53,55] However, recent observations of Mg dendrites[47,48] invite a third possible interpretation of this behavior; it is therefore hypothesized that stripping and plating begin with the onset of applied current and proceed throughout the plateau until three-dimensional growth reaches the counter electrode, creating a short circuit. (**Figure 2**b)

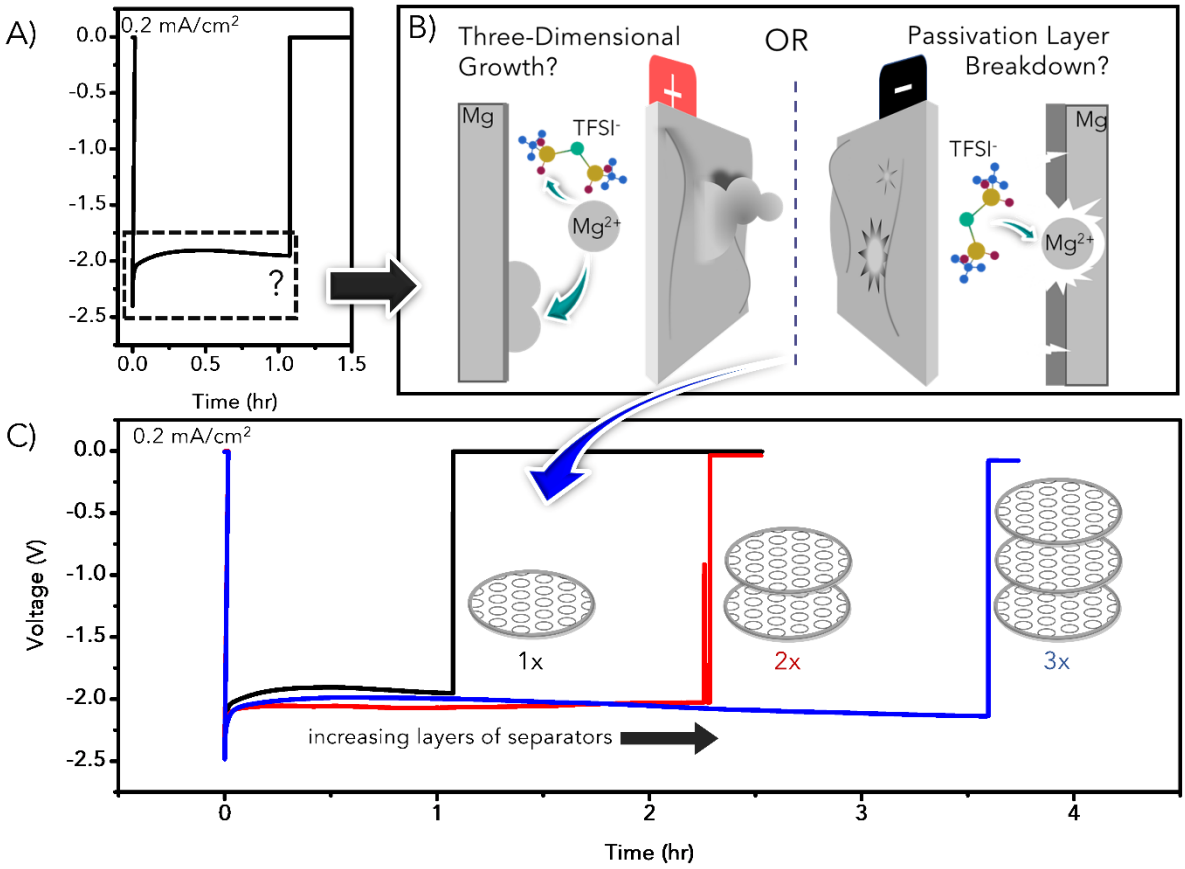

Figure 2: Electrodeposition Behavior in Mg Symmetric Cells. A) Typical galvanostatic plating curve for a Mg-Mg symmetrical cell at 0.2 mA/cm^2 in the presence of 0.1 M $Mg(TFSI)_2$ in 1:1 glyme:diglyme by volume. The boxed section encloses the overpotential plateau, which is thought to be a region of either passivation layer breakdown or nucleation and growth of 3-dimensional Mg deposits. B) Schematic describing aforementioned processes possibly occurring during plateau region. C) Resulting galvanostatic profiles after varying the number of Celgard 2325 separators used in same Mg-Mg symmetrical cell configuration.

To better understand and isolate the true meaning of this plateau, we performed galvanostatic plating experiments in Mg-Mg symmetric cells with increasing layers of separators. Here, a negative current was applied such that reduction of Mg^{2+} occurs at the working electrode, resulting in a negative plating voltage. Galvanostatic plating curves from Mg/Mg cells incorporating one, two, and three separators are shown in **Figure 2**c. We emphasize that the same electrode and electrolyte preparation practices were employed for all three cells. Overall, the three curves shown in Figure 1c have similar features except for the duration of the plateau. Adding a second separator increased the time to breakdown by 113%, and adding a third increased time to breakdown by an additional 122%. Since the anode and electrolyte were held constant, the changing separator thickness must exert control over breakdown time. The hypothesis that the plateau represents the breakdown of a passivation or adsorption layer therefore *cannot* explain the strong correlation.

To better understand this observation with increasing separator thickness, each coin cell in the separator study was subjected to electrochemical impedance spectroscopy (EIS) before and after electroplating through the high overpotential regime, as shown in **Figure 3**a. The results for the single separator case in **Figure 3**b show

a significant reduction in interface resistance (R_{int}) and the imaginary component of impedance. Additionally, a Warburg impedance component is expected at low frequencies for systems which undergo mass transfer, usually manifesting as a linear tail at low frequencies. Its absence implies a path for electron transfer which bypasses polarization of the electrolyte. In contrast to a perfect resistor, the system maintains some capacitive elements, signifying an intact passivation layer at either the counter electrode surface, deposit surface, or both, qualifying the phenomenon as a soft short circuit.[47,62,82,83]

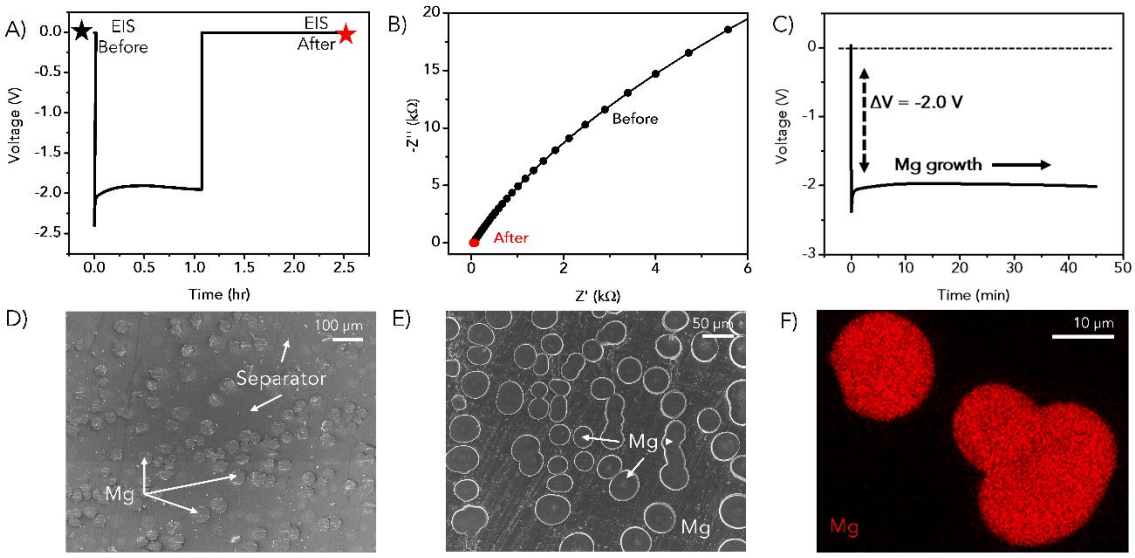

Figure 3: Identification of Short Circuit Signature in Mg Electrodeposition. A) Galvanostatic plating curve for a Mg-Mg symmetrical cell at 0.2 mA/cm^2. B) EIS of symmetrical cell before and after plating through high overpotential regime. See also figure S2. Spectra acquired with 10 mV amplitude in frequency range 0.5 Hz – 100 kHz. C) Constant current electrodeposition of Mg on Mg substrate at 0.2 mA/cm^2, stopped after 45 minutes for disassembly and SEM analysis. D) Electron micrograph of trilayer PP/PE/PP separator from cell subjected to constant current routine shown in (C) and peeled away from substrate, showing strong adhesion of Mg hemispheres to separator. E) Electron micrograph of bases of Mg deposits left behind on Mg substrate after electrochemical metal plating as in (C). F) EDS map of Mg, confirming that Mg is the primary element in observed deposits.

To further elucidate the processes occurring during Mg metal plating on polished Mg substrates, a cell was stopped in the midst of the plateau region, decrimped, washed, and analyzed to identify the presence or absence of Mg deposits (**Figure 3**c). As shown in **Figure 3**d, SEM imaging of the separator revealed numerous polycrystalline islands extending up into the porous scaffold with undersides sheared off the bases. The bases remained fixed to the substrate as sections of hemispheres, occasionally coalescing into dumbbells (**Figure 3**e) with flat topside appearance attributed to mechanical shearing during separator removal. In the specific case of electron dispersive spectroscopy (EDS), gold was used as the current collector in order to enhance contrast,

but polished Mg is used as a substrate in all other experiments. Whereas gold itself may undergo limited alloying with magnesium[84], the relatively high applied current density (0.2 mA/cm^2) and low temperature (298 K) prohibits diffusion into the bulk material. Supporting this hypothesis, the voltage trace possesses the same general shape as with magnesium substrates, lacking any plateaus early in the plating period that might indicate a phase transformation (**Figure 4**). As a caveat, it is important to note that subtle differences in surface roughness, crystal structure, and nucleation sites can produce differences in deposit morphology. EDS mapping of the hemispherical deposits on gold confirmed that magnesium was the primary constituent (**Figure 3**f), accompanied by trace fluorine and sulfur (**Figure 5**). The detection of magnesium demonstrates conclusively that nucleation takes place *prior to* the sudden reduction in polarization at the end of the plateau. Accordingly, we conclude that after a period of growth, 3D magnesium deposits protrude through the separator and produce a soft shorting event, to which we thereby attribute the rapid decrease in overpotential in the galvanostatic discharge profile. The presence of fluorine and sulfur points to the existence of an interfacial layer on the deposits, the precise composition of which has been noted to contain MgO, $Mg(OH)_2$, $MgCO_3$ and MgF_2 in other reports.[47,54,55] Detailed characterization of surface chemistry and the influence of operating conditions remains underexplored in the literature and requires further attention from the community.

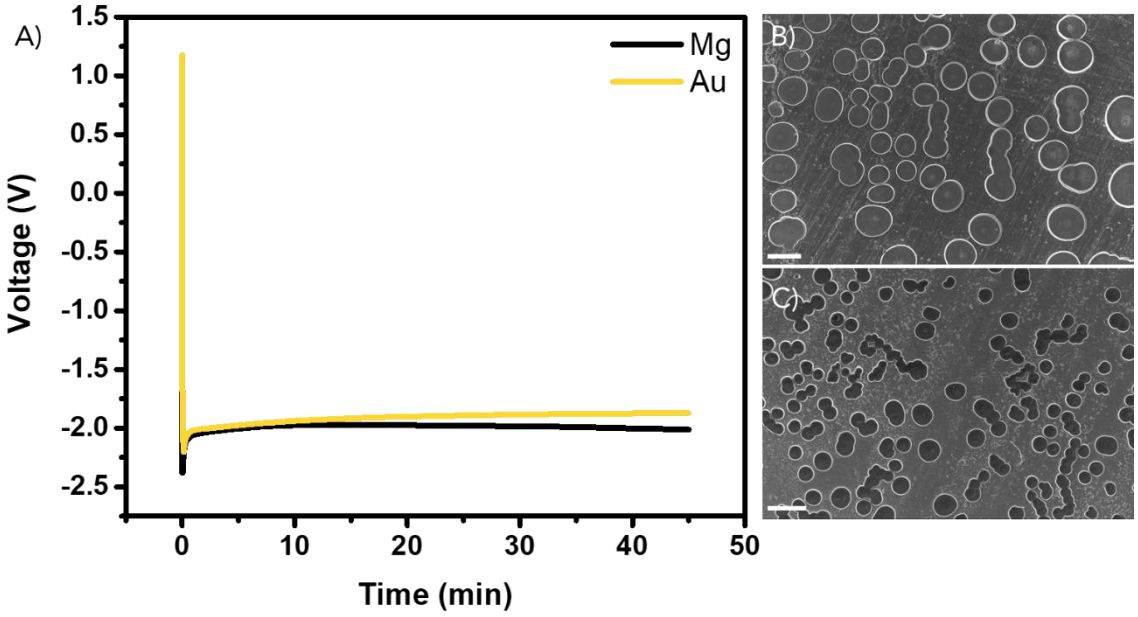

Figure 4: Comparison of deposition on Mg and Au substrates. A) Galvanostatic curves for deposition at 0.2 mA/cm^2 for 45 minutes; B) SEM image of resulting morphology on polished Mg substrate, scale bar = 50 μm; C) SEM image of resulting morphology on Au substrate, scale bar = 30 μm.

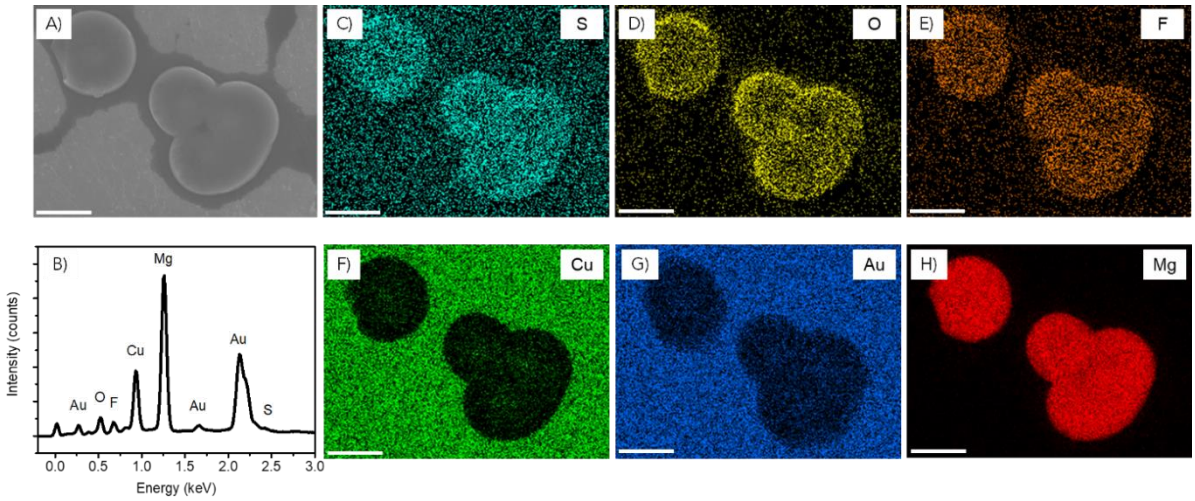

Figure 5: Energy Dispersive Spectroscopy (EDS) maps of magnesium deposits on gold substrates. A) Electron image; B) Map sum spectrum; C-H) Element specific maps.

2.4.2. Diffusion Limitations in $Mg(TFSI)_2$ Electrolytes

In the study of electrodeposition, hemispherical island-type growth often results from mixed kinetic and diffusion controls.[9,85–87] To gauge the extent of diffusion control, we measured the diffusion coefficient using an instantaneous potential step method.[68] From the slope of the resulting Anson plot in **Figure 6**, the diffusion constant, D_O, was determined to be 1.03 x 10^{-7} cm^2/s for the 0.1 M electrolyte solution, a full order of magnitude lower than typical lithium ion electrolytes.[59] It follows that with sluggish diffusion kinetics, rapid depletion can occur at the substrate-electrolyte interface during bulk electrolysis. For any current density exceeding the limiting current density, it is well understood that the interfacial cation concentration is rapidly depleted and species are reduced as quickly as they reach the surface, typically resulting in non-equilibrium morphologies which can be dendritic in nature.[49,59,68,69] The limiting current density, J_{lim} is defined as

$$J_{lim} = \frac{FD}{1 - t_+}\frac{2c^*}{L}$$

Equation 6

where F is Faraday's constant, t_+ is the cation transference number (extrapolated to be 0.272 for a dilute solution of $Mg(TFSI)_2$ in diglyme[80]), D is the diffusion coefficient, c^* is the bulk cation concentration, and L is the diffusion length. For D = 1.03 x 10^{-7} cm^2/s and an approximate cation transference number of 0.272[80] across a 25 μm separator, the limiting current density is about 1 mA/cm^2, which is within an order of magnitude of the currents typical for electrochemical analysis of Mg anode and cathode materials.

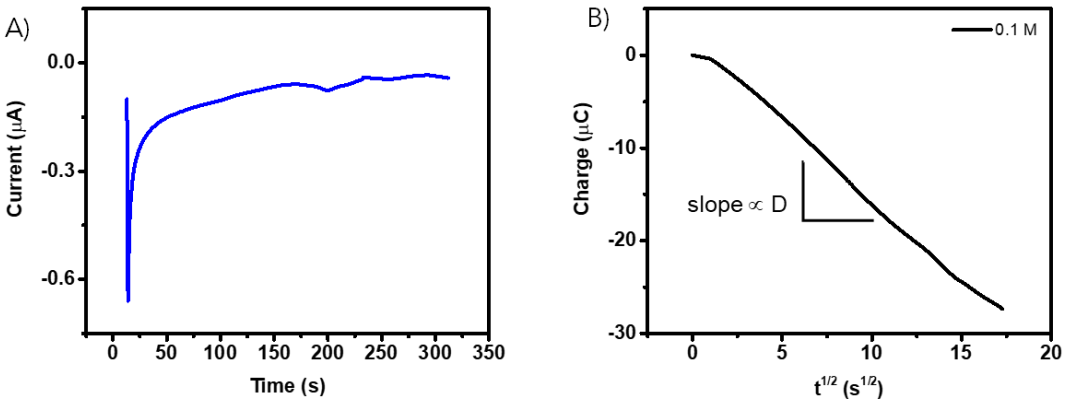

Figure 6: Extraction of diffusion coefficient from potential step experiment performed in 3-electrode flooded cell. A) Current response to sudden voltage step to -0.5 V vs Mg/Mg^{2+}; B) Corresponding Anson plot, the slope of which was used to calculate the diffusion coefficient in 0.1 M $Mg(TFSI)_2$.

To better evaluate the transition to diffusion limited growth at current densities within a few orders of magnitude of J_{lim}, we focus on a transition time, τ, at which the concentration of reactants at the surface, c_0, equals zero during extended electrolysis. This can be calculated using the Sand Equation, first derived by H.J.S. Sand in 1901[9,68] and represented by

$$\tau^{\frac{1}{2}} = \frac{nFAD_O^{\frac{1}{2}}\pi^{\frac{1}{2}}c^*}{2i(1-t_+)}.$$

Equation 7

For times greater than τ, non-equilibrium plating is probable and other species – like solvent molecules – may be consumed by the excess electrical current. Here, n is the number of electrons transferred (assumed to be 2 for Mg^{2+}), A is the electrode area, i is the applied current, and the other variables are defined as in Equation 1. Using Equation 2, we calculate Sand's time for experiments performed at 0.2 mA/cm^2 to be 1519 s, or about 25 minutes, which corresponds well to a local voltage maximum in the high (negative) overpotential regime from data in **Figure 7**a, denoted with a circle. This signifies the point where decreasing concentration of reacting species at the growth front dictates a more negative reduction potential, consistent with the Nernst equation.[9,68] To more broadly evaluate this concept, we analyzed this transition time at all current densities shown in **Figure 7**a ranging from 0.02 mA/cm^2 to 2.0 mA/cm^2 and found that the time corresponding to the minimum overpotential correlates closely with the $i^{-1/2}$ trend of transition time calculated according to Equation 7, achieving an R^2 value of 0.990 (**Figure 7**b). To further define what the transition time means for this system, we used the diffusion coefficient to simulate the theoretical concentration profile at the substrate surface over time for three different current densities (**Figure 7**c). For all the sampled current densities between 0.1 mA/cm^2 and 2 mA/cm^2, both above and below the limiting current density, there is an experimentally apparent transition to purely diffusion-controlled growth modes preceding an ultimate shorting event.

Experimentally, the relationship falls off at current densities much smaller than J_{lim}, when solid-state diffusion and reaction kinetics dominate over mass transport in the electrolyte.[9,59,69] Besides its outlying breakdown time, the galvanostatic transient for 0.02 mA/cm^2 in **Figure 7**a also has a unique feature at short time scales: the voltage decreases gradually over 10 minutes to a minimum point. In lithium electrodeposition, analogous behavior has been attributed to simultaneous nucleation and formation of solid electrolyte interphase, therein requiring extra charge to supply sufficient activation energy.[88] Although Mg(TFSI)$_2$-based electrolytes are not known to form SEI, it is speculated that the solvent reacts with surface defects to form a passivating film instead, which could further impede self-diffusion.[54,55,81,89]

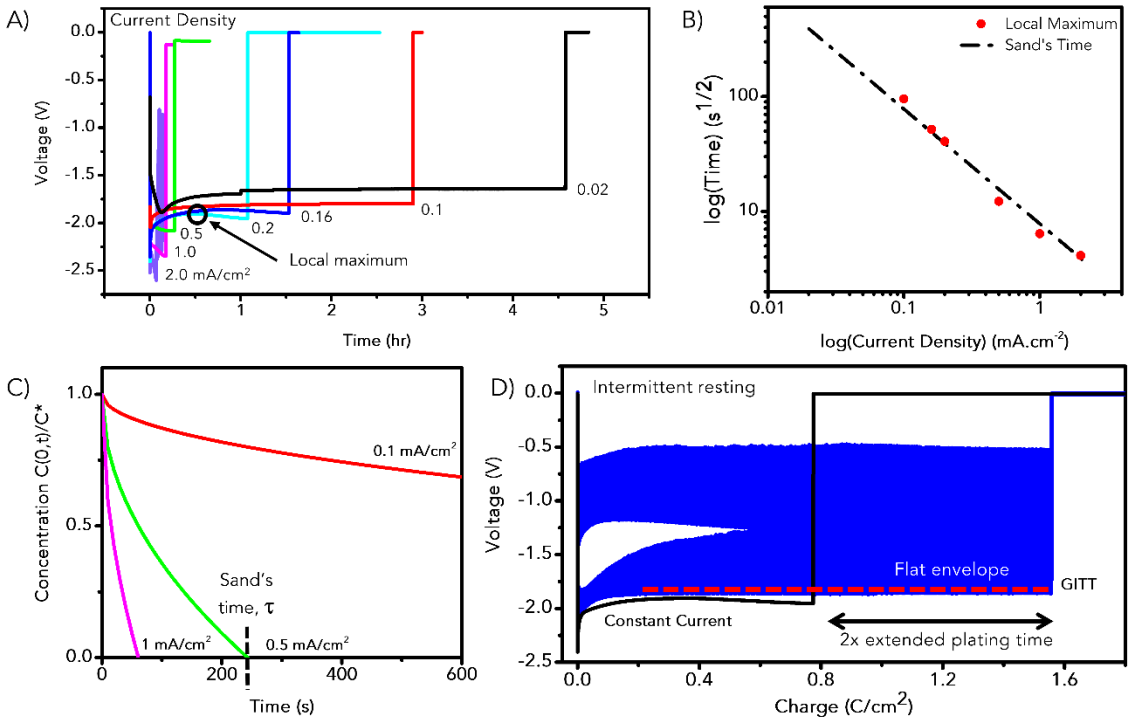

Figure 7: Diffusion Limitations in 0.1 M Mg(TFSI)$_2$ Electrolytes. A) Galvanostatic transients of Mg-Mg symmetrical cells plated at current densities from 0.02 mA/cm^2 to 2 mA/cm^2. B) Local maximum of overpotential plateaus extracted from curves in (A) plotted alongside Sand's time calculated according to Eqn 2. C) Computed concentration profiles at the substrate interface after constant current plating at 1 mA/cm^2, 0.5 mA/cm^2, and 0.1 mA/cm^2 for extended time periods. D) Galvanostatic intermittent titration technique applied to Mg-Mg symmetrical cell with current density 0.2 mA/cm^2 applied for 15 s with 180 s of rest between pulses.

Building from experiments so far, the influence of mass transfer limitations on the shape of the galvanostatic profile was further analyzed using galvanostatic intermittent titration technique (GITT). GITT is often used to study kinetic behavior because periodically resting the cell establishes near-static equilibrium conditions via minimization of concentration gradients through the electrolyte during short "on" periods.[63] If mass transport effects play a significant role in electrochemical behavior, the envelope formed by the minimum point in each

pulse should have a different shape than the steady state galvanostatic transient. GITT results are plotted in **Figure 7**d with respect to charge transferred, allowing for direct comparison to the original plating curve. Using a pulse time of 15 seconds (much less than the transition time of 25.3 minutes) at 0.2 mA/cm^2 followed by a 3-minute rest period, the GITT envelope forms an extremely flat plateau, lacking any statistically significant local maximum which was previously established as an indication of transition to pure diffusion control. Additionally, the overpotential was slightly reduced, and the total charge passed was improved by a factor of two.

It is evident from experiments discussed herein that Equation 2 provides insight into the mass-transfer limited growth of Mg metal nuclei at practical current densities commonly present in electroplating studies. In this way, one can utilize Equation 2 as a blueprint to control parameters in the cell which can postpone the reaction processes occurring beyond the transition window to mitigate 3D growth and eventual cell shorting, an idea supported by GITT measurements. Since it is generally impractical to introduce rest or re-equilibration times during battery operation, other modifications that can bear similar outcomes include increasing the transference number and modifying the electrolyte concentration, providing multiple ways to control and moderate shorting effects. Using longer chain glymes[47] and inclusion of additives[53,90,91] have also been effective in preventing shorting, although care must be taken not to shrink the electrochemical stability window. Further, the coulombic efficiency of Mg stripping and plating may be improved by avoiding diffusion-limited regimes where cation depletion could lead to surface passivation via reduction of solvent, anions, or contaminants.

2.4.3. Three-Dimensional Island Growth of Magnesium

Despite the fact that ramified dendritic growth is not expected when a system is driven below the critical current density, the observation of soft shorting phenomena under mild conditions emphasizes a need to unravel the true growth mechanisms dictating magnesium growth. Even at current densities that are two orders of magnitude below J_{lim}, we observe an eventual soft short during electroplating. One would naturally correlate a shorting effect to be correlated to dendrite formation since this has been observed with other alkali metals like Li and Na and dendrites have most recently been demonstrated to occur for Mg. In the context of metal electroplating, a dendrite is defined as a fractal structure in which the growth front proceeds at the rate of anion migration in order to preserve electroneutrality[59,65–67,70,92]. The velocity of dendrite growth is related to the applied bias, V, by the mobility, μ[68,70], which is independent of time. In contrast, revisiting the observations of **Figure 2**c leads to the conclusion that velocity of propagation through one, two, and three separators at 0.2 mA/cm^2 ($J < J_{lim}$) does not analytically match the rate of traditional dendrite propagation. In fact, as shown herein, this is more accurately modeled as the growth of a three-dimensional island under diffusion control (**Figure 8**a). Taking the growth velocity as the total separator thickness divided by the time spent under diffusion control, we find that the velocity decreases with time according to the classic solution for 3D hemispherical growth under diffusion control[9,86]:

$$\frac{dR}{dt} = \left(\frac{MDc^*}{2\rho}\right)^{0.5} \frac{1}{t^{0.5}}$$

Equation 8

where R is the radius for a hemisphere with 90° wetting angle, M is the molar mass of Mg, ρ is the density of Mg, and the other variables are as previously defined in Equations 1-2. This result is surprising because it implies that the electrodeposited metallic Mg was unperturbed by the presence of multiple trilayer PP/PE/PP separators and in fact used the separator as a scaffold for growth. This scaffolding effect is immediately clear from SEM imaging studies of Mg deposited at 0.2 mA/cm^2 through glass fiber separators (**Figure 9**), which preferentially break apart before shearing the deposit itself. In cross section, the islands are pictured engulfing the fibers, while a top view from the perspective of the counter electrode shows them penetrating all the way through. Some possible reasons for wetting of the separator by zerovalent magnesium could be high Mg surface tension[58], or the complex rearrangement of solvation structures throughout the process of multiple electron transfer.[89,93] This implies that the 3-D propagation of Mg metal growth could at least in part be moderated by separators with controlled surface properties.[94]

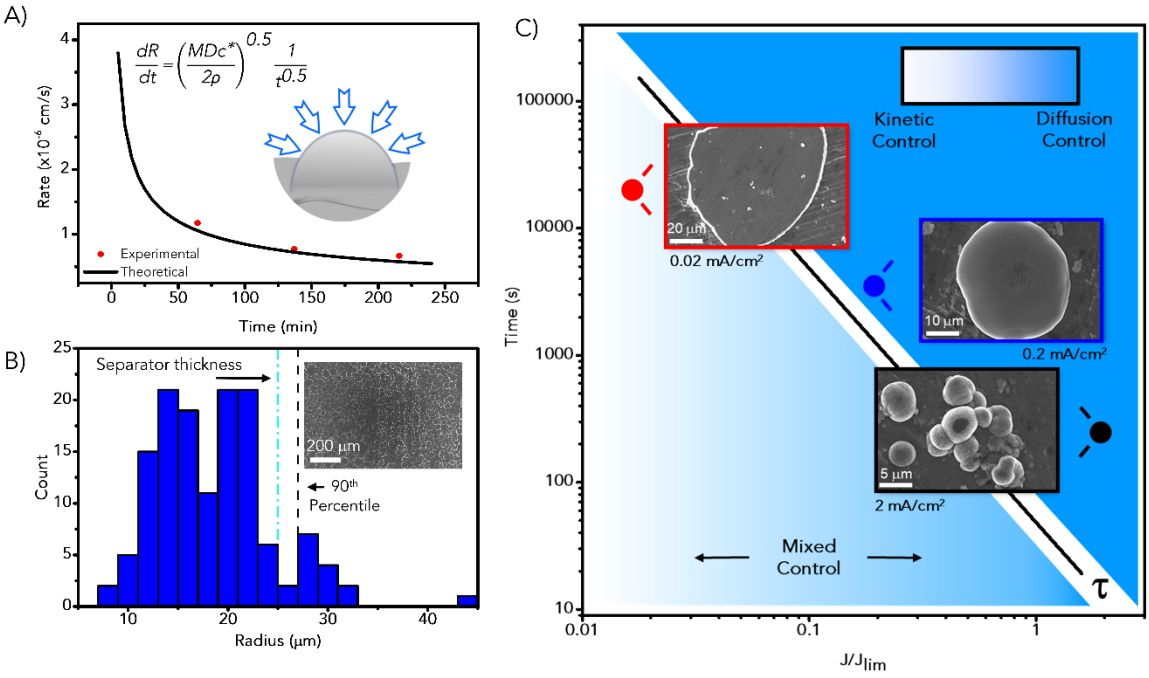

Figure 8: Three-dimensional growth of Mg is controlled by current density. A) Experimentally determined rate dR/dt of Mg hemispherical island growth from 0.1 M Mg(TFSI)$_2$ compared to rate predicted by diffusion controlled model of 3D growth[9,86]. B) Histogram of radii of individual Mg islands deposited on Mg substrate at 0.2 mA/cm^2, derived from electron micrograph shown in inset, scale bar = 200 µm. C) Dependence of transition time on fraction of the limiting current density and morphologies deposited at 0.02 mA/cm^2, 0.2 mA/cm^2, and 2 mA/cm^2 as a result of competition between kinetic and diffusion control.

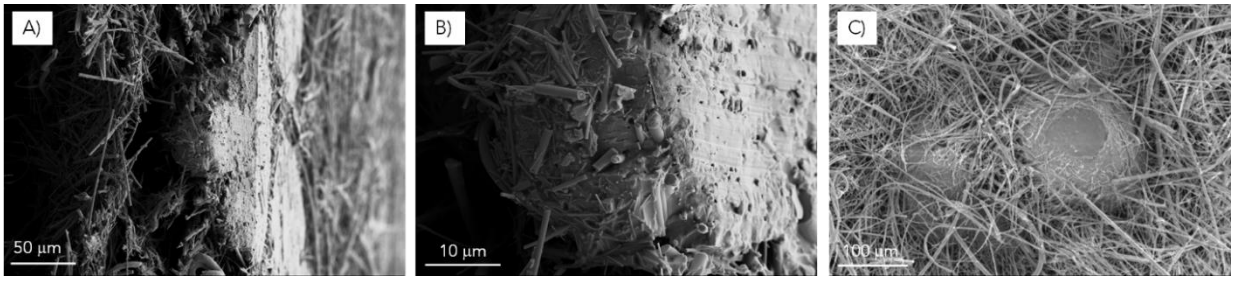

Figure 9: SEM images of hemispherical Mg growth through glass fiber separator at 0.2 mA/cm^2 in 0.1 M $Mg(TFSI)_2$. A) Cross section of separator, showing flat bases where deposits were lifted off of substrate; B) Higher magnification showing deposit engulfing glass fibers; C) View from "top" of a hemispherical Mg deposit, i.e. the side closest to the counter electrode.

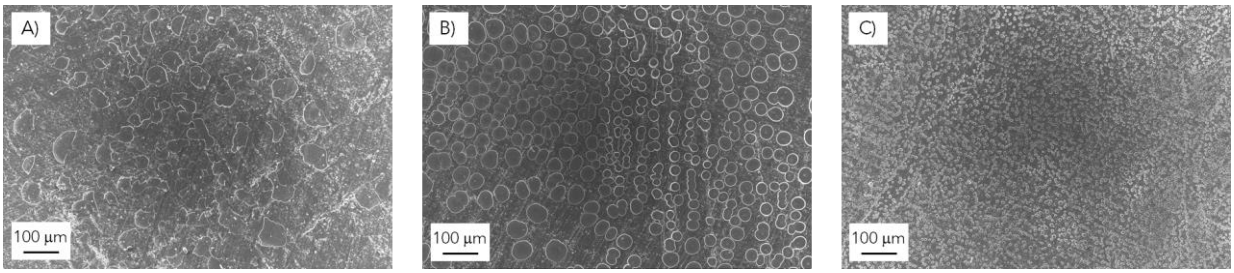

Figure 10: SEM images of Mg morphology when deposited at current densities of A) 0.02 mA/cm^2, B) 0.2 mA/cm^2, and C) 2.0 mA/cm^2

To further analyze the Mg morphology that forms under different current densities and understand these observations, we imaged deposits formed on magnesium substrates at 0.02 mA/cm^2, 0.2 mA/cm^2, and 2 mA/cm^2. **Figure 8**b shows a histogram of 137 individual islands grown at 0.2 mA/cm^2, demonstrating that 90% of deposits have a radius less than 25 microns, which is the thickness of one separator. Assuming a general hemispherical model where the height is equal to the radius, this would mean that the cell short circuited when some of these deposits grew to R = 25 µm, cutting off the driving force for any further reduction. We attribute this hemispherical growth mechanism of Mg deposits to diffusion control, and we delineate this from dendrite formation that would otherwise yield a similar shorted device outcome. At 0.02 mA/cm^2 – much lower than the critical current density – the bases of deposits left behind after separator removal deviate from circular geometry and grew significantly larger before shorting, indicating enhanced kinetic control. At 2 mA/cm^2 – above the limiting current density – we find a multitude of small nuclei that pile on top of each other like caterpillar segments, realizing a more traditional dendrite conformation since significant diffusion limitation drives preferential nucleation at protrusions. The average nucleus size and density follow trends consistent with those established for galvanostatic deposition of lithium metal, where higher current densities resulted in smaller, more numerous spherical nuclei which uniformly cover the substrate.[88] Direct comparison is presented

in **Figure 10**. Overall, SEM images showing representative deposits formed at these three current densities are included as insets in **Figure 8**c, demonstrating the competition between charge transfer and mass transfer at current densities within 2 orders of magnitude of the critical current density, J_{lim}. At very low current densities applied in the $Mg(TFSI)_2$-ether system, strong interactions between adjacent Mg adatoms[58] over large nuclei lead to three-dimensional growth which eventually traverses the separator to cause a soft short at times less than the transition time, τ, calculated according to Equation 7. At moderate current densities, mixed control gives way to mass transport limitation at times greater than τ, and deposits behave according to diffusion-controlled three-dimensional island growth. For high current densities $J > J_{lim}$, the concentration of cations is depleted at the surface almost instantaneously and protruding deposits of stacked spheres rapidly bridge the separator. In all cases, electrolysis concludes with a soft shorting event. By applying SEM analysis alongside GITT and traditional electrochemical models of nucleation and growth, we highlight a comprehensive picture of 3D growth that brings together past observations drawing from dendrite formation occurring due to solid state/surface diffusion mechanisms as well as our results that highlight 3D growth controlled by sluggish transport in commonly used electrolytes.

2.5. Conclusions

Overall, our results paint a picture that demonstrates key advances in understanding of Mg metal electroplating. First, our results indicate that the origin of the high overpotential commonly observed in Mg metal electroplating occurs subsequent to Mg metal nucleation, meaning that this cannot be attributed to common arguments of passivation layer removal. Second, our results highlight a competition between different mechanisms for electroplating over a full range of current densities practical to Mg battery operation – none of which form smooth layer-by-layer deposits that were previously assumed to be the case for electrodeposited Mg layers. Third, our results distinguish uniform 3-D growth of Mg scaffolded by the separator from that of traditional, ramified electrodeposits known as "dendrites" – both of which rely on different mechanisms but lead to the same symptomatic result in a battery of a soft-shorting effect. Although extended electrolysis tests have been extremely rare in Mg electrolyte studies to-date, we suspect that 3-D growth is not limited to TFSI-based electrolytes; anomalous voltage changes in early cycling accompanied by major reduction in impedance and/or SEM images of hemispherical growth have also been reported for TFSI with triphenolateborohydride additive[90], $Mg(CB_{11}H_{12})_2$ (MMC)[51,95], $Mg(HMDS)_2$[91], and $Mg[B(HFIP)_4]_2$ electrolytes[96].

Moving forward, understanding the different mechanisms behind Mg growth enables modification of the process. In the regime of 3D hemispherical growth at moderate current densities, one can leverage the insight of solution transport properties to control the mechanism of growth to some degree. Further, in the regime dictated by solid state/surface diffusion[48,58,97], one can seed the surface with abundant nuclei using a short high-overpotential pulse, or moderate surface properties of the current collector in a manner that has been recently explored for Na and Li metal batteries[98–100]. Finally, the weakness of traditional separators in impeding Mg growth may catalyze conversation about unique engineering solutions for multivalent systems, and possibly

open the door to solid electrolytes as a practical option for Mg[101], despite pervasive transport challenges in solid-state systems. Collectively, we assert that understanding and manipulating the strong electrostatic interactions characteristic of multivalent ions, and the mechanisms distinguishing observed behavior from that of monovalent alkali metals like Li and Na, are key steps toward realizing next-generation energy dense storage media.

Chapter 3: Leveraging Impurities in Recycled Lead Anodes for Sodium-Ion Batteries

3.1. Introduction

Like magnesium, sodium is a promising alternative ion for secondary batteries due to elemental abundance and the low cost of raw materials; however, the development of sodium ion batteries is limited by the availability of stable anode materials with sufficient energy density. In this chapter, I investigate the upcycling of lead acid battery electrodes into sodium ion battery anodes.

3.2. Background

In 2012, lead acid battery (LAB) production accounted for 85% of global lead demand [102]. About 80% of this demand is met with secondary lead recycled from spent batteries, exemplifying a largely closed-loop manufacturing cycle which keeps the toxic heavy metal out of waste streams [103]. Through the year 2022, demand for LABs is expected to continue growing alongside motor vehicles at an average annual rate of 3%; however, rechargeable lithium ion batteries (LIBs) account for increasing shares of the transportation and grid storage sectors, growing at a much faster annual rate of 9% [104,105]. Ultimately, with the price of LIBs expected to fall below $100/kWh by the year 2024 [106], a surge in electric vehicle popularity could destabilize the dominance of LABs, leading to a decline in the price of scrap lead [107], and a potential scenario where the broken loop of lead recycling has a detrimental environmental impact on wastewater streams and natural resources.

Lead-based electrodes may find new life in low-cost, rechargeable sodium ion batteries (SIBs). As the fourth most abundant element in the world, there exist over 47 billion tons of sodium precursor (soda ash) reserves worldwide, compared to 62 million tons of lithium. In turn, sodium is a target for the extreme scaling associated with penetration of grid-scale energy storage at residential levels [12]. Alloying anodes such as Sn [108–113], Bi [114–118], Sb [116,119–123], and Pb [114,124–128] have garnered much attention for application in sodium ion batteries due to high specific capacities and low operating voltages. Since Jow *et al* first established reversible alloying of sodium with lead (Pb) in 1987, the material was largely excluded from rechargeable battery design due to toxicity concerns. Recently, Darwiche *et al* studied the reversible alloying of Pb with sodium using diglyme as the electrolyte solvent, observing capacity retention of 464 mAh/g after 50 cycles in half cells [124]. These findings re-established lead as a promising anode material, despite being relatively under-explored.

In this work, we seek to establish a pathway for the recycling of Pb-based materials directly from used LABs. In this regard, recycled materials unlike raw pure materials contain impurities which can be troublesome for practical rechargeable battery design. Within the growing body of research in recycled battery cathodes[129–132] and alloying anodes[133–136], there is little understanding of the effect of residual impurities on electrochemical performance. In light of a recent analysis by Ciez and Whitacre showing that direct recycling of electrode powders has potential to reduce greenhouse gas emissions in battery manufacturing at competitive costs[137], studies of impurity impact are imperative to improve recycling initiatives. Our work demonstrates that recycled Pb alloys containing antimony (Sb) and tin (Sn) can be thermally processed to control the stability, rate performance, and storage capacity of sodium battery anodes. This highlights the ample potential in defect engineering of recycled and high-value materials for next-generation energy storage devices.

3.3. Experimental Methods

3.3.1. Pb Recycling

A previously used lead acid battery in fair condition was recovered from a totaled vehicle as shown in **Figure 11**. The battery was opened and dismantled to recover Pb materials. After draining the cell of sulfuric acid electrolyte, the components were neutralized by soaking in sodium bicarbonate solution. Then, the spongy lead from anode plates was scraped off before melting down the lead alloy in a smelting furnace above its melting point of ~330ºC. Remaining lead oxides and sulfates floated to the surface and were removed with the dross before cooling slowly in the furnace. Recycled Pb powder was produced by sanding the resulting ingot with a file or 220-grit SiC-based sand paper and sifting the shavings through a 325-mesh stainless steel sieve. The powder was neutralized a second time by soaking in sodium carbonate solution for ~12 hours before rinsing and drying under vacuum. At this point, powders undergoing heat treatment were annealed in a tube furnace at 430oC in reducing atmosphere for 30 minutes or 280oC for 2 hours and cooled slowly to room temperature. Heat treated powders were immediately processed into slurries and incorporated into coin cells within one week to avoid the recurrence of aging.

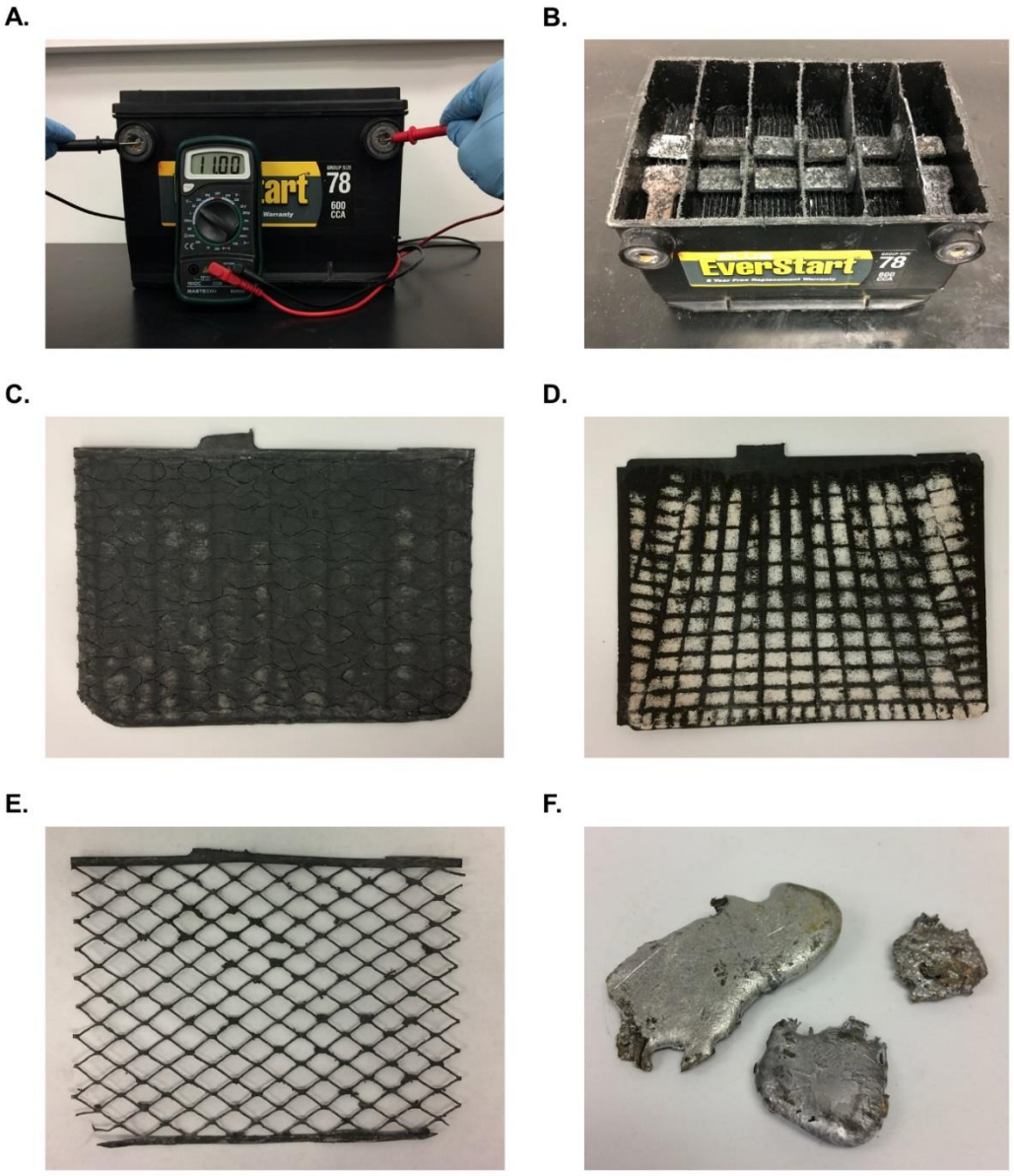

Figure 11: An overview of the recycling process: A) Used battery showing partial charge (11 V) at time of disassembly. B) Battery with electrolyte removed and neutralized and top cut off to expose the anode and cathode plates. C) Lead anode plate, commonly referred to as "spongy lead". D) Lead dioxide cathode plate. E) Lead mesh from an anode plate with the spongy lead removed. This material was used as the recovered lead to eliminate the need for extensive smelting and refining processes which are easily undergone in industrial settings yet are difficult at the lab scale. F) Final melts obtained from the lead mesh which was then filed, mechanically separated, characterized, and used in lead anodes.

3.3.2. Coin Cell Assembly

Anodes were prepared via slurry casting from an aqueous solution of either the prepared powder or 325 mesh elemental Pb (Sigma Aldrich >99%, trace metals basis) with 2 wt% carbon black (TIMCAL Super C45)

additive, 4 wt% sodium carboxymethyl cellulose (CMC) binder, and 1 wt% xanthan gum as a viscosity modifier. The anode slurry was applied to a carbon coated aluminum current collector and dried in a vacuum oven at 80oC for 24 hours before half cell construction. Active material loadings were between 4.5-5.5 mg/cm^2. Half cells consisted of the Pb electrode, two CelgardTM 2325 separators, and a sodium metal reference electrode (Sigma Aldrich 99.95%) housed in CR2032 coin cells. The electrolyte was 1M NaPF6 (99+%, Alfa Aesar) in diethylene glycol dimethyl ether ("diglyme", >99.5%, Sigma Aldrich). Before electrolyte synthesis, NaPF6 was dried at 100oC overnight on a hotplate in the glovebox and diglyme was dried over 4 Å molecular sieves for at least 48 hours. Electrolytes were used within 48 hours of preparation. Electrochemical Testing: Galvanostatic charge/discharge tests were performed on an 8 Channel MTI battery Analyzer between voltages of 0.00 to 1.00 V with the sodium metal electrode as the reference. All cells were cycled at a low rate of C/10 during the first cycle then brought to the testing rate. C-rates were determined based on the theoretical capacity of pure Pb: 485 mAh.g-1.

3.3.3. X-ray Diffraction

Diffraction spectra were taken on a Rigaku SmartLab X-Ray Diffractometer. Background diffraction was subtracted from the sample signal and crystallographic information was obtained through the Rigaku Data Analysis software.

3.3.4. Imaging

Coin cells were de-crimped, the electrode of interest rinsed twice in dry dimethyl ether (DME), and stored in a sealed vial for transport to SEM. Samples were exposed to air during transfer. Imaging was conducted using a Zeiss Merlin SEM with EDS detector.

3.4. Results and Discussion

3.4.1. Recycled Alloy Characterization

Pb-based powder was directly recycled from a used LAB. As depicted in **Figure 12**a, the used anode grid plates were neutralized, cleaned of PbO_2/$PbSO_4$ sludge, and smelted above 330^{o}C for 10 minutes to form a Pb-based alloy ingot. After removing the dross, the melt was furnace-cooled and aged at room temperature for approximately 12 months. Ageing of lead-antimony (Pb-Sb) alloys is known to result in the precipitation of fine, Sb-rich β-phase particles within the Pb-rich α-phase matrix and has been previously studied for its hardening effects. The aged alloy enables evaluation of a very fine microstructure, which can be subsequently heat-treated to restore the equilibrium morphology as predicted by the Pb-Sb-Sn phase diagram [138]. To establish the alloy composition obtained from the recycled Pb electrodes, quantitative energy dispersive x-ray spectroscopy (EDS) analysis was performed on a portion of the aged, recycled Pb ingot prepared by water-

cooled sanding followed by polishing with 1 μm and 35 nm alumina slurry. The map spectra of three random areas were averaged to find that the alloy contains 73.1 ± 0.7 % Pb, 21.3 ± 0.6 % Sb, and 5.55 ± 0.05 % Sn, corresponding to a hypereutectic composition (**Figure 12**b). An antimony concentration of 21 at% is slightly higher than reported values for grid alloys, which typically range from 0.5-12% depending on the brand, application, and year of manufacture [139,140], but may reflect the history of the used battery from whence it came. As antimony is a more noble metal than lead, it resists corrosion at positive electrodes, while lead is first to dissolve from the current collector grids[141]. The influence of grid health on microstructural and electrochemical properties of the recycled alloy could be an interesting area for further study.

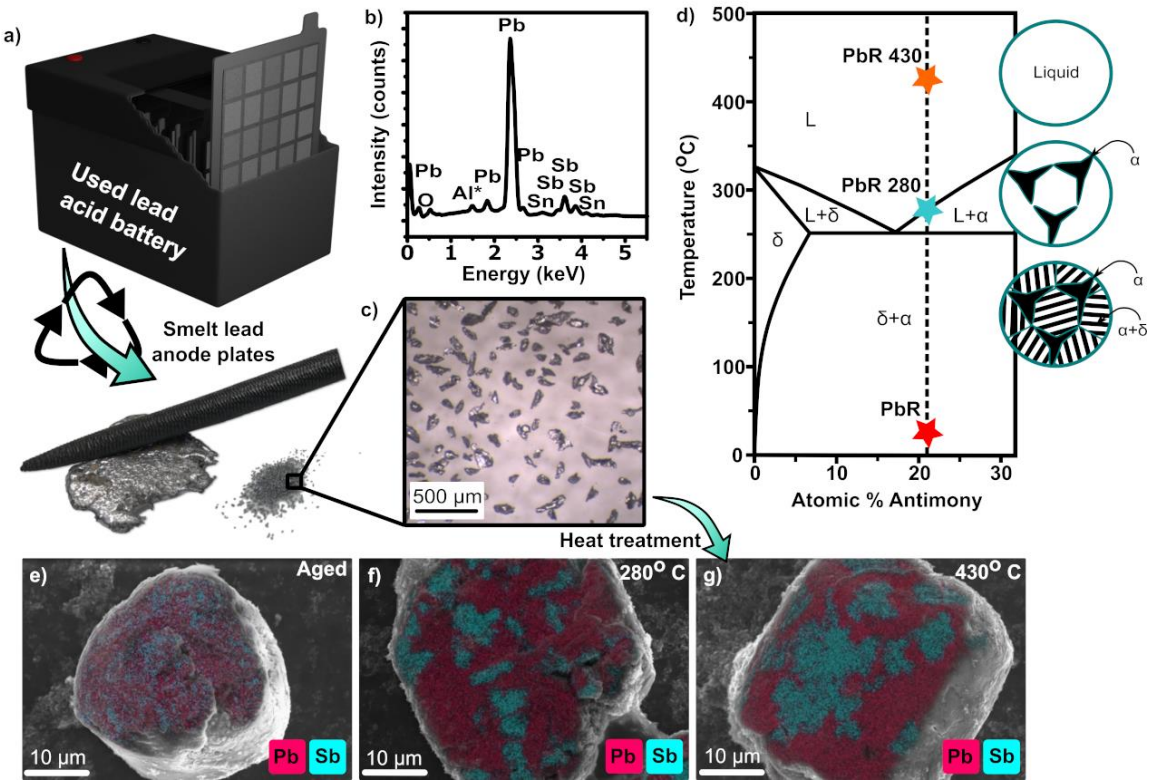

Figure 12: Process for direct recycling of Pb alloy powder from a used lead acid battery. A) Anode plates are cleaned, smelted, and aged as an ingot; B) EDS spectrum for a flat, polished section of the ingot acquired at 20kV; C) Optical microscope image of Pb alloy filings; D) schematic phase diagram based on [142] showing the regimes of heat treatment of the Pb alloy at the measured composition; E-G) EDS maps of the aged and heat treated particles acquired at 20 kV, overlaid over SEM images.

Pb alloy powder with particle size <325 mesh was produced from the ingot by shaving and sieving, resulting in oblong particles with sharp edges (**Figure 12**c). The powders were then heat treated in a tube furnace under reducing atmosphere at 430°C for 30 minutes or 280°C for 2 hours and cooled slowly to room temperature. Due to the relatively low concentration of tin, we approximate alloy rehomogenization in the context of the

binary Pb-Sb phase diagram. [142] The ternary Pb-Sb-Sn phase diagram outlines the existence of Pb, Sb, Sn, and Sb-Sn, but there is very little solid solubility for Sn in Pb and no ternary compounds are known [138]. A schematic phase diagram based on Okamoto[142] is included in **Figure 12**d, where the stars along the dotted line indicate the chosen heat treatment temperatures at the measured composition. Upon rehomogenization at temperatures exceeding the liquidus line, the phase diagram would suggest that a Sb-rich β-phase dendritic matrix is first to precipitate from the melt at hypereutectic concentrations, followed by formation of a lamellar eutectic structure between dendritic branches, with characteristic length scale dictated by the cooling rate. As predicted, EDS performed on the aged particles revealed coarse, dendritic β-phase precipitates surrounded by a fine distribution of more Sb and Pb, indicating that significant ageing had occurred (**Figure 12**e). Upon ageing, the eutectic morphology restructures over time, favoring spheroidal precipitates of β near dendritic boundaries [139]. After heating at 280ºC for 2 hours and cooling slowly to room temperature ("PbR 280"), EDS maps reveal the return of classical dendritic morphology in the form of small, branched Sb domains, with a reduction of Sb concentration in the matrix (**Figure 12**f). Increasing the temperature to 430ºC for 30 minutes ("PbR 430") facilitated segregation of Sb into even larger β-phase dendrites (**Figure 12**g). Heat treated powders were immediately processed into slurries and incorporated into coin cells within one week to avoid the recurrence of aging.

The crystal structure of the aged, recycled Pb alloy ("PbR") was compared to >99% elemental Pb from Sigma Aldrich ("PbS") using x-ray diffraction (XRD). Spectra were acquired before and after one full discharge at C/10 in a coin cell versus a sodium metal counter electrode (**Figure 13**a). The numbered positions on the discharge curves in **Figure 13**a correspond to the numbered XRD patterns in **Figure 13**b. The results for micrometric lead purchased from Sigma Aldrich confirm that the composition is mostly metallic Pb with some contamination by α-PbO, which is common in Pb manufacturing processes [102]. After sodiation, weak peaks corresponding to $Na_{15}Pb_4$ emerge at $2\theta = 37.8^{o}$ and 63^{o}, indicated by blue stars. The pattern for recycled Pb proves successful processing of metallic Pb with elimination of most α-PbO and other oxides or sulfates. Additional peaks match most closely with $Pb_{0.1}Sb_{0.9}$, consistent with expectations for a Sb-rich α-phase cooled at a finite rate. As with the commercial sample, alloying with sodium results in a peak at 37.8^{o}, corresponding to $Na_{15}Pb_4$.

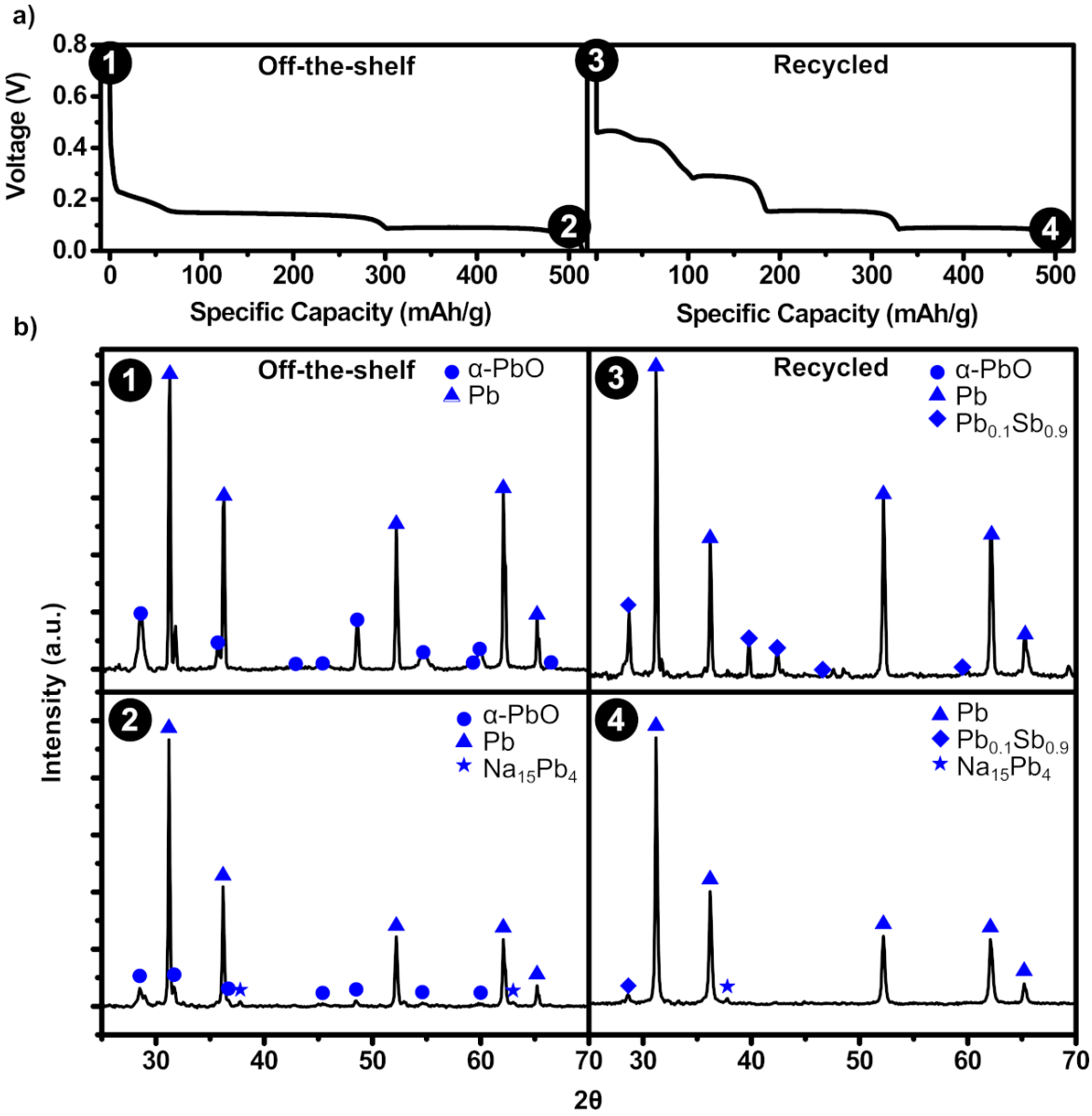

Figure 13: XRD analysis of commercial, 325 mesh elemental Pb (Sigma Aldrich >99%, trace metals basis) compared with recycled alloy powders in pristine and fully sodiated states. A) Galvanostatic discharge of Pb and Pb alloy at a rate of C/10 in coin cells versus sodium metal, with numbered circles to indicate charge state at time of B) ex-situ XRD measurements.

3.4.2. Electrochemical Comparisons of Recycled vs Refined Pb

Recycled and purchased lead anodes were electrochemically characterized in half cells versus sodium metal (**Figure 14**a-b). In galvanostatic testing, the first cycle was measured at a current density of C/10, while subsequent cycles were driven at C/2 (242.5 mA/g_{active}). For the purchased, refined lead, the first discharge capacity was 522 $mAh.g^{-1}$ and the first charge capacity was 477 $mAh.g^{-1}$. While the first discharge includes contributions from irreversible SEI formation and intercalation in PbO, the charge capacity matches closely

with the theoretical capacity of 485 mAh.g^{-1} for $Na_{15}Pb_4$ [114]. In contrast, the aged, recycled alloy had a high first charge capacity of 497 mAh.g^{-1}, suggesting that Sb and/or Sn are also active within the voltage window. Analyzing the differential charge with respect to voltage for the second cycle (**Figure 14**c-d) provides further evidence for the electrochemical activity of Sb. The major peaks, which represent nucleation of a new crystalline phase, are in good agreement with known voltages for $NaPb_3$, NaPb, Na_9Pb_4, and $Na_{15}Pb_4$, [114,124,125]; however, the recycled Pb also produces a broad discharge peak around 0.55 V, accompanied by two sharper charge peaks at 0.74 and 0.84 V. Such behavior is characteristic of Sb sodiation, in which an amorphous intermediate phase is formed during discharge while desodiation proceeds through the definite evolution of Na_3Sb to NaSb to Sb [123,143]. Analysis of the galvanostatic transients reveal that approximately 81 mAh/g_{alloy} is stored in these two charge plateaus during the first cycle. With a concentration of 21 at%, or ~14 wt%, antimony in the alloy and a theoretical capacity of 660 mAh/g_{Sb}, this result agrees well with the theoretical maximum contribution from Sb of 90 mAh/g_{alloy}.

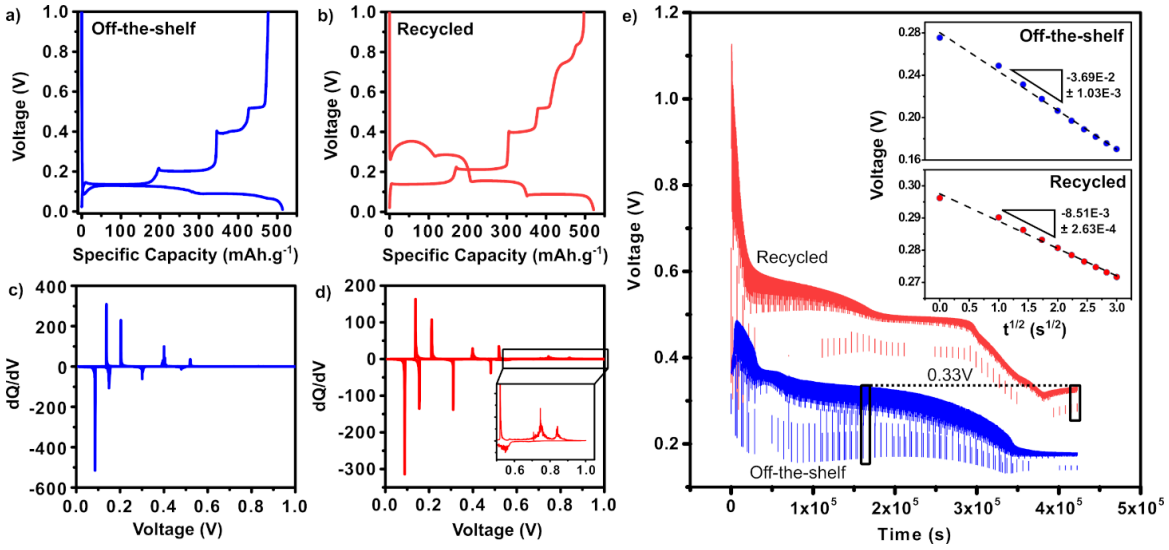

Figure 14: Comparison of first cycle behavior of commercial and recycled Pb-based anodes in half cells versus sodium metal. A) First galvanostatic cycle of off-the-shelf elemental Pb powder and B) recycled Pb powder at a rate of C/10; C-D) differential charge plots corresponding to (A) and (B), respectively; E) results of galvanostatic intermittent titration to enable comparison of solid state diffusion coefficient, which is proportional to the slope of voltage with respect to the square root of time (inset).

Early cycling behavior was further probed using galvanostatic intermittent titration technique (GITT) to minimize the role of mass transport through the interphase. By applying the appropriate parameters for current density and rest time, the concentration gradient of Na^+ across the cell is expected to approach quasi-steady-state, such that the system becomes reaction-rate limited. More information regarding GITT is provided in the Supplementary Material. A C/10 current (48.5 mA.g^{-1}) was applied for 10 seconds, followed by a rest period of 300 seconds, yielding the envelope patterns in **Figure 14**e. To first discuss the commercial Pb, a short

plateau emerges early in sodiation, beginning at approximately 0.48 V, which corresponds to the formation of $NaPb_3$. In this regime, the width of the envelope is related to polarization, which continuously narrows through the formation of NaPb at 0.37 V, and is suddenly reduced with the formation of Na_9Pb_4 at 0.19 V. These findings are consistent with polarization calculations performed by Darwiche et al, who hypothesized that electrochemical gridding during the first cycle facilitated future sodiation [124]. In the case of aged, recycled Pb alloy, sodiation begins with a solid solution regime at potentials between 1 V and 0.6 V vs Na/Na^+. This cannot be attributed to the carbon additive, since both the recycled and commercial samples contained 2 wt% carbon black and this feature does not appear in both sets of data, but may represent limited activity in the minority alloying element, Sn. In accordance with the binary Na-Sb phase diagram, it is unlikely that the solid solubility of Na in Sb would be greater than 1 at%.[144] The first plateau beginning at 0.60 V corresponds to the sodiation of Sb through an amorphous intermediate phase, as previously described. This does not seem to be a result of mass transport limitation, since pulses along this plateau still obey the linear relationship between potential and the square root of time defined by the Sand Equation for times much less than the characteristic diffusion time, and has been explained as a stress-balancing mechanism [123]. The following $NaPb_3$ plateau is substantially longer than that observed for the commercial counterpart, and the narrow envelope of the NaPb plateau beginning at 0.32 V implies less polarization than the formation of this phase in pure Pb.

For times much less than the characteristic diffusion time ($t << r^2/D$) and small concentration changes, there should be a linear relationship between potential, *E*, and the square root of time, *t*, which obeys Equation 1 [145]:

$$E_t = -\frac{RT}{F}\frac{|i|}{0.5Fc_n\sqrt{\pi D}}\sqrt{t} + E_n$$

Equation 9

where *n* designates the state before application of a current pulse, c_n is the concentration of sodium in the alloy, and E_n is the potential before the pulse [145]. This formula was applied to the two alloys at the same voltage, 0.33 V, which coincides with growth of NaPb. As shown in the inset of **Figure 14**e, the plots obey a linear relationship, with an R-squared value of 0.994 for commercial Pb and 0.992 for recycled. Although the exact diffusion constant cannot be determined explicitly, we assume similar electrode surface area and current density to calculate an effective diffusion coefficient 3.62 times greater in recycled Pb. Details regarding this calculation are available in the Supplementary Material. From this result, we hypothesize that the increased interfacial surface area between alloy phases in the recycled Pb intrinsically enhances solid state diffusion.

3.4.3. Thermal Processing of Alloys to Control Electrochemical Properties

To support this argument of improved solid state diffusion, we evaluated the relationship between electrochemical performance and interfacial surface area between phases in the thermally processed powders. Heat treatment of the Pb-Sb-Sn alloys enabled significant tuning of power (**Figure 15**) and cycle life (**Figure 16**) properties through manipulation of phase boundaries and microstructural stability. **Figure 17**a compares

the power performance of PbS with the recycled alloys at rates ranging from C/10 to 2C. The ranking of samples in order of discharge capacity retention is as follows: PbR 430 < PbS < PbR 280 < PbR. In cycle life tests over 50 cycles (**Figure 17**b), the order of capacity retention is nearly reversed: PbR 280 < PbR < PbS < PbR 430. Although PbS tracks closely with PbR 280 in early cycles, it ultimately undergoes a recovery, reaching a local maximum in specific capacity around cycle 45.

In order to elucidate the performance trends summarized in **Figure 17**a, we performed post-mortem analysis on the electrodes after undergoing power tests. We found that all of the electrodes had gradually self-assembled into highly porous networks supported by ligaments which increase in average thickness as PbR280 < PbR < PbR 430 < PbS. Glymes are also known to cause gradual evolution of microstructure [126]. Wang *et al* concluded that ether solvent wets the electrode surface well enough to penetrate pinholes left behind during desodiation, which eventually grow and force rearrangement of the surrounding material [115]. In the case of PbR, nanoscale domains, high interfacial surface area, and expansion mismatch of the elemental components[143,146–148] may lead to the development of many pinholes for diglyme ingress, creating a multitude of small pores. The thin ligaments greatly enhance solid state diffusion and power performance, but ultimately form a fragile structure with reduced capacity retention. An additional mechanism for loss is suggested by the gradual disappearance of defined plateaus between 0.6 - 1.0 V in **Figure 16**, in combination with the fragmentation of Sb precipitates observed in **Figure 18**; as Sb and Sn domains are stressed, broken, and dispersed, the small size creates a larger barrier to nucleation of a second phase [143]. The intermediate sample, PbR 280, evolved average strut thickness on par with the aged sample, PbR, but exhibited rapid capacity loss. It was treated in a regime of the Sb-Pb binary phase diagram very near the liquidus line, which was expected to ripen existing precipitates without melting, forming blocky structures. The early failure could be related to domain size and shape effects which maximize interfacial stress. In contrast, the fully rehomogenized PbR 430 demonstrated the best cycle life, but performed poorly at high discharge rates. The lower interfacial surface area and extensive phase segregation resulted in behavior very similar to pure Pb, although contributions from Sb and Sn secure a higher final specific capacity. Altogether, we demonstrate that battery performance is sensitive to elemental distribution in ternary alloys, and conventional metallurgical heat treatment can be applied to balance power and cycle life. This work provides the basis for us to facilitate self-assembly of porous nanostructures with differing electrochemical characteristics influenced by the original alloy microstructure, capable of both extending cycle life through accommodation of swelling and enhancing rate capability by reducing diffusion lengths.

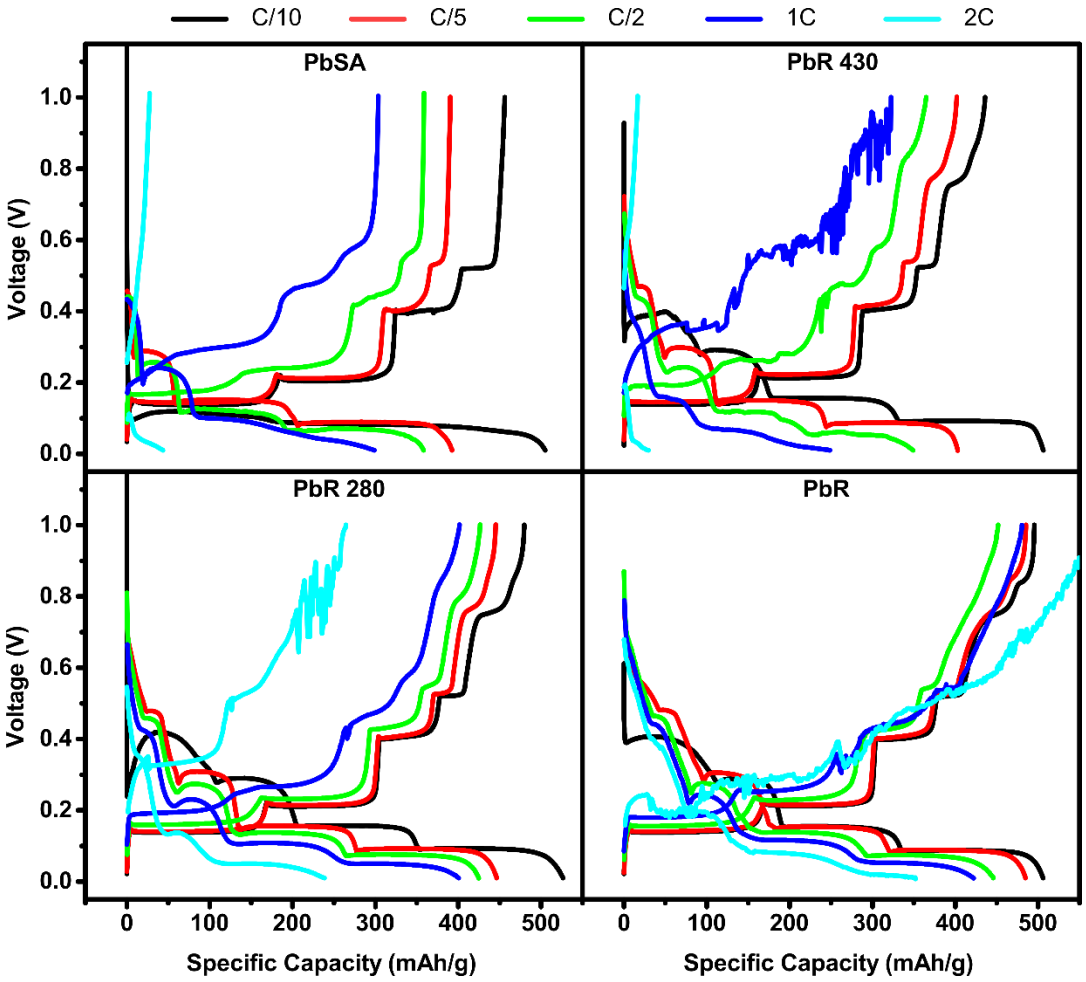

Figure 15: Galvanostatic cycling curves comparing rate performance of >99% elemental Pb (Sigma Aldrich) to recycled Pb-based alloys in half cells versus sodium metal with 1M $NaPF_6$ in diglyme. Anomalous charge curves in the recycled Pb alloy materials may be related to internal loss of electrical contact during rapid volume contraction at high C rates.

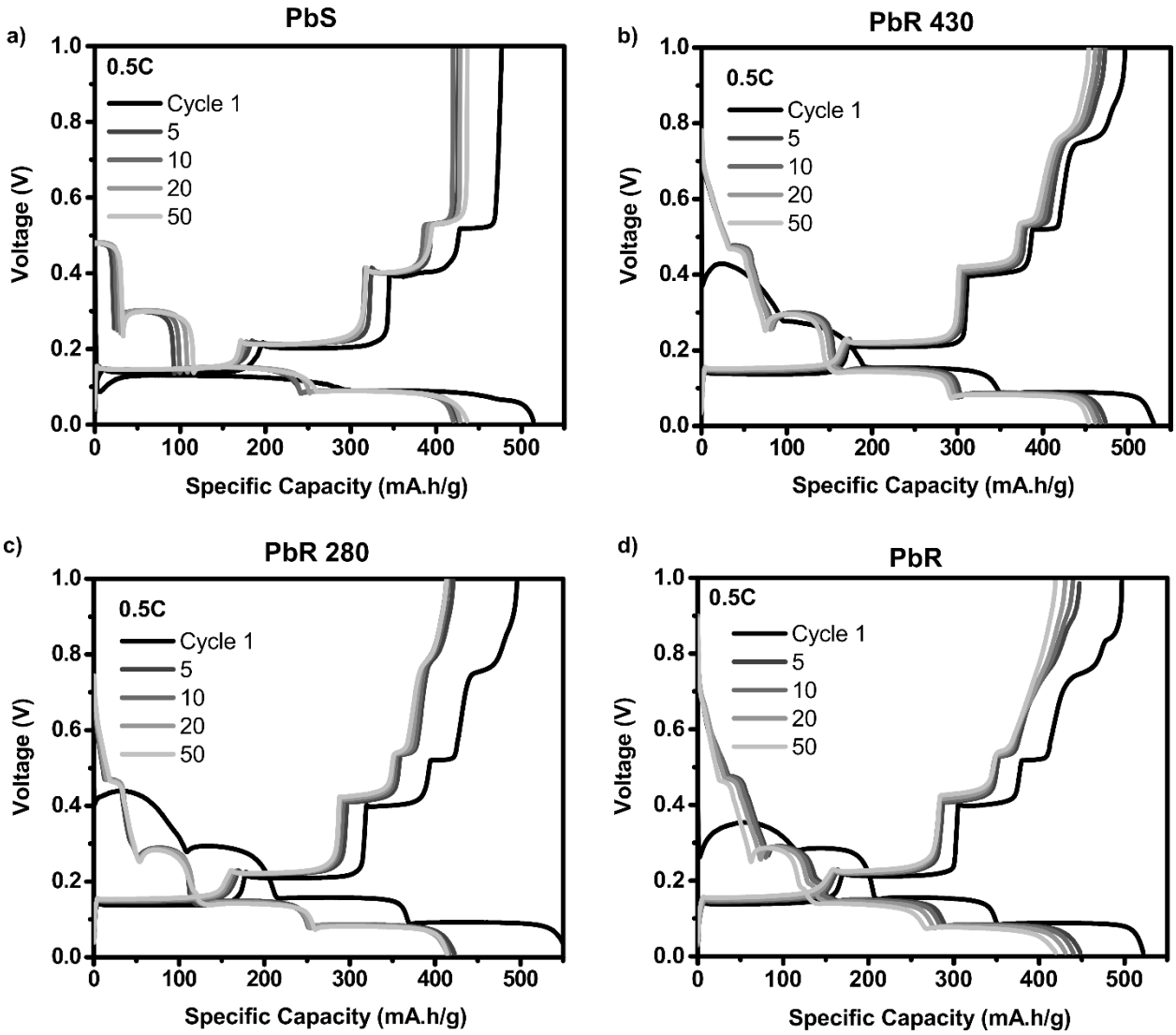

Figure 16: Galvanostatic cycling curves comparing cycle life of a) >99% elemental Pb (Sigma Aldrich) to (b-d) recycled Pb-based alloys in half cells versus sodium metal with 1M $NaPF_6$ in diglyme. A current density of C/10 was used for the first cycle, followed by C/2 for subsequent cycles.

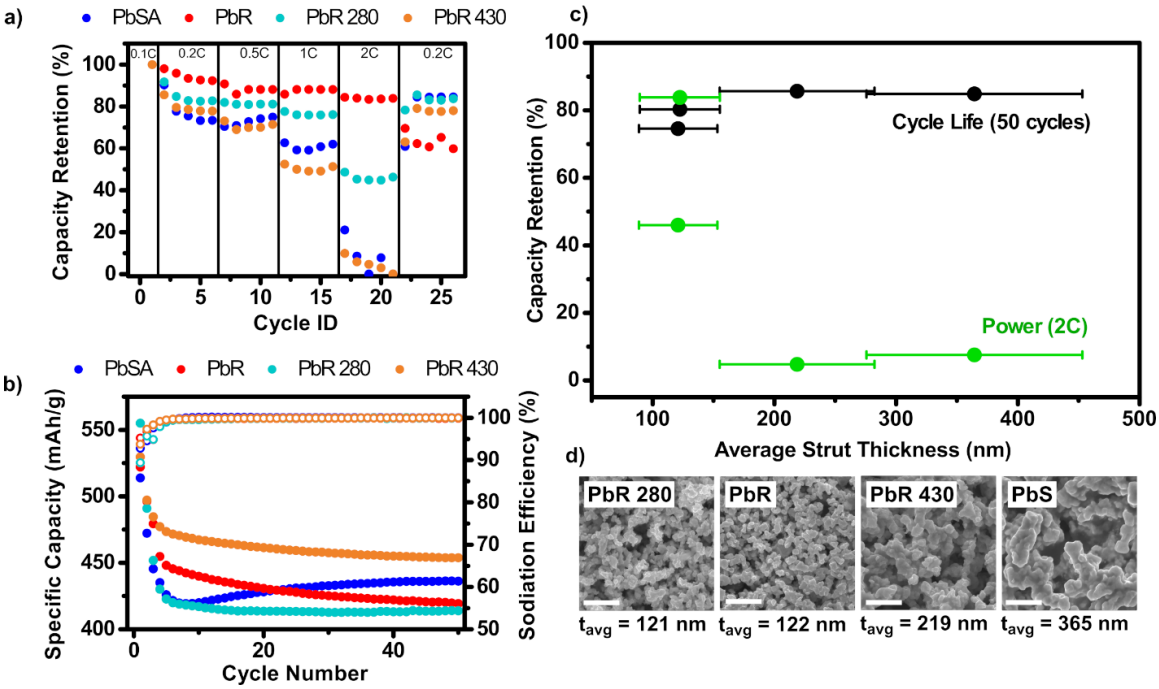

Figure 17: Summary of a) rate capability and b) cycle life at a rate of C/2 for pure lead compared to recycled, heat treated powders; c) relationship with average strut thickness measured from d) SEM images acquired during post-mortem analysis. Scale bar = 10 µm.

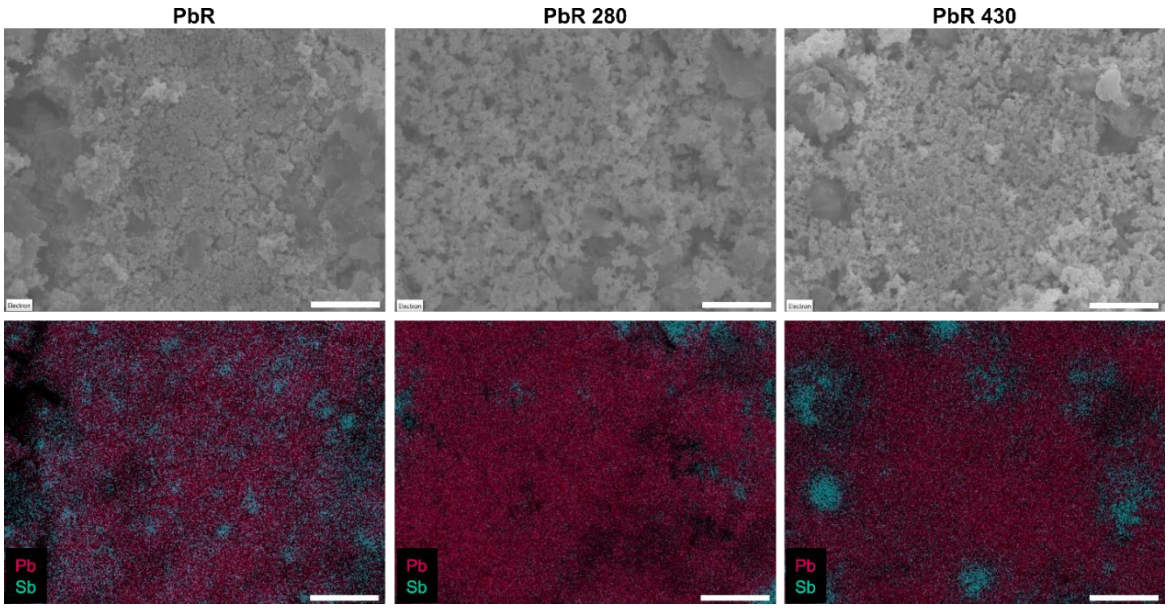

Figure 18: Results from SEM (top row) and EDS (bottom row) analysis performed on Pb-based alloy electrodes after 50 cycles at C/2 in half cells versus sodium metal. All scale bars are 10 µm.

3.5. Conclusions

In this work we demonstrate that the recovery of Pb-based materials from LABs results in impurity phases that facilitate a rich interplay of alloy properties that can be tuned to manipulate final electrode and cell characteristics. The ternary Pb-Sb-Sn system is unique because the large differences in assumed crystal structure and atomic radius of the elemental materials lead to very limited solid solubility, except for the existence of a SbSn intermetallic compound. Thus, the constituents retain their independent electrochemical properties, but are modified by the size and shape of domains, differential stresses, and interfacial surface area. In the presence of glyme-based electrolytes, the result is a tunable self-assembled nanostructured alloy phase with a high specific capacity of 522 $mAh.g^{-1}$. Although the final nanostructure enhances rate kinetics, GITT was used to show the enhancement of solid state diffusion in the early stages of cycling via transport along interfaces. We show that, despite very high impurity levels in the recycled alloy, extra temporal and energy inputs for refinement were not only unnecessary, but would be detrimental to cell performance. Heat treatment was utilized to modify alloy structure, and our findings indicate the time/temperature design space is extensive to produce optimal electrode architectures. We envision this work to be applicable not only to Pb anodes, but other alloying electrodes used in rechargeable batteries, such as tin or silicon. The approaches described in this work to leverage impurity phases to mitigate volume expansion provides a unique design space for the design of next-generation low-cost, and high performance electrodes. However, in the specific case of lead alloys, the ability to produce low-cost stationary storage applications from recycled lead materials provides a sustainable pathway to mitigate the leaching of toxic lead into wastewater streams and the environment as the transition from combustion powered to electric powered vehicles evolves.

Chapter 4: Dynamic Color Tuning with Electrochemically Actuated TiO_2 Metasurfaces

4.1. Introduction

In this chapter, I begin to explore ways in which electrochemistry can be applied to reduce the power consumption of dynamic photonic devices, especially more reflective display applications. In the visible spectrum, full spectral color tuning is inhibited by the large absorption that accompanies index changes, particularly at blue wavelengths. Here, we show that the electrochemical lithiation of anatase TiO_2 to $Li_{0.5}TiO_2$ (LTO) results in an index change of 0.65 at 649 nm with absorption coefficient less than 0.1 at blue wavelengths, making this material well-suited for dynamic visible color tuning. The dynamic range, speed, and cyclability of the TiO_2/LTO system indicate that it is competitive with established actuators like WO_3, with the additional advantage of reduced absorption at high frequencies.

4.2. Background

Color can be categorized as pigmentary or structural, and while pigmentary colors eliminate certain wavelengths of light due to absorption at energies dictated by electronic transitions, structural color is

generated from physical geometry. Since structural color does not directly rely on absorption, materials with ultra-low loss can be harnessed to build vibrant colors through interference, diffraction, or scattering. Active control over structural color is a burgeoning field of interest with applications in areas such as anticounterfeiting, consumer electronics, thermoregulation, and camouflage.[22,149] Furthermore, decoupling the electromagnetic response from intrinsic material properties allows for access to numerous modalities for dynamic color tuning. Approaches to modulation can be separated into two categories: 1) mechanical reconfiguration of the geometry and arrangement of scatterers; 2) manipulation of the optical properties of the scatterer or its environment for a resulting change in resonance frequency.[22] Although there are a variety of paths to achieve modulation, electrochemistry is the only method that belongs to both categories as it can provide large changes in geometry[36] as well as modulation of the carrier concentration[34,35] made possible by ionic diffusion and charge compensation, therein overcoming Debye screening effects.[34]

Considering the vast arsenal of materials available for opto-electrochemical tuning, it has been particularly challenging to find a continuously tunable material with high index and transparency throughout the visible spectrum, particularly in the blue region. To date, only a few different materials systems have been leveraged for electrochemical tuning of metamaterials, but they either experience high losses in the visible (i.e. Si, metals), or have limited dynamic range (i.e. polymers, WO_3). Titanium dioxide (TiO_2) is a popular material for photonics due to its high index and low absorption coefficient, and while the electrochromic properties of TiO_2 nanoparticles are well known,[150–153] there remain ample opportunities to further harness this phenomenon for structural color tuning. In metasurfaces, the transition metal oxide has found a multitude of applications including planar metalenses,[154–156] perfect reflectors,[157] subtractive color filters,[158] and aberration correction.[159] There has been a demonstration of a tunable TiO_2 metasurface using ion implantation in which the structural color of an array was fully damped,[160] but many applications require functionality beyond amplitude modulation.

Meanwhile, in the electrochemistry community, TiO_2 is a reliable anode material for lithium ion batteries, known for excellent cycle life and minimal volume expansion.[161–165] The reversible reaction is well studied: $TiO_2 + xLi^+ + xe^- \rightarrow Li_xTiO_2$, where x is the mole fraction of Li.[166] Upon Li^+ intercalation up to $x = 0.5$, the tetragonal symmetry of anatase ($I4_1/amd$) is broken, forming orthorhombic $Li_{0.5}TiO_2$ (*Imma*) which is accompanied by ~5% volume change.[166–168] Between $0.05 < x < 0.5$, TiO_2 and $Li_{0.5}TiO_2$ coexist in a two-phase system, resulting in a constant potential during charge and discharge. Insertion of additional lithium is possible for nanostructures and thin films at low current densities, but results in reduced Li^+ ion mobility.[161,166,169,170] To our knowledge at the time of writing, the dielectric function of electrochemically lithiated $Li_{0.5}TiO_2$ (henceforth referred to as LTO) has never been experimentally measured.

Here, we critically evaluate the TiO_2/LTO system as an electrochemical tuning agent for active metamaterials and demonstrate its efficacy for modulation of nanophotonic structures. In contrast to previous studies of electrochromism in TiO_2, the incorporation of resonant nanostructures harnesses both real and imaginary parts of the complex dielectric function to produce vibrant structural color spanning the visible spectrum. We first

demonstrate a simple Fabry-Perot nanocavity, which reflects frequencies of light that satisfy the resonance criteria between two reflective surfaces.[171] In a second demonstration, TiO_2 serves as the dielectric in a metal-insulator-metal (MIM) type gap plasmon metasurface, where enhanced electromagnetic fields[172,173] lead to smaller mode volumes and accelerated switching speeds. This work illustrates how nanophotonic design in conjunction with electrochemically activated media allows flexible control over spectral response.

4.3. Experimental Methods

4.3.1. TiO_2 Film and Device Fabrication

To form samples for ellipsometric characterization, a TiO_2 film was deposited directly onto a silicon wafer via RF magnetron sputtering at room temperature from a target of 99.99% pure TiO_2 in an AJA ATC-2200 sputtering system. The chamber pressure was 3 mT with a deposition height of 110 mm under 45 sccm Ar and 3 sccm O_2. After deposition, films were annealed in a tube furnace at 400 ^oC for 1 hour in air. To make simple Fabry-Perot nanocavities, 50 nm of metallic Ti was deposited on a silicon wafer using electron beam evaporation in an Angstrom Amod multimode deposition chamber. After, 100 nm of sputtered TiO_2 was coated onto the Ti backplane and annealed between 400 – 600 ^oC for 1 hour in air. MIM-type metasurfaces were prepared by sputtering 20 nm of TiO_2 onto a 100 nm aluminum backplane prepared by thermal evaporation on a silicon substrate. Following one hour of annealing at 400 ^oC in air, a positive bilayer PMMA resist was applied via spin coating and baked at 180 ^oC for 90 s. The top layer of pillars was defined using a Raith eLine electron beam lithography system and developed in 1:3 MIBK:IPA. Finally, 50 nm of silver was deposited via e-beam evaporation and excess material was removed by 5 minutes of sonication in acetone.

4.3.2. Electrochemical Measurements

For all electrochemical tests, the electrolyte was 1 M LiClO4 (ACS > 95%, Sigma Aldrich) in propylene carbonate (PC) dried over 4Å molecular sieves for at least 48 hours. All electrochemical cells were assembled in an argon glovebox with < 0.5 ppm O2. To perform cyclic voltammetry and diffusion coefficient measurements, a TiO_2/Ti/Si sample annealed at 400 oC was used as the working electrode in a sealed, three-electrode flooded cell with Ag/AgNO3 reference and platinum counter electrode. The reference electrode solution comprised 0.01 M AgNO3 and 0.1 M TEA-TFB in acetonitrile. TiO_2 films were prepared for ellipsometry and XPS in a two-electrode split cell from MTI using a polished lithium counter electrode and Whatman GF/A glass fiber separator with a constant current discharge rate of 10 $\mu A/cm^2$. Coin cells for cycle life studies were assembled in a similar fashion, with polished lithium anode and glass fiber separator. The optical setup used to execute electrochemical-optical modulation is depicted in Figure S7. Incoming light enters through a transparent ITO-coated glass electrode (Delta Technologies Ltd, sheet resistance 5-15 ohms/sq) which contacts a LiFePO4 cathode (MTI) as a lithium source. The cathode is electrically isolated from the TiO_2-based device by a glass fiber separator soaked in 1 M LiClO4/PC electrolyte.

4.3.3. Material Characterization

Raman spectra were collected using a Thermo Scientific DXR confocal Raman microscope using an 100x objective. Ellipsometry measurements were performed using a JA Woollam M-2000VI. After disassembly in the glovebox, lithiated samples were rinsed in acetonitrile and dried under vacuum before loading into a homemade air-free sample holder designed for ellipsometry measurements at a 60o angle. The lithiated samples were never exposed to air. A Cody-Lorentz model was used to fit the pristine data with a mean square error (MSE) of 1.028, while the lithiated sample data was fit using three Lorentz oscillators and a Drude term.[174] A delta offset was included to compensate for window effects caused by the air-free sample holder. The resulting MSE was 1.369. XPS analyses were performed using an Ulvac-PHI Versaprobe 5000. More information about ellipsometry and XPS measurements is available in the supporting information.

4.3.4. Optical Measurements

Reflectance measurements were performed using a Zeiss Observer A1.m microscope. Light reflected from samples illuminated with a white tungsten halogen light source was collected using a 50x objective and analyzed in a Horiba iHR320 spectrometer (600 lines/mm, blaze = 500 nm, 0.1 mm slit, 0.03 s integration time). Scans were averaged over three accumulations of the Horiba Symphony II silicon CCD detector. Background spectra were acquired from a silver mirror.

4.3.5. Numerical simulations

Numerical simulations were executed using commercial software, CST Studio Suite 2020 using the finite element frequency domain (FD) solver. Fabry-Perot nanocavities were analyzed using a full structure with electromagnetic boundary conditions (Et = 0 at xmin,xmax; Ht = 0 at ymin,ymax) in the frequency regime of 350 – 750 THz. Metasurfaces were analyzed using periodic boundary conditions with period equal to 250 nm in the frequency regime 375 – 1000 THz. In both cases, the background permittivity was 2.0, representing the major solvent component of the electrolyte, propylene carbonate. Optical constants for TiO_2 and LTO were derived from spectroscopic ellipsometry measurements. Other complex permittivities were taken from Johnson and Christy (1974) for Ti,[175] Johnson and Christy (1972) for Ag,[176] Green (2008) for Si,[177] and Querry (1985) for Al2O3.[178]

4.3.6. Ellipsometry

Annealed TiO_2 thin films were analyzed using a three-layer physical model comprising the silicon substrate, a native oxide layer described by the Cauchy equation, and a dense TiO_2 film represented as a Cody-Lorentz oscillator[179,180] with surface roughness. Fitting parameters are shown in Table S1. After lithiation, the film properties are no longer consistent with a Cody-Lorentz model; rather, the data is fit with multiple Lorentz

oscillators and a minor Drude term, reflecting the localized character of electrons in Ti-Ti zigzag bonds that fill the Ti-3dyz levels at the bottom of the conduction band.[168,181] LTO fitting parameters are included in Table S2.

4.3.7. DFT calculations

The optical constants of LTO and TiO_2 were calculated from first-principles using density functional theory with local density approximation (DFT-LDA) as implemented in the Quantum-Espresso code.[182] Calculations were performed using the unrefined primitive cells for $Li_{0.5}TiO_2$[183] and TiO_2.[184] We used the local-density approximation (LDA) exchange-correlation functional with Optimized Norm-Conserving Vanderbilt (ONCV) pseudopotentials from http://www.quantum-simulation.org, constructed using the Perdew–Burke–Ernzerhof (PBE) generalized gradient density functional. For TiO_2, a Hubbard *U* term of 7.5 was added to correct for strong correlation in localized 3*d* and 4*f* orbitals.[185,186] The plane wave cutoff energy was 40 Ry. A *k*-mesh of 4 x 4 x 2 under the Monkhorst-Pack scheme was used to sample the Brillouin zone. For LTO, the plane wave cutoff energy was 50 Ry, and a *k*-mesh of 5 x 5 x 5 under the Monkhorst-Pack scheme was used to sample the Brillouin zone.

The macroscopic complex dielectric function as a function of photon energy was calculated at the independent particle level through solving the Dyson equation for susceptibility, *X*, as implemented in the YAMBO code.[187] The refractive index and extinction coefficient were calculated from ε_1 and ε_2 using the following equations:

$$n = \sqrt{\frac{\left(\sqrt{{\varepsilon_1}^2 + {\varepsilon_2}^2} + \varepsilon_1\right)}{2}}$$

Equation 10

$$k = \sqrt{\frac{\left(\sqrt{{\varepsilon_1}^2 + {\varepsilon_2}^2} - \varepsilon_1\right)}{2}}$$

Equation 11

4.3.8. XPS

After cell disassembly, each sample for XPS analysis was loaded into a glass vial while in the glovebox. The vial was sealed with a cap which then was wrapped in tape to minimize air infiltration. The vials were immediately taken to the XPS lab. Samples were removed from the vials and mounted onto the sample holder by placing an edge of each sample under the head of a steel screw and tightening the screw. The samples were exposed to air for less than five minutes between being removed from the vials and being placed into the intro chamber. The mounted samples were pumped in the intro chamber until the pressure dropped below approximately 1x10-6 torr. XPS analyses were performed using an Ulvac-PHI Versaprobe 5000. Monochromatic Al Kα x-rays (1486 eV), a 100 μm diameter x-ray spot rastered over an approximately 600

μm by 400 μm area, and a takeoff angle of 45 degrees off sample normal were used in each acquisition. Pass energies of 187.7 eV and 23.5 eV were used for the survey and high-resolution acquisitions, respectively. Charge neutralization was accomplished using 1.1 eV electrons and 10 eV Ar+ ions. Binding energies were calibrated to -CH2- type bonding in the carbon 1s spectrum of 284.8 eV.

Though the electronic structure of LTO is rather complex, it has been thoroughly examined in other works[168,181] and the ratio of Ti atoms undergoing a change in oxidation state is a good indicator of the reaction extent.[181,188] The XPS spectra presented in Figure S6 clearly show an additional Ti binding state is introduced upon lithiation of the TiO_2. The new binding state is present at a lower binding energy than TiO_2, indicating that some of the Ti atoms have been reduced. The fraction of Ti atoms present in this reduced state can be estimated by the fraction of the total area under the curve and above the background of the top spectrum. A Shirley background was used Gaussian-Lorentzian peaks to deconvolute the spectrum which indicates that approximately 41% of the Ti atoms are in a reduced state compared to TiO_2 after lithiation.

4.3.9. Color Science

Simulated and experimental spectra were input into a Python script leveraging the Colour Science package[189], Colour 0.3.16, freely available under the New BSD License terms. Tristimulus values were generated from the interpolated spectral distribution using CIE 1931 2 Degree Standard Observer color matching functions (cmfs). Standard illuminant D65 is simulated by the filtered tungsten halogen lamp. The tristimulus values were converted to sRGB to create color swatches that could be displayed on screen. For chromaticity mapping, tristimulus values were converted into CIE xy format and plotted onto the CIE 1931 color space.

4.4. Results and Discussion

4.4.1. Optical properties of electrochemically lithiated TiO_2

In this work, the dielectric properties of TiO_2 are transformed by applying a voltage between the device and a counter electrode, causing lithium ions to reversibly intercalate into the TiO_2. When incorporated into nanophotonic devices, the resulting phase transformation is expected to shift the resonant frequency as shown in **Figure 19**a. To predict the breadth of optical modulation in the proposed configurations, we first experimentally determined the dielectric function of TiO_2 and its lithiated counterpart using spectroscopic ellipsometry. TiO_x films were deposited on silicon wafers via RF magnetron sputtering, and subsequently annealed in air at 400ºC to yield anatase TiO_2,[179,180,190–193] confirmed through Raman spectroscopy (**Figure 20**). Spectroscopic ellipsometry was used to determine the refractive index (n) and absorption coefficient (k) and the results are presented in **Figure 19**b-c, respectively. A refractive index of 2.42 at 650 nm is consistent with other reports of annealed TiO_2.[154,155,180] The raw ellipsometry data (**Figure 21**) was fit with an MSE of 1.082 using the fit described in the experimental methods. The absorption coefficient is negligible throughout

the visible spectrum, though it increases at lower wavelengths as photon energy approaches the band edge.

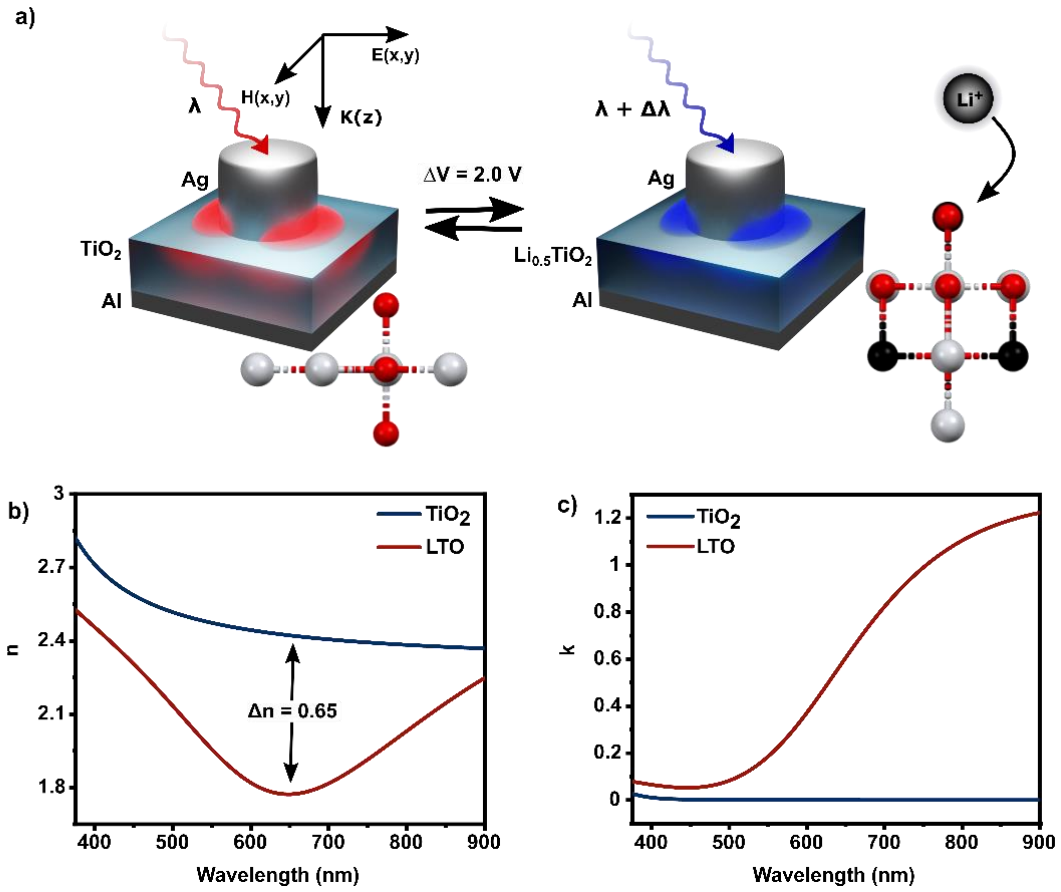

Figure 19: Concept of electrochemical modulation using the TiO_2/LTO materials system. A) Schematic depiction of modulation mechanism, showing the change in resonant wavelength of gap plasmon structures caused by lithium ion intercalation in TiO_2. Crystal structures for anatase TiO_2[183] and orthorhombic LTO[184] were visualized using Mercury[194]. B) Change in refractive index and C) absorption coefficient derived from ellipsometry measurements.

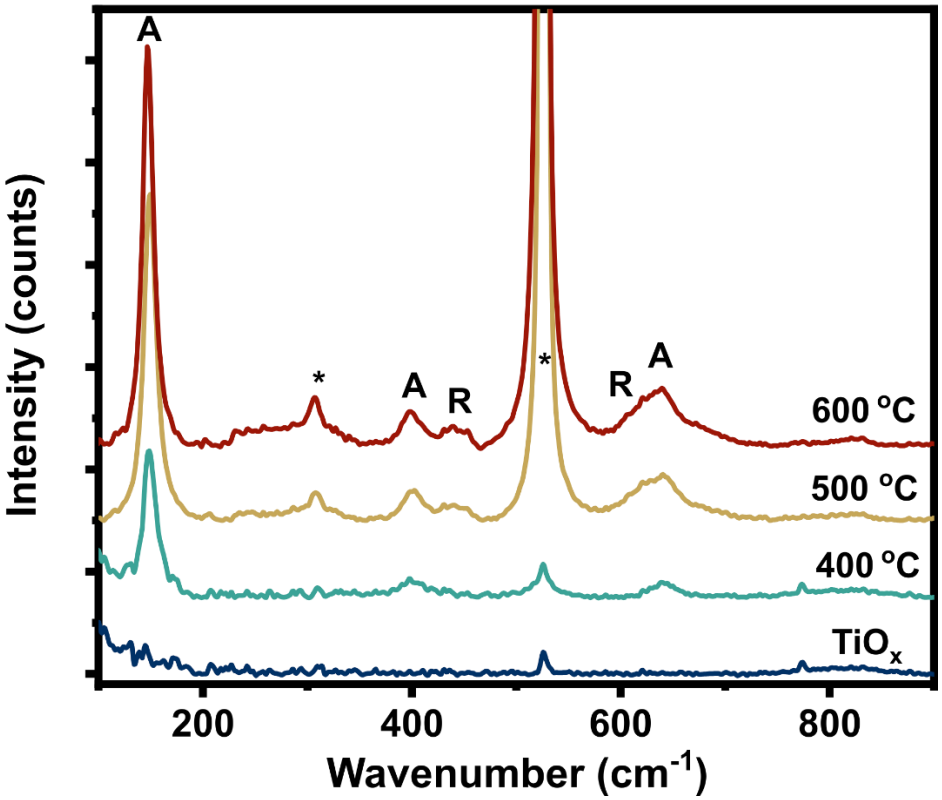

Figure 20: Raman spectra for 100 nm TiO_2 films sputtered on titanium metal evaporated on silicon wafer substrates and annealed at various temperatures for 1 hour each. Temperatures above 400°C lead to rapid oxidation of the 50 nm metallic Ti backplane, therein enhancing the signal of vibrations in the underlying Si wafer,[193,195] indicated with asterisks. The anatase and rutile phases are identified by "A" and "R" respectively.

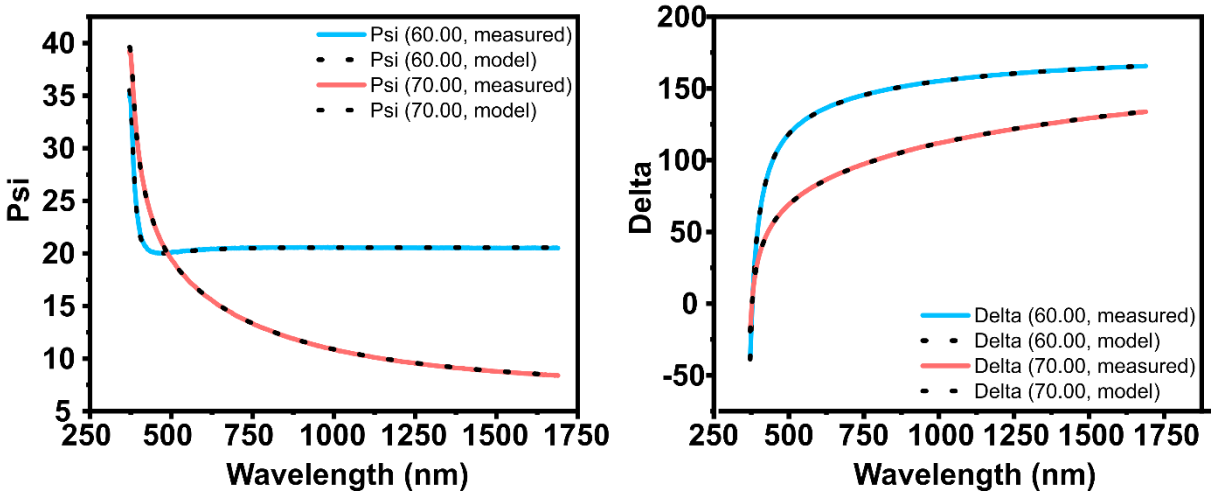

Figure 21: Raw ellipsometry results for TiO_2 on silicon wafer.

Significant modification of the refractive index and extinction coefficient was achieved through electrochemical lithiation of anatase TiO_2. Orthorhombic Li_xTiO_2 (LTO) was formed through ambient temperature galvanostatic discharge of anatase in 1 M $LiClO_4$ electrolyte to a capacity of 168 mAh.g-1, corresponding to x = 0.5, at which point the sample was rinsed in dry acetonitrile and transferred directly into a homemade air-free ellipsometry compartment inside a glove box. The raw ellipsometry data (**Figure 22**) was fit with an MSE of 0.993, resulting in a dip in refractive index with a minimum of 1.77 at 650 nm, generating a maximum shift of $\Delta n = 0.65$ at 649 nm ($\Delta\varepsilon_1 = 3.15$ at 707 nm), likely related to the interband transitions of localized electrons previously identified at 700 nm (1.77 eV) by Wagemaker et al.[181] Nearing the band gap, absorption remains very low due to the Moss-Burstein effect,[196] suggesting the possibility of high-efficiency, tunable metasurfaces across the entire visible spectrum. For reference, the absorption coefficient of Li_xTiO_2 with x = 0.5 is 50% less than that of the popular transition metal oxide, Li_xWO_3, with x > 0.38 at blue wavelengths.[197,198] The resulting values of n and k are in agreement with optical properties extracted from DFT calculations, as shown in **Figure 23**. The chemical underpinnings of the observed optical transitions were verified using x-ray photoelectron spectroscopy (XPS), revealing that approximately 41% of the Ti atoms are in a reduced state after lithiation (**Figure 24**).

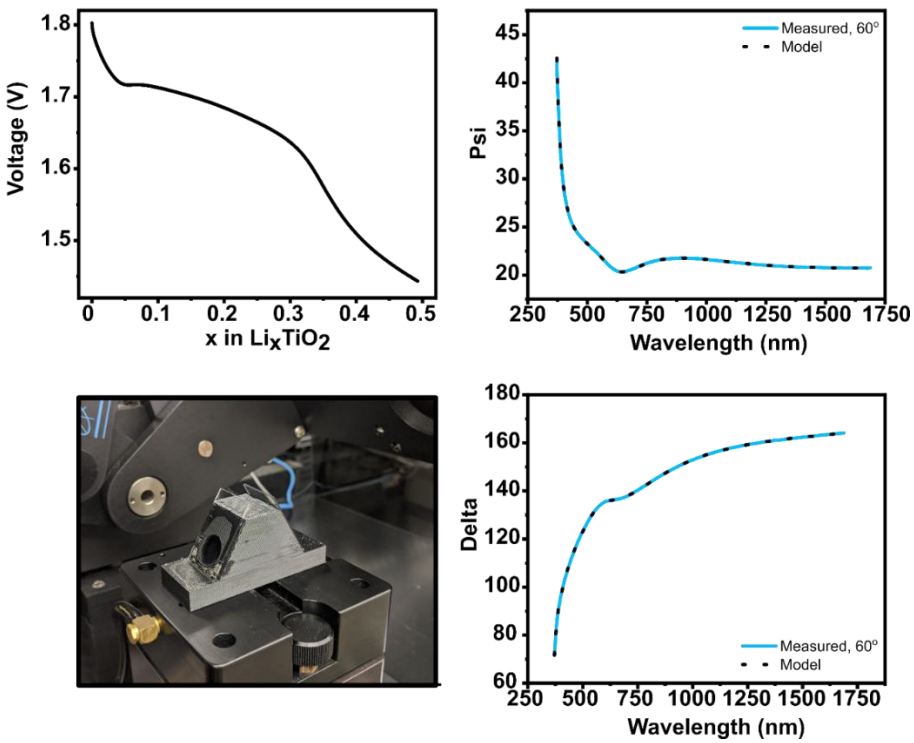

Figure 22: Method of acquiring ellipsometry data to extract complex refractive index of LTO. Galvanostatic curve for anatase TiO_2 samples on silicon wafer discharged at 1 μA/cm^2 (top left); air-free ellipsometry cell for measuring optical properties of LTO without exposure to oxygen or water (bottom left); raw ellipsometry results for resulting LTO on silicon wafer at an angle of 60° (right).

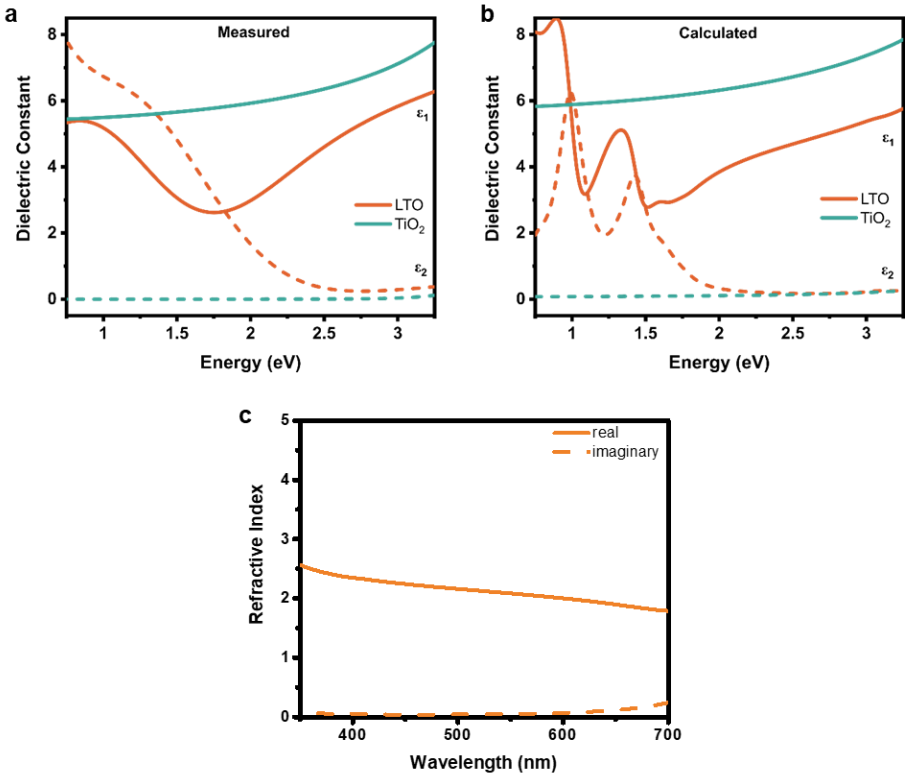

Figure 23: Real and imaginary parts of the dielectric constants of LTO and TiO_2 extracted from ellipsometry data (A) compared to the dielectric constants calculated using DFT (B). Data from B is also represented in terms of wavelength and refractive index in (C).

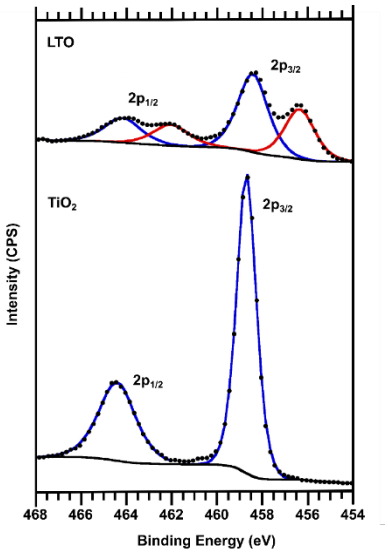

Figure 24: XPS analysis of pristine and lithiated TiO_2 films, 100 nm on Ti backplane.

4.4.2. Demonstration: Fabry-Perot Cavities

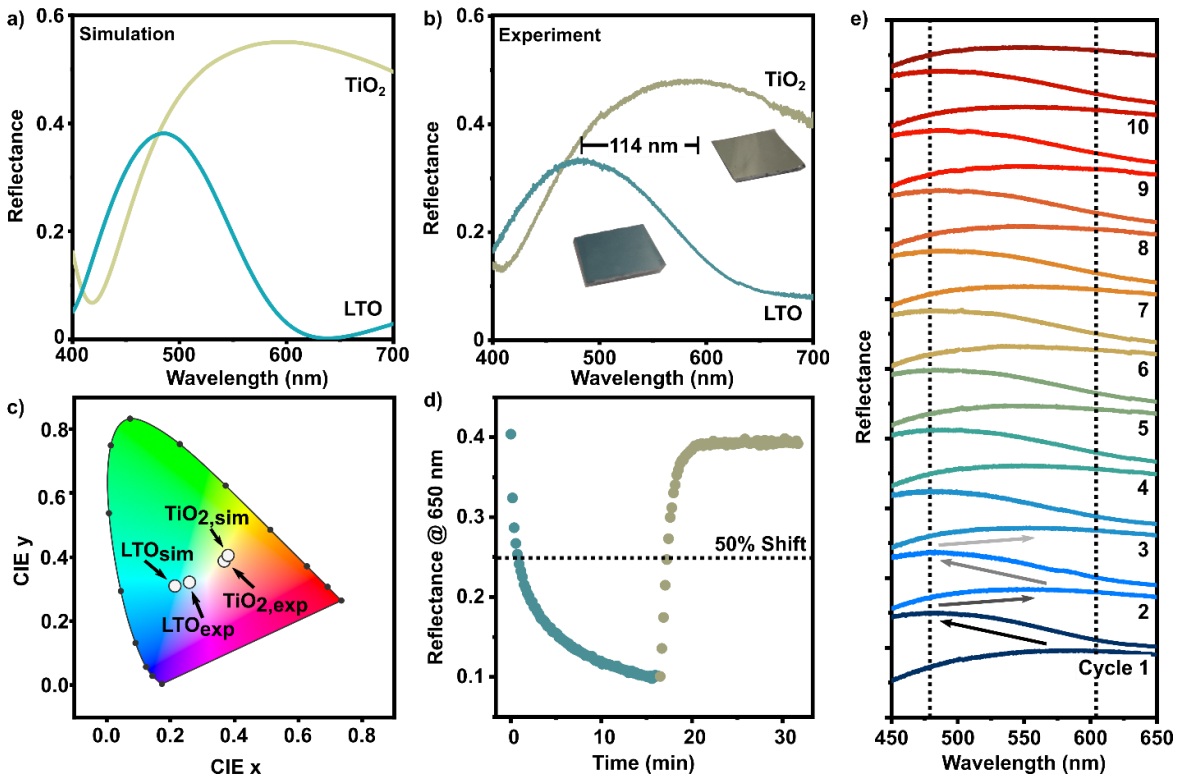

Figure 25: Performance of Fabry-Perot nanocavities in optical cell. A) Theoretical reflectance spectra for a cavity comprised of TiO_2 versus LTO film, simulated using measured optical constants. Line colors represent color calculated from spectra. B) Experimental reflectance spectra for pristine film and lithiated film after galvanostatic discharge to -2 V. Line colors represent color calculated from spectra. C) CIE 1931 chromaticity map with points representing experimentally-measured and simulated color of TiO_2 and LTO films. D) Speed of color change determined by plotting the magnitude of reflectance at 650 nm acquired every 10 s during potentiostatic hold at -2 V. E) Reversibility of spectral shift over 10 cycles.

With the aim of demonstrating the dynamic tuning capabilities of anatase TiO_2 in simplest form, basic Fabry-Perot nanocavities were fabricated through the deposition of 100 nm TiO_x onto a titanium metal backplane, which was subsequently annealed at 400°C in air to form anatase TiO_2. Reflections off the TiO_2-air interface and the metal backplane interact in a weakly resonant cavity that appears gold in the pristine state. Finite element frequency-domain (FD) simulations executed using the experimentally-determined dielectric functions for TiO_2 predicted broadband reflection of visible wavelengths greater than 500 nm in the pristine state, with a local minimum around 410 nm due to destructive interference in the cavity, as shown in **Figure 25**a. By replacing TiO_2 with the lower-index LTO and increasing thickness by 5% to represent volume expansion associated with the phase transformation,[169,199] new resonance conditions dictated reflection of blue-green wavelengths, peaking around 490 nm. In practice, spectral reflections in the pristine state agreed closely

with simulations, despite being slightly damped by interfacial losses in the optical cell (see **Figure 26**) and finite roughness of the TiO_2 surface. The experimental results shown in **Figure 25**b agree with simulations, therein confirming the dielectric function for LTO derived from ellipsometry measurements. For the first discharge, the full extent of tunability was achieved by slowly discharging at a constant current of 1 $\mu A/cm^2$, generating a 114 nm blue shift as the optical thickness of the cavity is decreased. Notably, the maximum peak intensity of the lithiated film experienced a reduction of 38.7%, in line with predictions, supporting the selection of the TiO_2/LTO system for highly efficient tuning across the visible spectrum. The chromaticity was calculated from the reflectance spectra and mapped in the CIE 1931 color space in **Figure 25**c. More information about color identification and mapping is provided in the Supporting Information. The color purity, represented as the radial component of chromaticity, is slightly lower than that predicted through simulation, likely due to the nuances of nanostructured anatase when operated at high rates. For very small particles, high surface energy may prohibit phase coexistence, causing individual grains to transform instantaneously rather than proceeding through the film as a uniform phase front.[170] This behavior results in an effective mixing of TiO_2 and LTO properties, broadening the resonance and reducing the color purity. Such phenomena can be mitigated by slowing the reaction or by using thicker films with bulk properties.

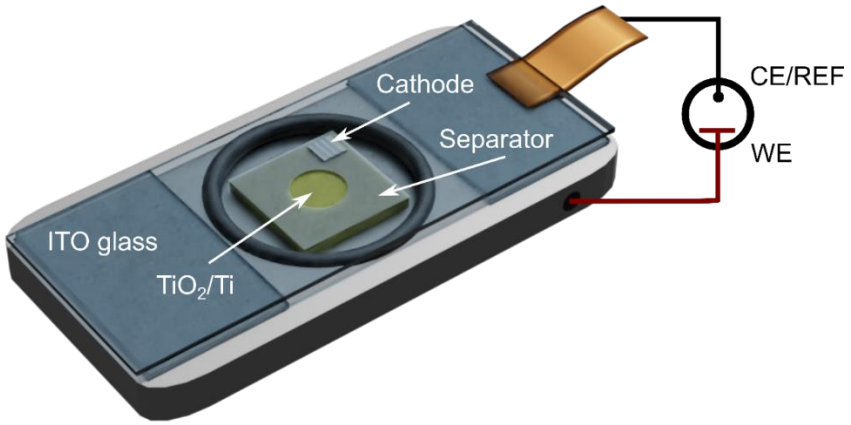

Figure 26: Schematic of optical cell used for in-situ reflectance measurements.

The greatest rate of change in reflectance spectra is observed in the early stages of intercalation (**Figure 25**d). Immediately after applying voltage, a buildup of capacitance at the interface gives way to the solid solution regime, followed by rapid nucleation of the LTO phase. Given the small nucleation energy barrier, the phase boundary motion is fast compared with lithium self-diffusion, thus the reaction rate slows as the system transitions into a diffusion-limited regime.[170] Accordingly, a large initial shift in peak wavelength after the first 30 seconds is succeeded by more and more subtle adjustments over the total holding period of 15 minutes. For insertion, 50% of the total reflection change is achieved within the first 50 s. Upon reversal, the 50% benchmark is achieved in just over 40 s. Such asymmetry has been evaluated in other works[166,200] and is theoretically

attributed to a higher energy barrier across the phase boundary during insertion.[166]

Although significant spectral shifts are possible in short times, the device is cycled to the extent of its capability using potentiostatic holds at –2 V (insertion) and 0 V (extraction) for up to 15 minutes each (**Figure 25**e). In doing so, we find that the device demonstrates full optical reversibility over the first 10 cycles, following an initial first cycle loss of only 5.5% the total reflected power. In the fourth and tenth cycles, the peak-to-peak shifts in reflectance were 62.9 nm and 61.2 nm, respectively, indicating negligible additional loss after the first few cycles. It should be noted that the external bias of only 2 V is an order of magnitude less than the voltages applied to devices based on state-of-the-art phase change materials.[201–203] Furthermore, the lithiated and delithiated states were highly stable after 20 minutes under open circuit conditions, suggesting the device is non-volatile and exhibits bistability (**Figure 27**).

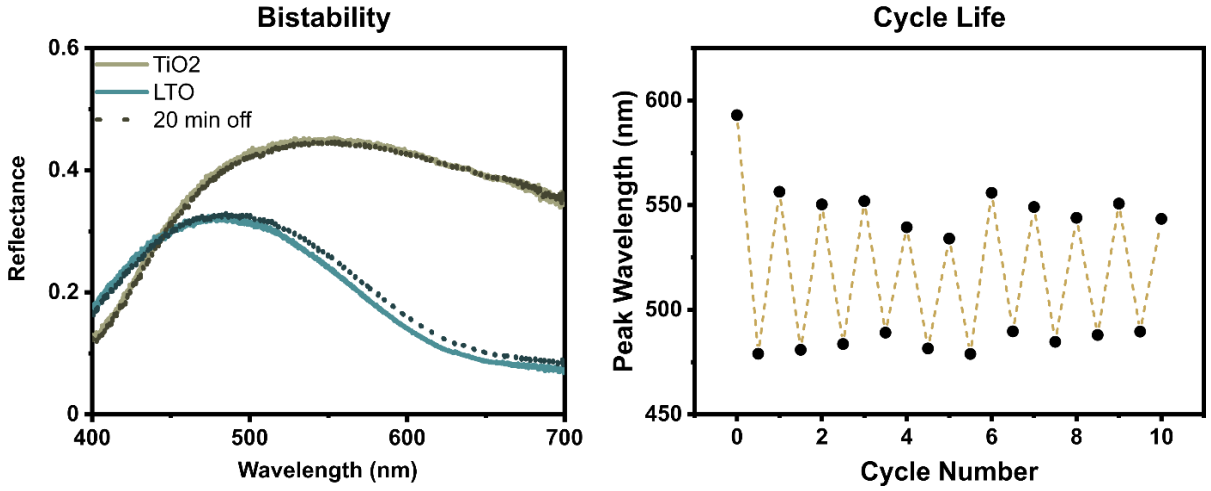

Figure 27: Bistability (left) and optical cyclability (right) from in-situ optical testing of Fabry-Perot nanocavities.

To better understand the limits of speed and cyclability for this material system, we measured the cycle life and diffusion coefficient of lithium in the sputtered TiO_2 thin films. The capacity retention for a 20 nm anatase film on an aluminum backplane cycled in a coin cell versus LFP is shown in **Figure 28**a. After 400 cycles of galvanostatic charge and discharge at 3 $\mu A/cm^2$ (30 minutes per cycle) the lithium capacity remains stable, despite initial capacity loss associated with solid electrolyte interphase formation and volume expansion. Following this, the capacity is constant over the duration of cycling with a slight increase attributed to fine adjustments in microstructure that allows accommodation of additional lithium ions. This observation is consistent with the previously discussed opto-electrochemical cycling studies of Fabry-Perot nanocavities. The excellent electrochemical cyclability of anatase thin films is expected to translate into dynamic photonic devices which maintain full modulation depth over many switching cycles.

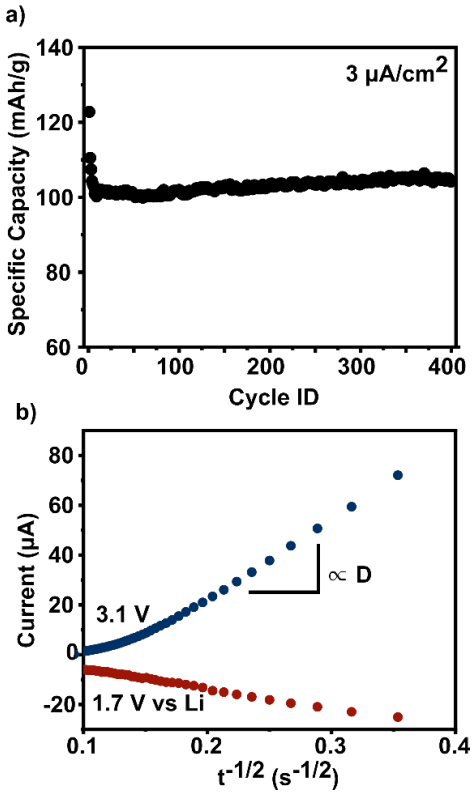

Figure 28: Electrochemical characterization of TiO_2 films. A) Cycle life of 20 nm TiO_2 films on Al backplane cycled at 3 μA/cm^2 in coin cells versus LFP cathode. B) Results of potential step experiment for 100 nm TiO_2 films on Ti in 3-electrode flooded cell with platinum counter electrode and $Ag/AgNO_3$ reference electrode. The slope of the curve is proportional to the diffusion coefficient.

Switching speed is a critical parameter for most optoelectronic devices. In electrochemical systems, the speed will primarily depend on film thickness and the intrinsic diffusion coefficient. The diffusion coefficient was derived from the transient current response of a planar electrode to an instantaneous potential step,[68,204,205] and the results are shown in **Figure 28**b. When stepped from the open circuit voltage to -1.5 V vs $Ag/AgNO_3$ (1.67 V vs Li/Li^+), the slope of current versus $t^{-1/2}$ is predominantly linear, curving slightly with increasing time to indicate a minor dependence of diffusion characteristics on lithium content.[166,206] Taking the average linear slope (R^2 = 0.997), the diffusion coefficient for lithium insertion was calculated as 9.78 x 10-12 cm^2/s. On the reverse step, a much higher current at early times is associated with a greater diffusion coefficient of 9.31 x 10^{-11} cm^2/s. These values agree with other measurements of lithium diffusion in anatase TiO_2[166,169,206] and establish an upper boundary on speed through the characteristic diffusion time, $\tau_d = L^2/D$, where L is the film thickness. For a 100 nm film, the characteristic diffusion time is 10.2 s for insertion and 1.07 s for extraction, though speed can be dramatically improved by reducing thickness; for a 20 nm film, the characteristic diffusion time is 0.409 s for insertion and 0.043 s for extraction. As this represents the ideal (upper bound) for speed, the slightly longer measured switching speed (**Figure 25**d) is attributed to sources of impedance in the opto-electrochemical cell, particularly non-negligible ionic resistance through the separator and electrolyte.

4.4.3. Demonstration: Gap Plasmon Metasurface

In order to realize faster actuation times, the same material system was incorporated into a gap plasmon metasurface. For the metal-insulator-metal configuration with patterned nanopillars atop a thin dielectric layer, strong absorption in the gap is enabled by the resonant behavior of excited gap surface plasmons.[207,208] 20 nm thick TiO_2 films were chosen as the dielectric layer between patterned silver nanopillars and an aluminum backplane, simultaneously optimizing coupling and reducing the diffusion path length of Li+ ions to enhance reaction speed. The final unit cell design is depicted in **Figure 29**a. For all tests, the period of the patterned layer remains a constant 250 nm and the pillar height is 40 nm. As pillar diameter varies from 60 nm to 90 nm, FD simulations predict a red-shift in the reflectance minimum (**Figure 29**b), as the resonance condition for counter-propagating gap surface plasmon polaritons dictates destructive interference at increasingly long wavelengths.[208] As shown in **Figure 29**b, inset, the electric field is concentrated in the gap between pillar and backplane at the frequency of minimum reflectance. The reflected color is thereby tuned from gold to brown with increasing pillar diameter. The positions of local minima at shorter wavelengths are not strongly dependent on resonator width due to near-field coupling between neighboring surface plasmon polaritons. Considering the case of 70 nm pillar diameter, changing LTO content was simulated as a uniform phase front propagating along the depth of the film in **Figure 29**c. As the film is transformed from anatase TiO_2 to 100% LTO, the reflectance minimum experiences a significant blue-shift of 135 nm, changing the expected color from gold to green. An SEM image of the fabricated metasurface is included in **Figure 29**d. In experimental demonstrations (**Figure 29**e), the position of the gap plasmon resonances are consistent with expectations for the lithiated state, but the pristine spectra are slightly blue-shifted, potentially stemming from diffusion of silver into the TiO_2 thin film during e-beam evaporation.[209,210] Due to the sensitivity of plasmon polaritons to the environment at the metal-dielectric interface, this introduces an offset in the initial state of the device. Accordingly, the spectral shifts in reflectance minima are 59 nm, 39 nm, and 37 nm for the 80 nm, 70 nm, and 60 nm diameter pillars respectively. Though the minima for the 90 nm pillars are cut off by the detector window, there is a significant blueshift in the peak edge measuring 108 nm. **Figure 29**e shows that the most significant shift occurs in the first few seconds with diminishing returns at longer time scales. When considering the change in reflectance over time at 650 nm, 50% change is realized in 7 s, a timescale which compares favorably with similar devices constructed using Li_xWO_3.[34,197] Though the transition is still slower than the measured diffusion coefficient would suggest, the speed of ion transport is likely limited by elements of device construction and can be optimized using different cell components and geometries. These results lay the foundation for applications of the TiO_2/LTO material system in tunable nanophotonic devices for the visible spectrum.

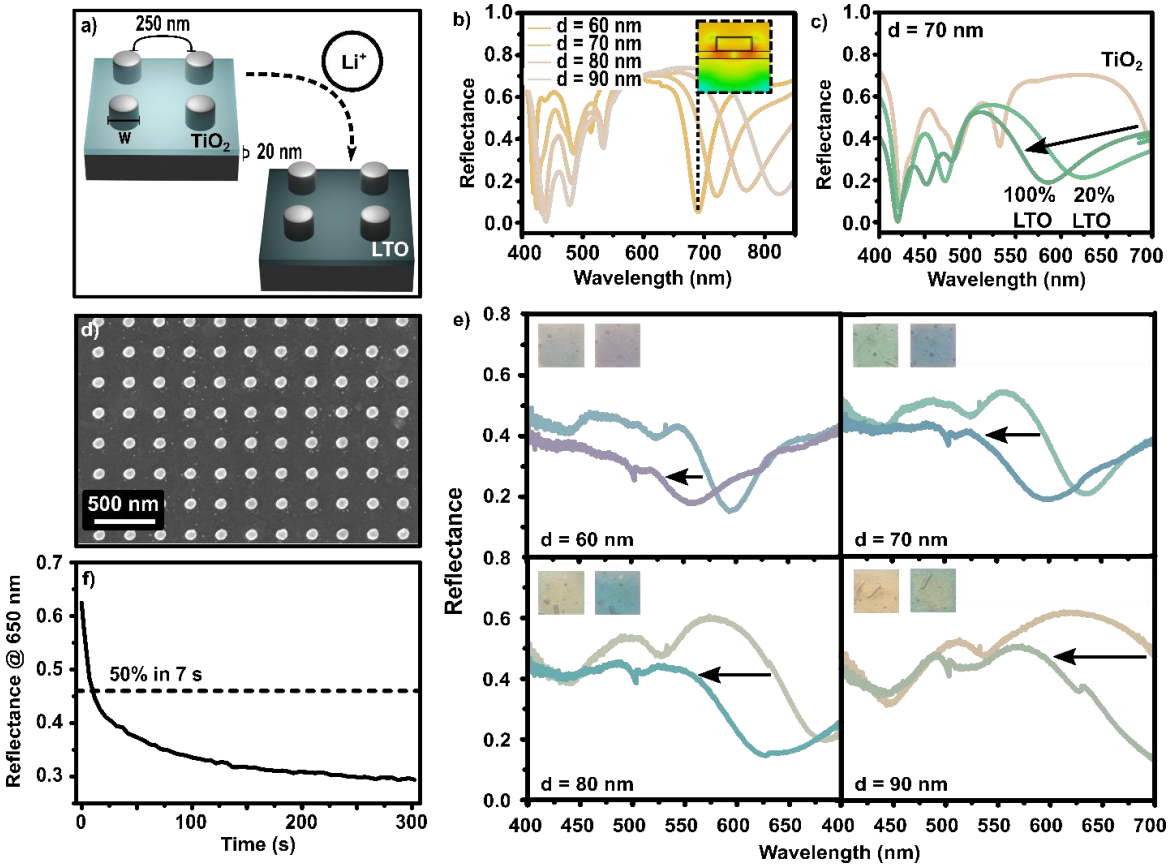

Figure 29: Performance of gap plasmon device in optical cell. In all plots, line colors represent color calculated from spectra. A) Schematic of device unit cell before and after lithium intercalation. B) Simulated reflectance spectra for varying pillar diameter from 60 – 90 nm. Inset shows electric field distribution at the frequency corresponding to the peak minimum. C) Simulated reflectance spectra for 70 nm diameter pillars with LTO content ranging from 0 – 100%. D) SEM image of metasurface acquired at 5 kV, magnification = 100 kx, working distance = 5.0 mm. E) Experimentally measured reflectance spectra showing shifts for four different pillar diameters after galvanostatic lithiation. Insets are photographs of the arrays in each state. F) Speed of reflectance change at 650 nm.

4.5. Conclusions

As shown here, TiO_2 is an attractive material for dynamic tuning of photonic devices in the visible spectrum, leveraging a reversible electrochemically controlled phase transformation at biases less than 2V. This results in a change in refractive index of 0.65 while maintaining a small absorption coefficient at blue wavelengths. These properties, combined with measured diffusion coefficients on the order of 10^{-11} cm^2/s and stable cycling of lithium at high rates, enable this material system as a suitable platform for active modulation. Employed in nanophotonic structures, this enables resonance tuning exceeding 100 nm. Employed as all-dielectric metasurfaces, this material system could open new doors in applications such as anti-counterfeiting, holograms, or tunable aberration correction.

Chapter 5: Colloidal Fabrication of Hierarchical TiO_2 Metasurfaces for Dynamic Color Tuning

5.1. Introduction

Having shown that electrochemical reactions are a powerful tool for generating permittivity changes in metal oxides, I set out to address the barriers to practical implementation of this technology: speed, scalability, and environmental stability. In this chapter, I evaluate hydrogen as a more agile ion for electrochemical modulation of TiO_2-based metasurfaces.

5.2. Background

Reducing the power consumption of electronic devices is a key element of the energy transformation required to ensure global sustainability. In an age of ubiquitous access to information, reflective displays are a promising low-power alternative to emissive displays for applications ranging from wearable devices and e-paper to superlarge wall displays. Though the field remains fraught with challenges, major barriers to widespread integration, including low brightness and limited dynamic range, may be surmounted through the development of structural color technologies.[41] As opposed to pigmentation, structural color decouples perceived color from intrinsic properties through engineered architectures.[211,212] This dramatically expands the material selection space to low-loss and environmentally durable substances with photobleaching resistance.

Metamaterials are a particularly attractive platform for structural color generation due to their high spatial resolution and improved range of viewing angles. These subwavelength arrays of scatterers can be designed for extremely high field confinement to maximize optical response to subtle stimuli according to first order perturbation theory.[22,213,214] While metallic resonators supporting a localized surface plasmon resonance (LSPR) can be highly sensitive to changes in the dielectric environment, particularly when the modes are geometrically confined,[214,215] they also tend toward high dissipative losses at visible frequencies. In contrast, dielectrics and semiconductors have wide bands of transparency and can support additional magnetic modes.[16] The associated Mie resonances may be localized to the interior of a dielectric nanostructure, enhancing sensitivity to internal changes in permittivity caused by electrical gating,[28–30,216] doping,[217] or phase transformations.[32,33]

With a band gap of 3.2 eV, high refractive index (2.5 at 450 nm), and negligible loss throughout the visible spectrum, titanium dioxide (TiO_2) is an ideal selection for efficient metasurfaces at visible frequencies[218–221]; however, there have been few demonstrations of the tunability required for reflective display technologies[222–224]. Wu *et al* showed intensity modulation greater than 80% over 4 minutes of hydrogen ion implantation in TiO_2 nanopillars[224], but the requirement for an inductively coupled plasma chamber prohibits practical device integration. Alternatively, reversible hydrogen doping can be accomplished using electrochemical[225–229] or photochemical[230–232] methods compatible with on-demand modulation.

By compensating charge buildup with positive ions, electrochemical redox reactions circumvent Debye screening to achieve high dopant concentrations at biases less than 2 V.[34,36,233] In prior work, we established the efficacy of electrochemical methods for dynamic tuning of gap plasmon metasurfaces incorporating TiO_2, but the system was limited by switching speed and the atmospheric sensitivity of Li^+ electrolytes.[215] Here, we leverage reduced diffusion path lengths in nanoparticles in conjunction with the higher diffusion coefficient[166,234] of hydrogen in anatase TiO_2 to enhance the speed and cyclability of a dynamic TiO_2 metasurface fabricated via scalable colloidal processing methods. By forming hierarchical photonic structures from pure TiO_2 nanoparticles, we also access photodoping mechanisms for all-optical switching capability, circumventing the need for complex circuitry which can become preventative for very small, very large, or three-dimensional devices. The system is completely reversible and incorporates environmentally-stable electrolytes. The advantages of in-situ photochemical and electrochemical doping of TiO_2 are highlighted using two forms of resonant cavity: the Fabry-Perot configuration for broadband response, and the all-dielectric metasurface for extreme field confinement and modulation depth.

5.3. Experimental Methods

5.3.1. Nanoparticle synthesis

TiO_2 nanoparticles were synthesized by controlled hydrolysis of titanium tetraisopropoxide (TTIP) (97+%, Alfa Aesar) in deionized water adjusted with 0.1 M nitric acid (HNO_3, Fisher Chemical) based on a procedure by Prathapani et al[235], which was originally modified from Choi et al[236]. 36 g of 0.1 M HNO_3 was prepared from stock solution in a round bottom flask suspended in an oil bath. While stirring at room temperature, 6 g of TTIP was added dropwise to the acidic solution. Then, the temperature was raised to 80°C, where it was maintained for 12 h before cooling to room temperature. Depending on the fabrication step, nanoparticles were used as-is or diluted with 1-3 parts ethanol for processing.

5.3.2. Nanoparticle characterization

To obtain crystalline phase information, nanoparticles were dried at 75°C in a vacuum oven and then annealed in a tube furnace at 500°C for 30 minutes in air. Powder diffraction data was obtained using a Rigaku SmartLab X-ray diffractometer with Cu Kα source. Optical absorption was evaluated using a Cary 5000 UV-Visible spectrophotometer with a scan rate of 600 nm/min. To measure the response of nanoparticles to UV light, a nanoparticle film was spin coated at 1000 RPM for 60 s onto an ITO glass slide, then annealed for 30 minutes at 500°C in air. The coated slide was inserted into a polystyrene cuvette, then the cuvette filled with glycerol. For both the sample cuvette and the reference cuvette, the side facing the light source was covered with polyimide tape with a 4 mm diameter hole as an aperture. Between measurements, the sample was illuminated with a collimated beam of 365 nm UV radiation focused onto the 4 mm aperture. The UV illumination source was a Thorlabs M365LP1 mounted LED 21.0 $\mu W/mm^2$. For ellipsometry using a JA Woollam M-2000VI spectroscopic ellipsometer, nanoparticles were spin coated directly on a cleaned glass slide to simplify analysis

and modeling. Annealed TiO_2 thin films were analyzed using a two-layer physical model comprising the SiO_2 substrate, and an effective medium approximation of a porous TiO_2 layer with air-filled voids. TiO_2 was represented as a Cody-Lorentz oscillator. [179,180]

5.3.3. Metasurface fabrication

Substrates for fishnet metasurfaces were prepared by sputtering 10 nm of ITO via RF magnetron sputtering at room temperature from a target of 99.99% pure ITO in an AJA ATC-2200 sputtering system. The chamber pressure was 5 mT with a deposition height of 110 mm under 20 sccm Ar. After deposition, films were annealed by rapid thermal annealing at 500°C. To make simple Fabry-Perot nanocavities, 50 nm of metallic Ti was deposited on a silicon wafer using electron beam evaporation in an Angstrom Amod multimode deposition chamber. Then, a positive bilayer PMMA resist was applied via spin coating and baked at 180 °C for 90 s. The fishnet structure was defined using a Raith eLine electron beam lithography system and developed in 1:3 MIBK:IPA. Following development, colloidal TiO_2 nanoparticles in DI water diluted with one part ethanol were dropped on top of the structure. Excess material was removed by spin coating at 2000 RPM for 60 s and drying at 150°C for 5 minutes. Liftoff was accomplished by sonicating in acetone for 10 minutes. Finally, the structures were annealed at 500°C in air for 30 minutes.

5.3.4. Optical measurements

For reflectance measurements, samples were illuminated with a white tungsten halogen light source using a 50x objective and analyzed in a Horiba iHR320 spectrometer (300 lines/mm, blaze = 500 nm, 0.1 mm slit, 0.03 s integration time). Scans were averaged over three accumulations of the Horiba Symphony II silicon CCD detector. Background spectra were acquired from a silver mirror. When required, electrochemical modulation was executed using a Metrohm potentiostat in the presence of 0.1 M H_2SO_4 in 50/50 DI water and glycerol by volume. The counter electrode was Pt foil and the reference electrode was Pt wire. Reflectance spectra were baselined in post-processing to clarify modulation depths.

5.3.5. Numerical simulations

Numerical simulations were executed using commercial software, CST Studio Suite 2020 using the finite element frequency domain (FD) solver. Fabry-Perot nanocavities were analyzed using a full structure with electromagnetic boundary conditions ($E_t = 0$ at x_{min}, x_{max}; $Ht_t = 0$ at y_{min}, y_{max}) in the frequency regime of 350 – 750 THz. Metasurfaces were analyzed using periodic boundary conditions in the frequency regime 375 – 1000 THz. In both cases, the background permittivity was 1.97, representing the average permittivity of a 50/50 volume-basis mixture of water and glycerol. Optical constants for TiO_2 and ITO were derived from spectroscopic ellipsometry measurements. The complex permittivities of Ti was taken from Johnson and Christy. [175]

5.4. Results and Discussion

5.4.1. Optical and electrochemical tunability of TiO_2 nanoparticles

In this work, dynamic modulation of all-dielectric metasurfaces is achieved using electrochemical and photo-induced doping methodologies, both compatible with on-demand switching of photonic devices. The mechanism of electrochemical reductive doping is depicted schematically in **Figure 30**a. Electron transfer from the cathode is compensated by the uptake of protons from the electrolyte, thereby reducing Ti^{4+} to Ti^{3+} according to the reaction[227,228,237]

$$Ti^{IV}O_2 + H^+ + e^- \leftrightarrow Ti^{III}(O)(OH^+)$$

where the process is easily reversed by applying a positive bias voltage to re-oxidize the TiO_2, restoring the Ti to its original valence state.[228,229]

While electrochemical switching operates on a pixel-by-pixel basis, optical addressing of arbitrary regions may be enabled through photodoping, **s**chematically illustrated in **Figure 30**b. In general, observed increases in optical absorption are attributed to the photoexcitation of electron-hole pairs, where the hole is scavenged by an adsorbate and the electron is compensated by reduction of Ti^{4+} to Ti^{3+} via oxygen vacancy formation[230,231] along with potential incorporation of hydrogen in the anatase lattice.[230] Here, glycerol is chosen a hole scavenger due to its combined trapping energy and adsorption-induced surface dipole effect, which are computationally determined by Valentin and Fittipaldi to be more effective than other organic scavengers.[238] The photoreduction process may be reversed by exposing the TiO_2 to oxygen[230,231] or pairing with electrochemical oxidation for on-demand switching.

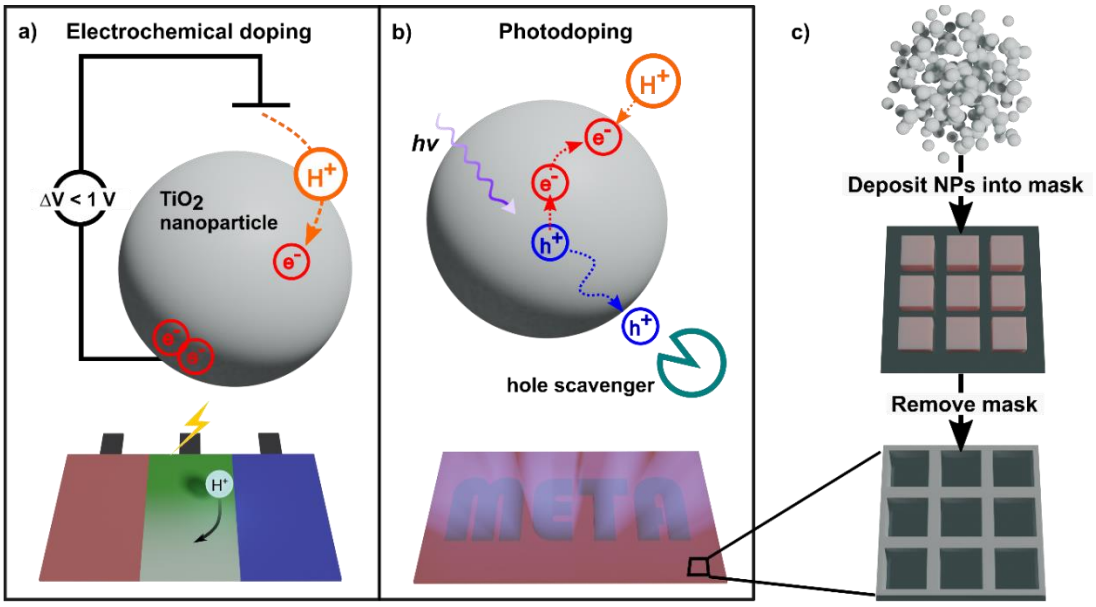

Figure 30: Schematic representation of modulation strategies applied for dynamic tuning of colloidal TiO_2

metasurfaces. A) Electrochemical doping mechanism and potential pixel-by-pixel application in reflective display; B) Photochemical doping mechanism, highlighting opportunities for optical addressing of arbitrary patterns; C) Strategy for fabricating dielectric metasurfaces from colloidal solutions.

For effective optical addressing of dynamic metasurfaces, absorbance should be maximized by using TiO_2 nanoparticles with radii on the order of the exciton diffusion length of anatase, approximately 3.2 nm.[239] Nanostructured electrodes are also known to exhibit enhanced rate capability in electrochemical devices.[240] Accordingly, hierarchical metasurfaces were fabricated from solution-based deposition of TiO_2 nanoparticles as shown in **Figure 30**c. Briefly, a structure is defined in positive photoresist using electron beam lithography (EBL). Following development, a colloidal nanoparticle solution is deposited into the pattern by spin coating and dried thoroughly before liftoff. Unlike recent developments in nanoimprint lithography, this approach avoids the incorporation of UV curable resins that may impede photochemical activity while still eliminating the need for lengthy vacuum-intensive deposition methods and reactive ion etching. After liftoff, the films are annealed at 500ºC in air for 30 minutes.

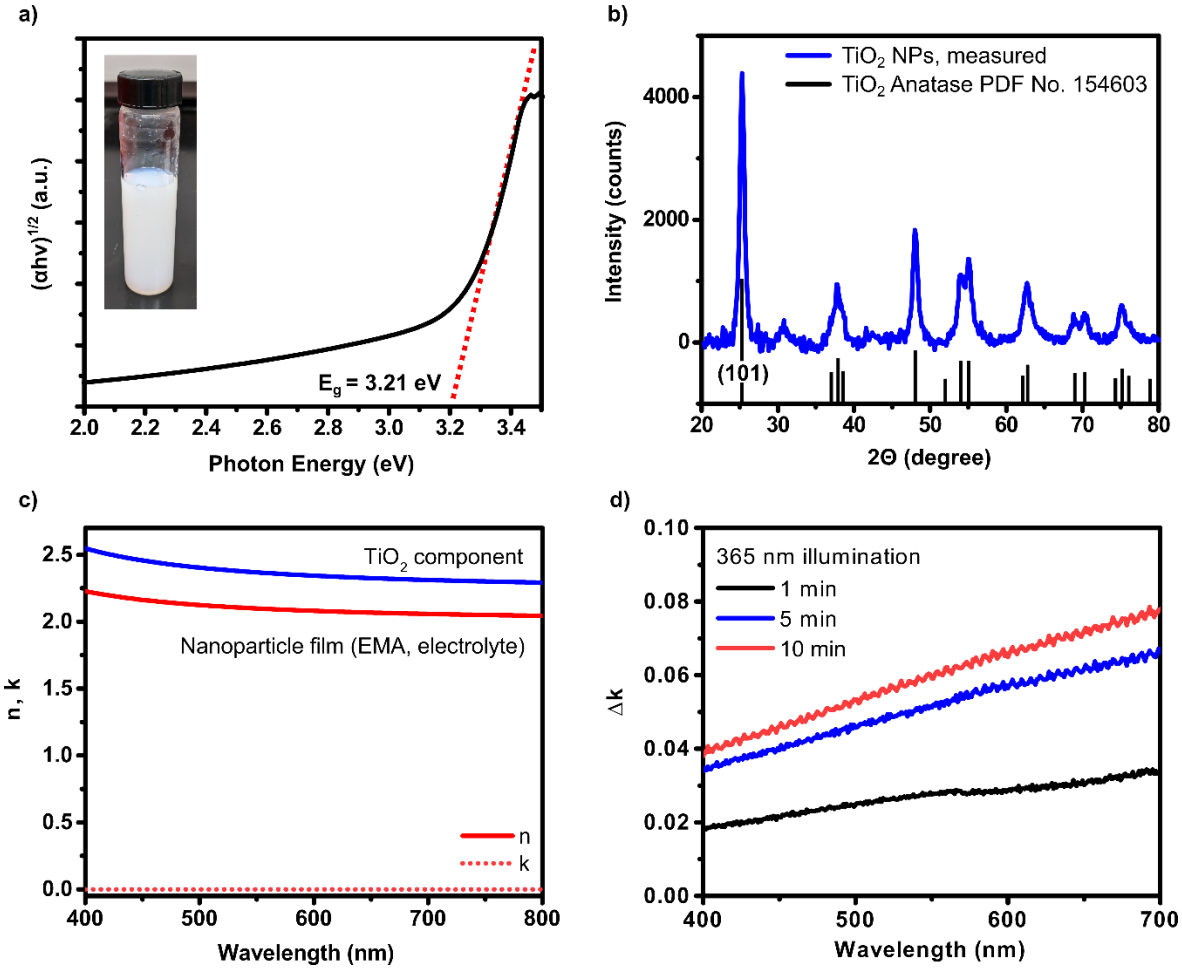

Figure 31: Characterization of TiO_2 nanoparticles. A) Tauc plot derived from UV-Vis absorption spectrum of the colloidal TiO_2 suspended in water; B) X-ray diffraction of dried TiO_2 powder annealed at 500ºC for 30 minutes in air, compared to PDF No. 154604 for anatase TiO_2; C) refractive index of porous TiO_2 film compared to dense TiO_2 particles, derived from ellipsometry using effective medium approximation; D) changing extinction coefficient of porous TiO_2 film on ITO glass as a function of UV illumination time in the presence of glycerol.

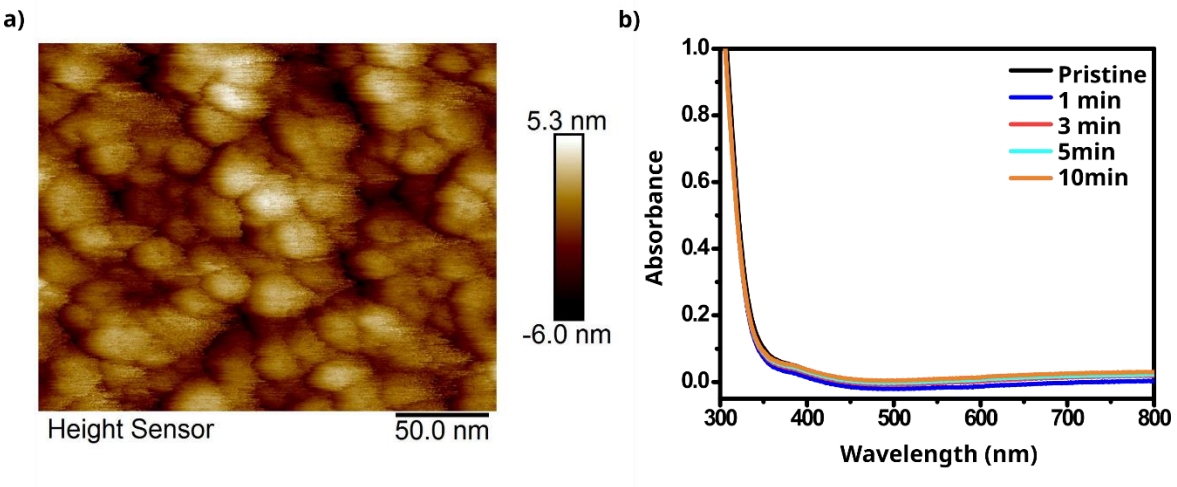

Figure 32: Properties of colloidal TiO_2 thin films: a) atomic force microscopy scan of colloidal TiO_2 film surface; b) UV-Vis measurement of changing absorbance as a function of UV illumination time for an 81 nm, 27% porous TiO_2 film on ITO glass

Anatase TiO_2 nanoparticles were synthesized through a one-step controlled hydrolysis approach modified from a procedure described by Prathapani *et al.*[235] The resulting colloidal solution was opalescent, as shown in **Figure 31**a (inset) and remained stable without coagulation for over 6 months. The bandgap was evaluated using UV-Visible spectrophotometry to generate a Tauc plot (**Figure 31**a) from the absorbance of the colloid. Fitting the curve below the band edge gives an x-intercept of 3.21 eV (386 nm), corresponding to a 10 meV shift from bulk TiO_2. Using the Brus equation to account for quantum size effects[236,241] suggests that the particle diameter is about 9.6 nm, which is consistent with the AFM images in **Figure 32**.

Crystallographic information was acquired by executing x-ray diffraction (XRD) on an aliquot of solution which was dried in an aluminum foil boat and subsequently annealed at 500°C for 30 minutes in air, yielding a faintly yellow powder. The resulting diffraction peaks in **Figure 31**a closely matched powder diffraction file No. 154603 for anatase TiO_2, and Scherrer analysis on the characteristic (101) peak reveals broadening consistent with a crystallite size of 10.3 nm, in agreement with prior particle size measurements.

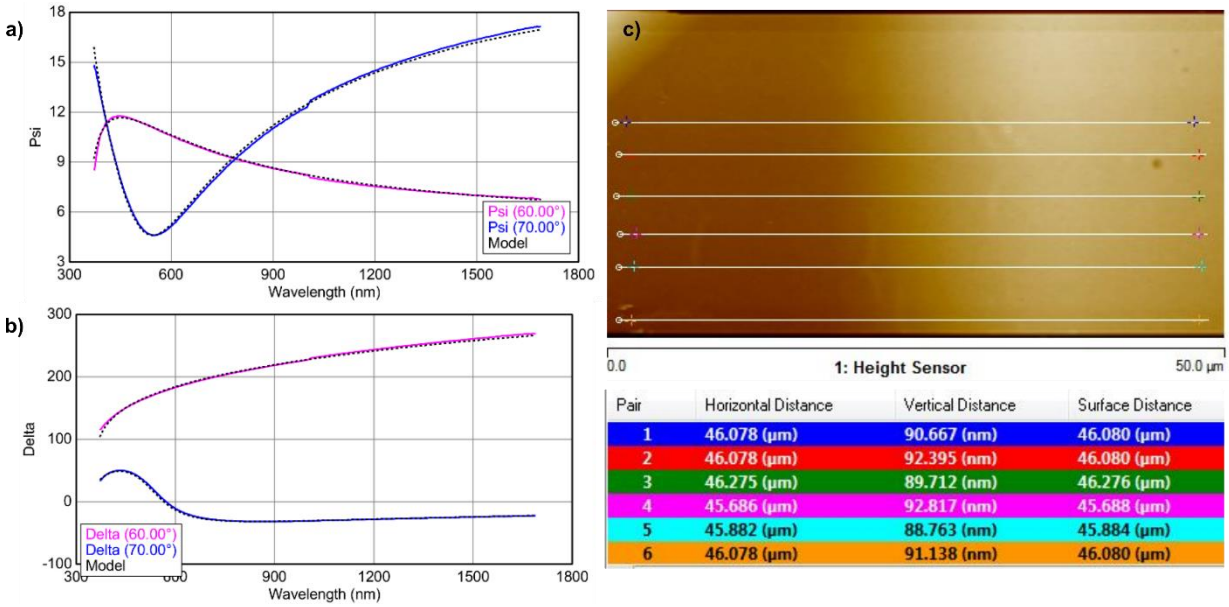

Figure 33: Ellipsometry analysis of spin coated thin films. A) Raw ellipsometry data for measured psi value and modeled result; B) Raw ellipsometry data for measured delta value and modeled result; C) AFM profile of film edge and measured thickness.

Spectroscopic ellipsometry was used to extract the porosity and complex refractive index of undoped TiO_2 NP films spin coated on glass and annealed at 500ºC for 30 minutes in air. The porous dielectric was modeled by an effective medium approximation of spherical TiO_2 inclusions interspersed with air-filled voids. Consistent with other reports of annealed TiO_2,[219,220] the dense TiO_2 component was best fit with a refractive index of 2.32 at 650 nm and negligible extinction throughout the visible spectrum (**Figure 31**c). In total, the composite film was 81 nm thick with 27% porosity. Raw ellipsometry data is included in Figure 33a-b. In order to calculate the dielectric function of such a film immersed in electrolyte, the Bruggeman effective medium approximation was applied with an MSE of 5.37 assuming 27% porosity and a dielectric constant of 1.97 for a 1:1 mixture of glycerol and water. For the composite film, we expect a refractive index of 2.07 at 650 nm, providing plenty of index contrast against typical SiO_2 substrates with n = 1.5. Upon irradiation with 365 nm UV light at 21 $\mu W/cm^2$, the measured absorbance of spin coated TiO_2 NP films increases with illumination time (**Figure 32**b). The change in extinction coefficient, k, can be calculated from the change in absorption, A, as $k = 2.303*\lambda A/(4\pi d)$,[242] where d = 81 nm as concluded from ellipsometry. The resulting curves in **Figure 31** agree with existing reports of hydrogen doped TiO_2.[224,230–232,243,244] The increase in k at longer wavelengths up to 0.078 at 700 nm is attributed to a combination of the Burstein-Moss effect, which appears the shift the band gap and absorption edge as electrons fill the bottom edge of the conduction band, and a plurality of oxygen vacancies compensating Ti^{3+}.[230,244] The real part of the refractive index can be estimated from Δk through Kramers-Kronig analysis, though the change was found to be negligible.

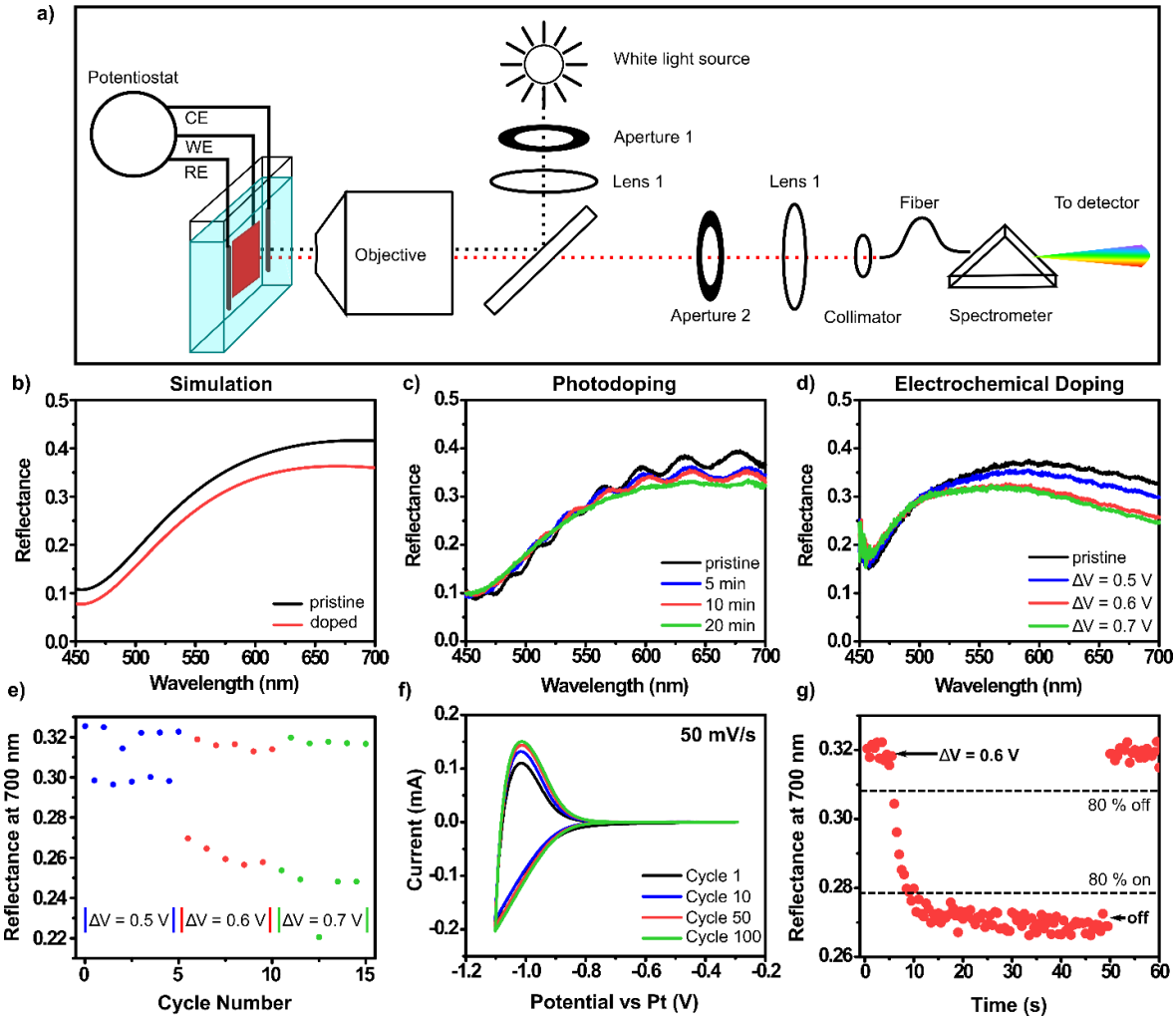

Figure 34: Demonstration of dynamic tuning in simple Fabry-Perot cavities. A) Schematic representing setup for opto-electrochemical measurements; B) FD simulation results for a pristine 135 nm TiO_2 film on Ti backplane compared to a doped film using the extinction coefficient derived from UV-Vis spectrometry; C) Experimental impact of photochemical doping by illuminating with 365 nm light in the presence of glycerol over time; D) Experimental impact of bias voltage in the presence of 0.1 M H_2SO_4 electrolyte; E) optical cyclability of dynamic tuning via electrochemical methods at different bias voltages; F) evolution of cyclic voltammagram over 100 cycles at a scan rate of 50 mV/s; G) coloration and bleaching rates for electrochemical doping with 0.6 V bias voltage.

5.4.2. Demonstration: Fabry-Perot Cavity

Having established the optical properties of anatase TiO_2 nanoparticles, their real-time spectral responses to electrochemical and photochemical doping were measured using the setup in **Figure 34**a. In the first embodiment, nanoparticles were spin coated onto a Ti metal backplane to form a simple Fabry-Perot resonator. Since the second partial reflector is formed by index mismatch at the electrolyte interface, the broadband reflection of this leaky cavity enables evaluation of performance throughout the visible spectrum. To establish expectations for visible color tuning based on a change in extinction coefficient of 0.04 at 700 nm, finite difference frequency domain (FD) simulations were executed using the experimentally determined dielectric

functions. For the proposed Fabry-Perot geometry, doping reduces reflectance throughout the visible spectrum, reaching a maximum expected decrease of 13.4%, at 700 nm (**Figure 34**b). The experimental results for a 365-nm illumination of a 140 nm film on Ti are shown in **Figure 34**c. After 10 minutes of exposure in the presence of glycerol, the experimentally determined decrease in reflection is 11% at 700 nm. Additional illumination time yields diminishing returns, reaching 11.4% decrease after 20 minutes.

When the driving force for oxygen vacancy generation is electrochemical gating, the experimentally determined change in reflection at 700 nm is 6.1% for -1 V, 19.4% for -1.1 V, and 23% for -1.2 V, close to the value theoretically predicted using the extinction coefficient measured by UV-VIS spectrophotometry. Since the open circuit voltage measured in **Figure 35** is approximately -0.5V vs Pt, potentiostatically setting the voltage to -1.1 V corresponds to a voltage bias (ΔV) of only 600 mV. Similar to the case of photochemical doping, the optical response saturates with biases more negative than -0.6 V. After 15 opto-electrochemical cycles at potentials down to -1.2 V, there is only 2.7% loss in on-state reflectance, as evidenced **Figure 34**e; however, greater biases may negatively impact energy efficiency. The outlying reflectance point in cycle 12 may be an artifact of excess hydrogen generation in the electrolyte, creating bubbles that scatter light. While the device continues to return to its original optical state even after 15 cycles, charge consumed in the water splitting reaction to create hydrogen gas detracts from overall device efficiency. This is resolved by limiting bias voltage to only 0.6 V. When electrochemically cycled to a minimum voltage of -1.1 V vs Pt at 50 mV/s, the device exhibits stable performance for over 100 voltammetric sweeps (**Figure 34**f). Coulombic efficiency may be quantified by taking the ratio of areas beneath the oxidation and reduction peaks, which is 87% for the 100^{th} cycle.

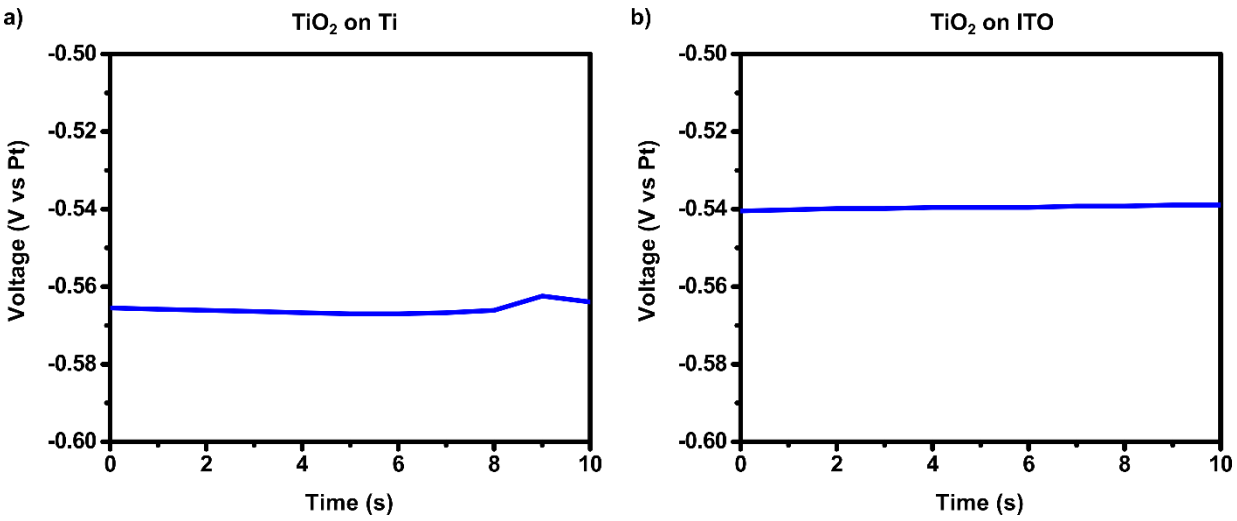

Figure 35: Open circuit voltage for a) TiO_2 on Ti and b) TiO_2 on ITO with respect to a platinum wire reference electrode.

Excellent cycling stability is attributed to the small atomic radius of the hydrogen ion, generating negligible volume expansion upon intercalation into the oxide lattice. The same property enables fast switching speeds, especially considering the short solid state diffusion lengths in the nanoparticle network. Other work has established the diffusion coefficient of protons in TiO_2 as 2.7×10^{-9} cm^2/s.[234] According to the equation, $\tau = L^2/D$, where D = 5 nm for the nanoparticle radius, the lower bound on switching speed of a diffusion limited reaction would be 92 μs. The experimental coloration and bleaching times, defined at 80% of the minimum and maximum reflectance values, respectively, are shown in **Figure 34**g. The coloration time for a bias of 0.6 V was 3.5 s, while the bleaching time was less than 0.5 s. These rates offer substantial rate enhancement over similar systems hinging on lithium ion intercalation.[34,215] The switching time could be further optimized toward the theoretical lower bound by introducing conductive additives into the nanoparticle film to reduce charge transfer resistance.

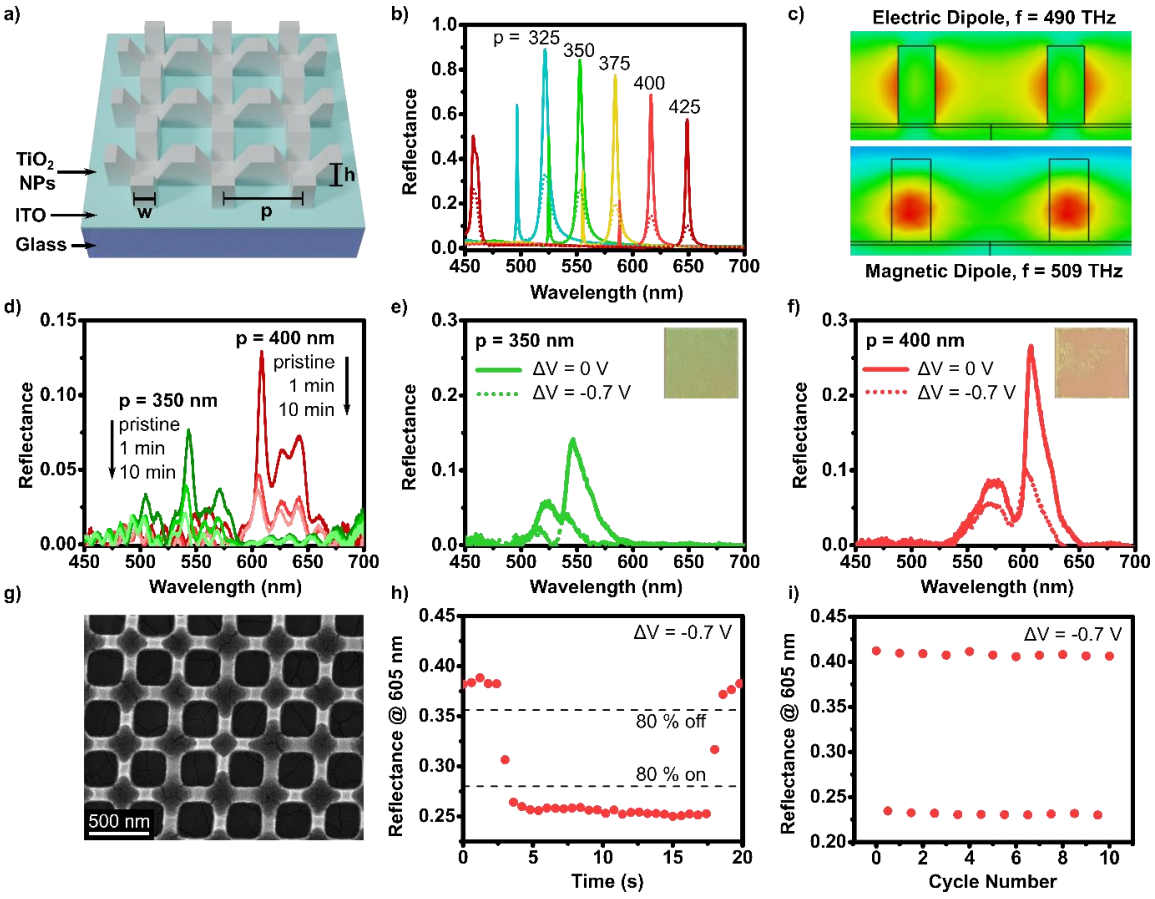

Figure 36: Performance of dynamically tunable TiO_2 metasurfaces. A) Schematic of modified fishnet metasurface; B) results of FD simulation for modified fishnet with period ranging from 325 nm to 425 nm, before and after doping; C) electrical (top) and magnetic (bottom) field distributions for resonances in simulated metasurface with 400 nm period; D) effect of 365-nm illumination of experimentally fabricated metasurfaces with 350 nm and 400 nm period in the presence of glycerol; E-F) microscope images and baselined reflectance spectra for experimentally fabricated metasurfaces before and after applying 0.7 V bias

with respect to Pt foil in 0.1 M H_2SO_4 electrolyte; G) SEM image of fabricated metasurface acquired at 5 kV; H) coloration and bleaching rates for electrochemical doping with 0.7 V bias voltage; I) optical cyclability of dynamic tuning via electrochemical doping at 0.7V bias.

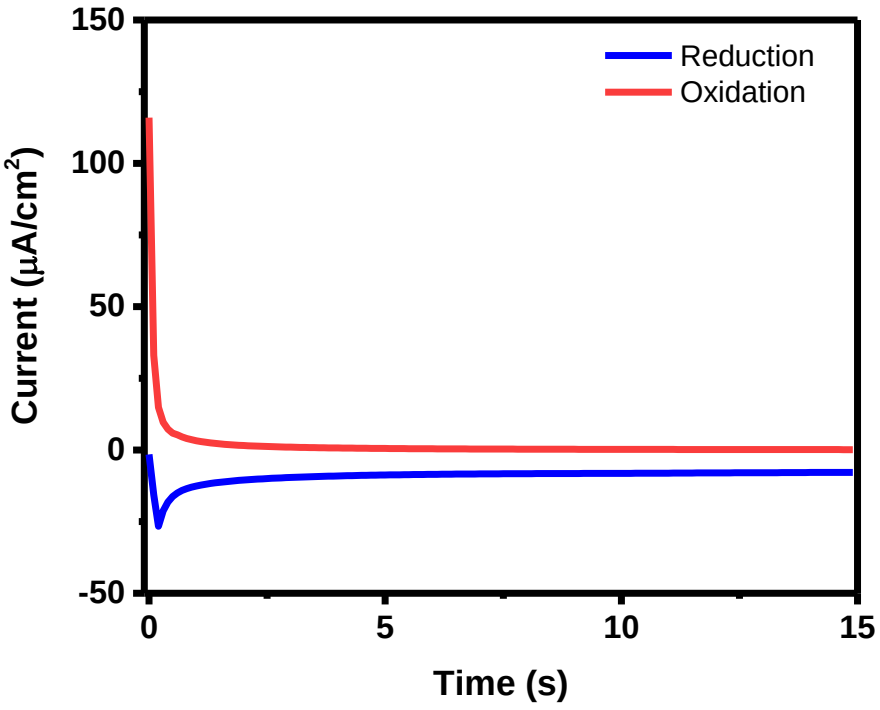

Figure 37: Current density in response to an instantaneous potential step of (blue) -1.2V vs Pt, or 700 mV bias, and (red) -0.5V vs Pt, or -0.04 V bias.

5.4.3. Demonstration: All-dielectric metasurface

Due to the strongly confined electric fields in resonant structures with high quality factors like all-dielectric metasurfaces, small changes in absorption can be leveraged for significant damping of transmission or reflection. While the Fabry-Perot cavities were a useful verification of intrinsic material properties, the lifetime of light in the cavity should be increased to achieve extreme color tuning. By structuring the nanoparticle films into a fishnet metasurface (**Figure 36**a), we expect to achieve modulation depths up to 70% in the visible spectrum. **Figure 36**b shows the simulated reflectance of modified fishnet structures comprising TiO_2 NPs with 100 nm bar width, 200 nm bar height, and periods ranging from 350 – 400 nm on a 10 nm layer of ITO for electrical contact. For each period, simulated field distributions in **Figure 36**c reveal that the larger peak at longer wavelengths is associated with an electric dipole, while the extremely narrow peak comes from a magnetic dipole. For the experimentally fabricated metasurfaces in **Figure 36**d, the resonance red shifts with increasing period due to reduced coupling between parallel resonators; however, the measured intensities are lower than predicted due to nonuniformities in bar height throughout the spin coated structure. For a 400 nm

period, exposure to 365 nm illumination in the presence of glycerol results in 65% damping after 1 minute, increasing to 72% damping after 10 minutes. For a metasurface with 350 nm period, the resonance is 53% damped after 1 minute, and 74% damped after 10 minutes. It is important to note that the majority of damping action occurs within the first minute of illumination. The damping may exceed expectations due electromagnetic field enhancements by higher order modes at ultraviolet frequencies, improving absorption and photochemical activity[224]. The results of real-time opto-electrochemical experiments are included in **Figure 36**e-f for the fabricated metasurfaces in 0.1 M H_2SO_4. A 700 mV bias was chosen to account for increased overpotential caused by the high resistivity of a 10 nm ITO current collector. In the top right corner of each plot, an optical micrograph is included to show the perceived color of the 100-μm square array before doping. After electrochemical doping, the modulation depths for metasurfaces with 350 nm and 400 nm periods are measured at 72%, and 64%, respectively, exceeding computationally determined expectations. **Figure 36**g shows an SEM image of an actual metasurface prepared by colloidal fabrication with 400 nm period. This device demonstrates nearly perfect cyclability, retaining 99% of the original reflectance in the off state after 10 cycles (**Figure 36**h), with a coloration and bleaching time of approximately 1 s (**Figure 36**i). Despite higher resistance in the thin ITO current collector, improved speed over the Fabry-Perot configuration may be the result of enhanced ion mobility at the electrolyte interface of the structured electrode. While there is still room for optimization, electrochemical switching via hydrogen doping is an ultralow power process suitable for eco-friendly reflective displays. Analysis of the current response to a sudden change in bias (**Figure 37**) reveals a peak current of 26.6 $\mu A/cm^2$ for reduction, and 11.6 $\mu A/cm^2$ for oxidation. Since energy is stored during the reduction process and spontaneously released during oxidation, as with discharging a battery, the peak input power is 26.6 $\mu A/cm^2$ x 0.7 V, or only 18.6 $\mu W/cm^2$.

5.5. Conclusions

Having achieved modulation depths from 64-74% across the visible spectrum, both electrochemical and photochemical doping are powerful mechanisms for on-demand switching of all-dielectric TiO_2 metasurfaces in practical device configurations. The fabrication method avoids lengthy vapor-phase deposition processes without sacrificing cycle life and can be switched on the order of 1 s. With an ultralow power density of 1.1 $\mu W/cm^2$ for color modulation, this system is a compelling platform for next-generation dynamic reflective display technologies.

Chapter 6: Conclusion

6.1. Summary

Energy storage is just one element in a comprehensive approach to the mitigation of greenhouse gas emissions. In this dissertation, I investigated phenomena underlying engineered devices which change the way we generate, distribute, and use energy, all connected by systematic analysis of mass transport in electrochemical

cells.

First, I probed the weak points of promising alternative-ion battery chemistries that utilize elements with higher abundance than Li in the Earth's crust. For magnesium ion batteries, progress was inhibited by poor understanding of transport and plating from multivalent ion electrolytes. In Chapter 2, I used the experimentally determined diffusion coefficient for Mg^{2+} in 0.1M $Mg(TFSI)_2$ in classical electrochemical expressions for the limiting current density and Sand's time to map the morphological space of Mg metal electrodeposited as a function of current density. I brought attention to the shifting balance between kinetic and mass transport control which resulted in nonequilibrium three-dimensional growth after extended plating durations. In Chapter 3, I turned my attention to low-cost sodium ion batteries, which are limited by the availability of anode materials with high energy density and sufficient durability to withstand repeated incorporation of sodium ions, which have Shannon ionic radii 34% larger than Li^+.[245] I evaluated the possibility of directly upcycling Pb alloys from LABs as anode materials for sodium ion batteries, and discovered a way to tune the power and cycle life by applying heat treatments to redistribute the initial phase distribution of Pb and Sb. I used GITT to show that solid state diffusion was enhanced along phase boundaries in aged, recycled alloys. Further, I found that finer phase distributions self-assembled into finer ligaments in the presence of diglyme electrolytes, leading to improved rate capability. In this way, I showed that the balance between power and cycle life could be optimized using different heat treatments to redistribute the original alloy phases.

Having applied principles of mass transport to improve power delivery of batteries, I then leveraged similar design strategies to reduce power consumption of tunable photonic devices. In Chapter 4, I revealed that Li^+ intercalation in anatase TiO_2 generates a large change in refractive index of 0.65 at 650 nm with low loss at blue wavelengths; however, switching speeds on the order of 50 seconds for 100-nm thick films impede practical application. Unable to change the diffusion coefficient for Li^+ in sputtered TiO_2, I designed a gap plasmon metasurface to overlap strong electric fields within a 20-nm thin film of anatase TiO_2. This reduced both the diffusion length and reaction volume to achieve switching in only 7 seconds at a peak power density of 34 $\mu W/cm^2$. Compared to CRT displays which consume over 250 mW/cm^2,[40] this work establishes electrochemical actuation as a promising platform for reflective display applications.

While the lithiation of TiO_2 introduced a compelling method for broadband tunability of visible metamaterials, the switching rate was limited by diffusion of lithium through solid dielectric films. In Chapter 5, I used TiO_2 nanoparticles to fabricate all-dielectric metasurfaces which were electrochemically tuned to modulation depths up to 72% in water-based electrolytes with sub-volt biases. By swapping lithium for the smaller protons and using nanoparticles with approximately 10 nm diameter, switching speed was further reduced to ~1 s, with ultralow power consumption of only 1.1 $\mu W/cm^2$. Further, the nanoparticles respond to ultraviolet illumination, enabling optical addressing of large-format devices without the need for complex circuitry.

6.2. Outlook for next-generation energy storage

Despite the environmental and economic advantages of Na and Mg as earth-abundant metals for next-generation battery systems, both technologies face substantial barriers to widespread commercialization. For Mg the major barriers are related to the increased electronegativity and sluggish transport of the divalent Mg ion. This complicates the development of electrolytes and high-voltage intercalation compounds that allow the fast and reversible migration of Mg^{2+}.[246,247] My work further destabilizes the future of Mg batteries by directly connecting sluggish transport to three-dimensional growth and internal shorting events, dispelling rumors of flat growth and intrinsic safety.[44,45] For sodium, the major barriers are related to energy density and cycle life.[248] I have demonstrated the opportunity to further reduce costs by using low-purity, low-cost anode materials with tunable performance, but long-term cyclability remains a challenge. In other work from the Pint group, Dr. Adam Cohn circumvented the drawbacks of high-expansion anode materials altogether through in-situ plating of sodium metal from the cathode directly onto the current collector, further reducing costs and increasing energy density.[249] Regardless of which emerging energy storage chemistries become commercially viable, the increasing dominance of secondary batteries comes with increasing urgency to innovate in the field of battery recycling. Of the existing methods, direct recycling methods consume 78% and 86% less energy than hydrometallurgy or pyrometallurgy, respectively; however, the process is complicated by the presence of binders, conductive additives, and reactive liquid electrolytes found in commercial batteries.[250] To achieve a truly sustainable life cycle for secondary batteries, they should be designed for recyclability from the ground up.

6.3. Outlook for low-power photonics

Electrochemical methods for modulation of metamaterials are powerful because they can enable coordinate transformations of the resulting phase profile and/or generate massive permittivity changes in constituent materials through a combination of electrical gating and phase change mechanisms. To-date, they have been applied using electroplating[251,252], electrochromic polymers[253–257], and intercalation in metal oxides[258–262], but most demonstrations have resulted in insufficient modulation depth, poor cyclability, or slow switching speeds. The ideal material for electrochemical modulation might undergo a fast, highly reversible phase change from an insulating to metallic state with an epsilon near zero (ENZ) point in the range of interest. With these guidelines in mind, there is still a vast design space for exploration of optical transformations in other redox-active materials.

6.4. Future directions

In the work chronicled here, I developed an expertise in electrochemical energy storage which I then applied to the dynamic modulation of optical metamaterials. In the future, I think there are exciting opportunities to address the multi-scale challenge of sustainable energy storage by applying photonics to the understanding and enhancement of electrochemical systems; for example, integrating optical sensors with batteries to measure materials properties (e.g. volume change) or cell-level properties (e.g. temperature). Further, since

electrochemical cells are multiscale systems influenced by elastic, thermodynamic, diffusional, and electrical processes, there may be a path toward a new class of metamaterials called “electrochemical metamaterials” to separate and guide ionic species as in fuel cells, batteries, electrocatalysis, electroplating, etc. As we continue to push the boundaries of what is possible with electrochemical methods, there is plenty of room for innovation at the intersection of electrochemistry and photonics.

References

1. U.S. Energy Information Administration. Electricity in the U.S. https://www.eia.gov/energyexplained/electricity/electricity-in-the-us.php.
2. Turner, J. A. A realizable renewable energy future. *Science* vol. 285 687–689 (1999).
3. Yang, Y., Bremner, S., Menictas, C. & Kay, M. Battery energy storage system size determination in renewable energy systems: A review. *Renewable and Sustainable Energy Reviews* vol. 91 109–125 (2018).
4. Barton, J. P. & Infield, D. G. Energy storage and its use with intermittent renewable energy. **19**, 441–448 (2004).
5. Ritchie, H. & Roser, M. CO_2 and Greenhouse Gas Emissions. *Our World Data* (2020).
6. Bard, A. J. & Faulkner, L. R. *Electrochemical methods : fundamentals and applications*. (Wiley, 2001).
7. Kobayashi, T., Yoneyama, H. & Tamura, H. Electrochemical reactions concerned with electrochromism of polyaniline film-coated electrodes. *J. Electroanal. Chem.* **177**, 281–291 (1984).
8. Mandal, J. *et al.* Li 4 Ti 5 O 12 : A Visible-to-Infrared Broadband Electrochromic Material for Optical and Thermal Management. *Adv. Funct. Mater.* **28**, 1802180 (2018).
9. Fuller, T. F. & Harb, J. N. *Electrochemical Engineering*. (Wiley, 2018).
10. Olivetti, E. A., Ceder, G., Gaustad, G. G. & Fu, X. Lithium-Ion Battery Supply Chain Considerations: Analysis of Potential Bottlenecks in Critical Metals. *Joule* **1**, 229–243 (2017).
11. Recycle spent batteries. *Nat. Energy* **4**, 253–253 (2019).
12. U.S. Geological Survey. *U.S. Geological Survey 2019*. *Mineral commodity summaries* https://www.usgs.gov/centers/nmic/mineral-commodity-summaries (2019).
13. Saha, P. *et al.* Rechargeable magnesium battery: Current status and key challenges for the future. *Prog. Mater. Sci.* **66**, 1–86 (2014).
14. Villalonga, B. *et al.* Establishing the quantum supremacy frontier with a 281 Pflop/s simulation. *Quantum Sci. Technol.* **5**, 034003 (2020).
15. Zhai, Y. *et al.* Scalable-manufactured randomized glass-polymer hybrid metamaterial for daytime radiative cooling. *Science (80-.).* **355**, 1062–1066 (2017).
16. Kuznetsov, A. I., Miroshnichenko, A. E., Brongersma, M. L., Kivshar, Y. S. & Luk’yanchuk, B. Optically resonant dielectric nanostructures. *Science (80-.).* **354**, (2016).
17. Wang, W. *et al.* Self-adaptive radiative cooling and solar heating based on a compound metasurface. *J. Mater. Chem. C* **8**, 3192–3199 (2020).
18. Sentker, K. *et al.* Self-Assembly of liquid crystals in nanoporous solids for adaptive photonic metamaterials. *Nanoscale* **11**, 23304–23317 (2019).
19. Ono, M., Chen, K., Li, W. & Fan, S. Self-adaptive radiative cooling based on phase change materials. *Opt. Express* **26**, A777 (2018).
20. Ma, Q. *et al.* Smart metasurface with self-adaptively reprogrammable functions. *Light Sci. Appl.* **8**, 2047–7538 (2019).
21. Li, L. *et al.* Intelligent metasurface imager and recognizer. *Light Sci. Appl.* **8**, 2047–7538 (2019).
22. Hail, C. U., Michel, A. U., Poulikakos, D. & Eghlidi, H. Optical Metasurfaces: Evolving from Passive to Adaptive. *Adv. Opt. Mater.* **7**, 1801786 (2019).
23. Komar, A. *et al.* Dynamic Beam Switching by Liquid Crystal Tunable Dielectric Metasurfaces. *ACS Photonics* **5**, 1742–1748 (2018).
24. Komar, A. *et al.* Electrically tunable all-dielectric optical metasurfaces based on liquid crystals. *Appl. Phys. Lett.* **110**, 071109 (2017).
25. She, A., Zhang, S., Shian, S., Clarke, D. R. & Capasso, F. Adaptive metalenses with simultaneous electrical control of focal length, astigmatism, and shift. *Sci. Adv.* **4**, (2018).

26. Roy, T. *et al.* Dynamic metasurface lens based on MEMS technology. *APL Photonics* **3**, 021302 (2018).
27. Arbabi, E. *et al.* MEMS-tunable dielectric metasurface lens. *Nat. Commun.* **9**, 1–9 (2018).
28. Sherrott, M. C. *et al.* Experimental Demonstration of >230° Phase Modulation in Gate-Tunable Graphene-Gold Reconfigurable Mid-Infrared Metasurfaces. *Nano Lett.* **17**, 3027–3034 (2017).
29. Howes, A., Wang, W., Kravchenko, I. & Valentine, J. Dynamic transmission control based on all-dielectric Huygens metasurfaces. *Optica* **5**, 787 (2018).
30. Park, J., Kang, J. H., Liu, X. & Brongersma, M. L. Electrically Tunable Epsilon-Near-Zero (ENZ) Metafilm Absorbers. *Sci. Rep.* **5**, 1–9 (2015).
31. Petronijevic, E. & Sibilia, C. All-optical tuning of EIT-like dielectric metasurfaces by means of chalcogenide phase change materials. *Opt. Express* **24**, 30411 (2016).
32. Kana Kana, J. B., Vignaud, G., Gibaud, A. & Maaza, M. Thermally driven sign switch of static dielectric constant of VO2 thin film. *Opt. Mater. (Amst).* **54**, 165–169 (2016).
33. Ding, F., Yang, Y. & Bozhevolnyi, S. I. Dynamic Metasurfaces Using Phase-Change Chalcogenides. *Adv. Opt. Mater.* **7**, 1801709 (2019).
34. Li, Y., van de Groep, J., Talin, A. A. & Brongersma, M. L. Dynamic Tuning of Gap Plasmon Resonances Using a Solid-State Electrochromic Device. *Nano Lett.* **19**, 7988–7995 (2019).
35. Zanotto, S. *et al.* Metasurface Reconfiguration through Lithium-Ion Intercalation in a Transition Metal Oxide. *Adv. Opt. Mater.* **5**, 1600732 (2017).
36. Wang, G., Chen, X., Liu, S., Wong, C. & Chu, S. Mechanical Chameleon through Dynamic Real-Time Plasmonic Tuning. *ACS Nano* **10**, 1788–1794 (2016).
37. Xia, X. *et al.* Electrochemically reconfigurable architected materials. *Nature* **573**, 205–213 (2019).
38. Shcherbakov, M. R. *et al.* Ultrafast all-optical tuning of direct-gap semiconductor metasurfaces. *Nat. Commun. 2017 81* **8**, 1–6 (2017).
39. Peng, J. *et al.* Scalable electrochromic nanopixels using plasmonics. *Sci. Adv.* **5**, eaaw2205 (2019).
40. Xiong, K., Tordera, D., Jonsson, M. P. & Dahlin, A. B. Active control of plasmonic colors: Emerging display technologies. *Reports on Progress in Physics* vol. 82 024501 (2019).
41. Kim, I. *et al.* Outfitting Next Generation Displays with Optical Metasurfaces. *ACS Photonics* **5**, 3876–3895 (2018).
42. Lin, D., Liu, Y. & Cui, Y. Reviving the lithium metal anode for high-energy batteries. *Nat. Nanotechnol.* **12**, 194–206 (2017).
43. Jäckle, M. & Groß, A. Microscopic Properties of Lithium, Sodium, and Magnesium Battery Anode Materials Related to Possible Dendrite Growth. *J. Chem. Phys.* **141**, 174710 (2014).
44. Ling, C., Banerjee, D. & Matsui, M. Study of the electrochemical deposition of Mg in the atomic level: Why it prefers the non-dendritic morphology. *Electrochim. Acta* **76**, 270–274 (2012).
45. Matsui, M. Study on electrochemically deposited Mg metal. *J. Power Sources* **196**, 7048–7055 (2011).
46. Gregory, T. D., Hoffman, R. J. & Winterton, R. C. Nonaqueous Electrochemistry of Magnesium. *J. Electrochem. Soc.* **137**, 775 (1990).
47. Ding, M. S., Diemant, T., Behm, R. J., Passerini, S. & Giffin, G. A. Dendrite Growth in Mg Metal Cells Containing Mg(TFSI) 2 /Glyme Electrolytes. *J. Electrochem. Soc.* **165**, A1983–A1990 (2018).
48. Davidson, R. *et al.* Formation of magnesium dendrites during electrodeposition. *ACS Energy Lett.* **4**, 375–376 (2019).
49. Davidson, R. *et al.* Mapping mechanisms and growth regimes of magnesium electrodeposition at high current densities. *Mater. Horizons* (2020) doi:10.1039/C9MH01367A.
50. Ha, S.-Y. *et al.* Magnesium(II) Bis(trifluoromethane sulfonyl) Imide-Based Electrolytes with Wide Electrochemical Windows for Rechargeable Magnesium Batteries. *ACS Appl. Mater. Interfaces* **6**, 4063–4073 (2014).
51. Tutusaus, O., Mohtadi, R., Singh, N., Arthur, T. S. & Mizuno, F. Study of Electrochemical Phenomena Observed at the Mg Metal/Electrolyte Interface. *ACS Energy Lett.* **2**, 224–229 (2017).
52. Senoh, H. *et al.* Charge-Discharge Performance of Rechargeable Organic-Magnesium Batteries Using Glyme-Based Electrolytes. *ECS Trans.* **29**, 33–39 (2015).
53. Kang, S.-J. *et al.* Electrolyte Additive Enabling Conditioning-Free Electrolytes for Magnesium Batteries. *ACS Appl. Mater. Interfaces* **11**, 517–524 (2019).
54. Connell, J. G. *et al.* Tuning the Reversibility of Mg Anodes via Controlled Surface Passivation by H 2 O/Cl − in Organic Electrolytes. *Chem. Mater* **28**, 8268–8277 (2016).
55. Yu, Y. *et al.* Instability at the Electrode/Electrolyte Interface Induced by Hard Cation Chelation and Nucleophilic Attack. *Chem. Mater.* **29**, 8504–8512 (2017).

56. Shterenberg, I. *et al.* Evaluation of (CF3SO2)2N− (TFSI) Based Electrolyte Solutions for Mg Batteries. *J. Electrochem. Soc.* **162**, A7118–A7128 (2015).
57. Ma, Z., Kar, M., Xiao, C., Forsyth, M. & Macfarlane, D. R. Electrochemical Cycling of Mg in Mg[TFSI] 2 /Tetraglyme Electrolytes. *Electrochem. commun.* **78**, 29–32 (2017).
58. Jäckle, M., Katharina Helmbrecht, A., Malte Smits, A., Daniel Stottmeister ab, A. & Groß, A. Self-diffusion barriers: possible descriptors for dendrite growth in batteries? *Energy Environ. Sci* **11**, 3400 (2018).
59. Bai, P., Li, J., Brushett, F. R. & Bazant, M. Z. Transition of lithium growth mechanisms in liquid electrolytes. *Energy Environ. Sci.* **9**, 3221–3229 (2016).
60. Tikekar, M. D., Choudhury, S., Tu, Z. & Archer, L. A. Design principles for electrolytes and interfaces for stable lithium-metal batteries. *Nat. Energy* **1**, 16114 (2016).
61. Lu, Y. *et al.* Stable Cycling of Lithium Metal Batteries Using High Transference Number Electrolytes. *Adv. Energy Mater.* **5**, 1402073 (2015).
62. Lu, Y., Tu, Z., Shu, J. & Archer, L. A. Stable lithium electrodeposition in salt-reinforced electrolytes. *J. Power Sources* **279**, 413–418 (2015).
63. Chen, K.-H. *et al.* Dead lithium: mass transport effects on voltage, capacity, and failure of lithium metal anodes. *J. Mater. Chem. A* **5**, 11671–11681 (2017).
64. Wood, K. N. *et al.* Dendrites and pits: Untangling the complex behavior of lithium metal anodes through operando video microscopy. *ACS Cent. Sci.* **2**, 790–801 (2016).
65. Fleury, V., Chazalviel, J. N. & Rosso, M. Theory and experimental evidence of electroconvection around electrochemical deposits. *Phys. Rev. Lett.* **68**, 2492–2495 (1992).
66. Fleury, V., Chazalviel, J.-N. & Rosso, M. Coupling of drift, diffusion, and electroconvection, in the vicinity of growing electrodeposits. *Phys. Rev. E* **48**, (1993).
67. Chazalviel, J.-N. Electrochemical aspects of the generation of ramified metallic electrodeposits. *Phys. Rev. A* **42**, 7355–7367 (1990).
68. Bard, A. J. & Faulkner, L. R. *Electrochemical Methods: Fundamentals and Applications*. (Wiley, 2001).
69. Rosso, M., Gobron, T., Brissot, C., Chazalviel, J. N. & Lascaud, S. Onset of dendritic growth in lithium/polymer cells. in *Journal of Power Sources* vols 97–98 804–806 (2001).
70. Brissot, C., Rosso, M., Chazalviel, J.-N., Baudry, P. & Lascaud, S. In situ study of dendritic growth in lithium/PEO-salt/lithium cells. *Electrochim. Acta* **43**, 1569–1574 (1998).
71. Brissot, C., Rosso, M., Chazalviel, J.-N., Lascaud, S. & Francè´, F. Dendritic growth mechanisms in lithium polymer cells. *J. Power Sources* **81**, 925–929 (1999).
72. Ren, X. *et al.* High-Concentration Ether Electrolytes for Stable High-Voltage Lithium Metal Batteries. *ACS Energy Lett.* **4**, 896–902 (2019).
73. Chen, S. *et al.* High-Voltage Lithium-Metal Batteries Enabled by Localized High-Concentration Electrolytes. *Adv. Mater.* **30**, 1706102 (2018).
74. Li, Q., Tan, S., Li, L., Lu, Y. & He, Y. Understanding the molecular mechanism of pulse current charging for stable lithium-metal batteries. *Sci. Adv.* **3**, 1701246 (2017).
75. Mayers, M. Z., Kaminski, J. W. & Miller, T. F. Suppression of Dendrite Formation via Pulse Charging in Rechargeable Lithium Metal Batteries. *J. Phys. Chem. C* **116**, 26214–26221 (2012).
76. Ryou, M.-H. *et al.* Excellent Cycle Life of Lithium-Metal Anodes in Lithium-Ion Batteries with Mussel-Inspired Polydopamine-Coated Separators. *Adv. Energy Mater.* **2**, 645–650 (2012).
77. Ding, F. *et al.* Dendrite-Free Lithium Deposition via Self-Healing Electrostatic Shield Mechanism. *J. Am. Chem. Soc.* **135**, 4450–4456 (2013).
78. Chi, S.-S., Qi, X.-G., Hu, Y.-S. & Fan, L.-Z. 3D Flexible Carbon Felt Host for Highly Stable Sodium Metal Anodes. *Adv. Energy Mater.* **8**, 1702764 (2018).
79. Sa, N. *et al.* Is alpha-V 2 O 5 a Cathode Material for Mg Insertion Batteries? *J. Power Sources* **323**, 44–50 (2016).
80. Sa, N. *et al.* Concentration Dependent Electrochemical Properties and Structural Analysis of a Simple Magnesium Electrolyte: Magnesium bis(trifluoromethane sulfonyl)imide in Diglyme. *R. Soc. Chem.* **6**, 113663–113670 (2016).
81. Rajput, N. N., Qu, X., Sa, N., Burrell, A. K. & Persson, K. A. The Coupling between Stability and Ion Pair Formation in Magnesium Electrolytes from First-Principles Quantum Mechanics and Classical Molecular Dynamics. *J. Am. Chem. Soc.* **137**, 3411–3420 (2015).
82. Yamada, Y., Iriyama, Y., Abe, T. & Ogumi, Z. Kinetics of Lithium Ion Transfer at the Interface between Graphite and Liquid Electrolytes: Effects of Solvent and Surface Film. *Langmuir* **25**, 12766–12770

(2009).
83. Lu, Y., Tu, Z. & Archer, L. A. Stable lithium electrodeposition in liquid and nanoporous solid electrolytes. *Nat. Mater.* **13**, 961–969 (2014).
84. Cvetković, V. *et al.* Magnesium–Gold Alloy Formation by Underpotential Deposition of Magnesium onto Gold from Nitrate Melts. *Metals (Basel).* **7**, 95 (2017).
85. Guo, L. & Searson, P. C. On the influence of the nucleation overpotential on island growth in electrodeposition. *Electrochim. Acta* **55**, 4086–4091 (2010).
86. Branco P., D., Mostany, J., Borrás, C. & Scharifker, B. R. The current transient for nucleation and diffusion-controlled growth of spherical caps. *J. Solid State Electrochem.* **13**, 565–571 (2009).
87. Gunawardena, G., Hills, G., Montenegro, I. & Scharifker, B. Electrochemical nucleation. Part I. General considerations. *J. Electroanal. Chem.* **138**, 225–239 (1982).
88. Pei, A., Zheng, G., Shi, F., Li, Y. & Cui, Y. Nanoscale Nucleation and Growth of Electrodeposited Lithium Metal. *Nano Lett.* **17**, 1132–1139 (2017).
89. Rajput, N. N., Seguin, T. J., Wood, B. M., Qu, X. & Persson, K. A. Elucidating Solvation Structures for Rational Design of Multivalent Electrolytes—A Review. *Top. Curr. Chem.* **376**, 79–124 (2018).
90. Hebié, S. *et al.* Electrolyte Based on Easily Synthesized, Low Cost Triphenolate− Borohydride Salt for High Performance Mg(TFSI) 2-Glyme Rechargeable Magnesium Batteries. *ACS Appl. Mater. Interfaces* **9**, 28377–28385 (2017).
91. Merrill, L. C. & Schaefer, J. L. The Influence of Interfacial Chemistry on Magnesium Electrodeposition in Non-nucleophilic Electrolytes Using Sulfone-Ether Mixtures. *Front. Chem.* **7**, 194 (2019).
92. Bazant, M. Z. Regulation of ramified electrochemical growth by a diffusive wave. *Phys. Rev. E* **52**, 1903–1914 (1995).
93. Hu, J. Z. *et al.* 25Mg NMR and computational modeling studies of the solvation structures and molecular dynamics in magnesium based liquid electrolytes. *Nano Energy* **46**, 436–446 (2018).
94. Jana, A., Ely, D. R. & García, R. E. Dendrite-separator interactions in lithium-based batteries. *J. Power Sources* **275**, 912–921 (2015).
95. Singh, N. *et al.* Achieving High Cycling Rates via In Situ Generation of Active Nanocomposite Metal Anodes. *ACS Appl. Energy Mater.* **1**, 4651–4661 (2018).
96. Zhao-Karger, Z. *et al.* Toward Highly Reversible Magnesium-Sulfur Batteries with Efficient and Practical Mg[B(hfip)4]2 Electrolyte. *ACS Energy Lett.* **3**, 2005–2013 (2018).
97. Ling, C., Banerjee, D. & Matsui, M. Study of the electrochemical deposition of Mg in the atomic level: Why it prefers the non-dendritic morphology. *Electrochim. Acta* **76**, 270–274 (2012).
98. Cohn, A. P., Muralidharan, N., Carter, R., Share, K. & Pint, C. L. Anode-Free Sodium Battery through in Situ Plating of Sodium Metal. *Nano Lett.* **17**, 1296–1301 (2017).
99. Cohn, A. P. *et al.* Rethinking Sodium-Ion Anodes as Nucleation Layers for Anode-Free Batteries. *J. Mater. Chem. A* **6**, 23875–23884 (2018).
100. Yan, K. *et al.* Selective Deposition and Stable Encapsulation of Lithium Through Heterogeneous Seeded Growth. *Nat. Energy* **1**, 16010 (2016).
101. Deivanayagam, R., Ingram, B. J. & Shahbazian-Yassar, R. Progress in development of electrolytes for magnesium batteries. *Energy Storage Materials* vol. 21 136–153 (2019).
102. Payne, D. J., Ballantyne, A. D., Hallett, J. P., Riley, D. J. & Shah, N. Lead acid battery recycling for the twenty-first century. *R. Soc. Open Sci.* **5**, (2016).
103. Ellis, T. W. & Mirza, A. H. The refining of secondary lead for use in advanced lead-acid batteries. *J. Power Sources* **195**, 4525–4529 (2010).
104. Freedonia Focus. *Lead: United States*. www.freedoniafocusreports.com (2018).
105. Freedonia Focus. *Batteries: United States*. www.freedoniafocusreports.com (2018).
106. A Behind the Scenes Take on Lithium-ion Battery Prices | BloombergNEF. https://about.bnef.com/blog/behind-scenes-take-lithium-ion-battery-prices/.
107. Liu, W., Chen, L. & Tian, J. Uncovering the Evolution of Lead In-Use Stocks in Lead-Acid Batteries and the Impact on Future Lead Metabolism in China. *Environ. Sci. Technol.* **50**, 5412–5419 (2016).
108. Baggetto, L. *et al.* Characterization of sodium ion electrochemical reaction with tin anodes: Experiment and theory. *J. Power Sources* **234**, 48–59 (2013).
109. Zhang, B. *et al.* Microsized Sn as Advanced Anodes in Glyme-Based Electrolyte for Na-Ion Batteries. *Adv. Mater.* **28**, 9824–9830 (2016).
110. Li, Z., Ding, J. & Mitlin, D. Tin and Tin Compounds for Sodium Ion Battery Anodes: Phase Transformations and Performance. *Acc. Chem. Res.* **48**, 1657–1665 (2015).

111. Liu, W. *et al.* Gassing in Sn-anode sodium-ion batteries and its remedy by metallurgically pre-alloying Na. *ACS Appl. Mater. Interfaces* **11**, 23207–23212 (2019).
112. Ying, H. & Han, W.-Q. Metallic Sn-Based Anode Materials: Application in High-Performance Lithium-Ion and Sodium-Ion Batteries. *Adv. Sci.* **4**, 1700298 (2017).
113. Lin, Y.-M. *et al.* Sn−Cu Nanocomposite Anodes for Rechargeable Sodium-Ion Batteries. *ACS Appl. Mater. Interfaces* **5**, 8273–8277 (2013).
114. Ellis, L. D., Wilkes, B. N., Hatchard, T. D. & Obrovac, M. N. In Situ XRD Study of Silicon, Lead and Bismuth Negative Electrodes in Nonaqueous Sodium Cells. *J. Electrochem. Soc.* **161**, 416–421 (2014).
115. Wang, C., Wang, L., Li, F., Cheng, F. & Chen, J. Bulk Bismuth as a High-Capacity and Ultralong Cycle-Life Anode for Sodium-Ion Batteries by Coupling with Glyme-Based Electrolytes. *Adv. Mater.* **29**, 1702212 (2017).
116. Bridel, J.-S. *et al.* Decomposition of ethylene carbonate on electrodeposited metal thin film anode. *J. Power Sources* **195**, 2036–2043 (2010).
117. Sottmann, J. *et al.* How Crystallite Size Controls the Reaction Path in Nonaqueous Metal Ion Batteries: The Example of Sodium Bismuth Alloying. *Chem. Mater.* **28**, 2750–2756 (2016).
118. Yang, F. *et al.* Bismuth Nanoparticles Embedded in Carbon Spheres as Anode Materials for Sodium/Lithium-Ion Batteries. *Chem. - A Eur. J.* **22**, 2333–2338 (2016).
119. Hou, H. *et al.* Antimony nanoparticles anchored on interconnected carbon nanofibers networks as advanced anode material for sodium-ion batteries. *J. Power Sources* **284**, 227–235 (2015).
120. Li, Z. *et al.* Coupling In Situ TEM and Ex Situ Analysis to Understand Heterogeneous Sodiation of Antimony. *Nano Lett.* **15**, 6339–6348 (2015).
121. He, M., Kravchyk, K., Walter, M. & Kovalenko, M. V. Monodisperse Antimony Nanocrystals for High-Rate Li-ion and Na-ion Battery Anodes: Nano versus Bulk. *Nano Lett.* **14**, 1255–1262 (2014).
122. Qian, J. *et al.* High capacity Na-storage and superior cyclability of nanocomposite Sb/C anode for Na-ion batteries. *Chem. Commun.* **48**, 7070 (2012).
123. Darwiche, A. *et al.* Better Cycling Performances of Bulk Sb in Na-Ion Batteries Compared to Li-Ion Systems: An Unexpected Electrochemical Mechanism. *J. Am. Chem. Soc.* **134**, 20805–20811 (2012).
124. Darwiche, A., Dugas, R., Fraisse, B. & Monconduit, L. Reinstating lead for high-loaded efficient negative electrode for rechargeable sodium-ion battery. *J. Power Sources* **304**, 1–8 (2016).
125. Komaba, S. *et al.* Redox reaction of Sn-polyacrylate electrodes in aprotic Na cell. *Electrochem. commun.* **21**, 65–68 (2012).
126. Kim, C. *et al.* A high rate and long-cycle-life anode based on micrometer-sized Pb powder for sodium-ion batteries. *J. Alloys Compd.* **886**, 161240 (2021).
127. Pandit, B., Fraisse, B., Stievano, L., Monconduit, L. & Sougrati, M. T. Carbon-coated FePO4 nanoparticles as stable cathode for Na-ion batteries: A promising full cell with a Na15Pb4 anode. *Electrochim. Acta* **409**, 139997 (2022).
128. Ahuja, V., Singh, S., Vengarathody, R. & Senguttuvan, P. Room-Temperature Synthesis and Stable Na-ion Storage Performance of Two-Dimensional Mixed Lead-Bismuth Oxychloride. *J. Phys. Chem. C* **125**, 17622–17628 (2021).
129. Zou, H., Gratz, E., Apelian, D. & Wang, Y. A novel method to recycle mixed cathode materials for lithium ion batteries. *Green Chem.* **15**, 1183 (2013).
130. Wang, H. & Whitacre, J. F. Direct Recycling of Aged LiMn2O4 Cathode Materials used in Aqueous Lithium-ion Batteries: Processes and Sensitivities. *Energy Technol.* **6**, 2429–2437 (2018).
131. Kim, D. S. *et al.* Simultaneous separation and renovation of lithium cobalt oxide from the cathode of spent lithium ion rechargeable batteries. *J. Power Sources* **132**, 145–149 (2004).
132. Weng, Y., Xu, S., Huang, G. & Jiang, C. Synthesis and performance of Li[(Ni1/3Co1/3Mn1/3)1−xMgx]O2 prepared from spent lithium ion batteries. *J. Hazard. Mater.* **246**, 163–172 (2013).
133. Kasukabe, T. *et al.* Beads-Milling of Waste Si Sawdust into High-Performance Nanoflakes for Lithium-Ion Batteries. *Sci. Rep.* **7**, 42734 (2017).
134. Naskar, A. K. *et al.* Tailored recovery of carbons from waste tires for enhanced performance as anodes in lithium-ion batteries. *RSC Adv.* **4**, 38213 (2014).
135. Soo Jung, D., Ryou, M.-H., Joo Sung, Y., Bin Park, S. & Wook Choi, J. Recycling rice husks for high-capacity lithium battery anodes. *PNAS* **110**, 12229–12234 (2013).
136. Jang, H. D. *et al.* Aerosol-Assisted Extraction of Silicon Nanoparticles from Wafer Slicing Waste for Lithium Ion Batteries. *Sci. Rep.* **5**, 9431 (2015).

137. Ciez, R. E. & Whitacre, J. F. Examining different recycling processes for lithium-ion batteries. *Nat. Sustain.* **2**, 148–156 (2019).
138. Hilger, J. P. Hardening process in ternary lead-antimony-tin alloys for battery grids. *J. Power Sources* **53**, 45–51 (1995).
139. Feliu, S., Otero, E. & Gonzalez, J. A. The effect of ageing on the anodic corrosion of Pb-Sb alloys. *J. Power Sources* **3**, 145–155 (1978).
140. Rocca, E. & Steinmetz, J. Passivation phenomenon of low antimony alloys in deep discharge conditions of lead–acid batteries. *J. Electroanal. Chem.* **543**, 153–160 (2003).
141. Osorio, W. R., Rosa, D. M. & Garcia, A. The roles of cellular and dendritic microstructural morphologies on the corrosion resistance of Pb–Sb alloys for lead acid battery grids. *J. Power Sources* **175**, 595–603 (2008).
142. Okamoto, H. Pb-Sb (Lead-Antimony). *J. Phase Equilibria Diffus.* **32**, 567–567 (2011).
143. Farbod, B. *et al.* Anodes for Sodium Ion Batteries Based on Tin–Germanium–Antimony Alloys. *ACS Nano* **8**, 4415–4429 (2014).
144. Songster, J. & Pelton, A. D. The Na-Sb (sodium-antimony) system. *J. Phase Equilibria* **14**, 250–255 (1993).
145. Plieth, W. *Electrochemistry for Materials Science*. *Electrochemistry for Materials Science* (2008). doi:10.1016/B978-0-444-52792-9.X5001-5.
146. Obrovac, M. N., Christensen, L., Le, D. B. & Dahn, J. R. Alloy Design for Lithium-Ion Battery Anodes. *J. Electrochem. Soc.* **154**, A849 (2007).
147. Sayed, S. Y., Kalisvaart, W. P., Luber, E. J., Olsen, B. C. & Buriak, J. M. Stabilizing Tin Anodes in Sodium-Ion Batteries by Alloying with Silicon. *ACS Appl. Energy Mater.* **3**, 9950–9962 (2020).
148. Li, H., Shi, L., Lu, W., Huang, X. & Chen, L. Studies on Capacity Loss and Capacity Fading of Nanosized SnSb Alloy Anode for Li-Ion Batteries. *J. Electrochem. Soc.* **148**, A915 (2001).
149. Jung, C. *et al.* Metasurface-Driven Optically Variable Devices. *Chem. Rev.* **121**, 13013–13050 (2021).
150. Patil, R. A., Devan, R. S., Liou, Y. & Ma, Y. R. Efficient electrochromic smart windows of one-dimensional pure brookite TiO2 nanoneedles. *Sol. Energy Mater. Sol. Cells* **147**, 240–245 (2016).
151. Ghicov, A. *et al.* TiO2 nanotubes: H+insertion and strong electrochromic effects. *Electrochem. commun.* **8**, 528–532 (2006).
152. Chen, J. Z., Ko, W. Y., Yen, Y. C., Chen, P. H. & Lin, K. J. Hydrothermally processed TiO 2 nanowire electrodes with antireflective and electrochromic properties. *ACS Nano* **6**, 6633–6639 (2012).
153. Dinh, N. N., Oanh, N. T. T., Long, P. D., Bernard, M. C. & Goff, A. H. Le. Electrochromic properties of TiO2 anatase thin films prepared by a dipping sol-gel method. *Thin Solid Films* **423**, 70–76 (2003).
154. Devlin, R. C., Khorasaninejad, M., Chen, W. T., Oh, J. & Capasso, F. Broadband high-efficiency dielectric metasurfaces for the visible spectrum. *Proc. Natl. Acad. Sci.* **113**, 10473–10478 (2016).
155. Khorasaninejad, M. *et al.* Visible Wavelength Planar Metalenses Based on Titanium Dioxide. *IEEE J. Sel. Top. Quantum Electron.* **23**, 43–58 (2017).
156. Khorasaninejad, M. *et al.* Metalenses at visible wavelengths: Diffraction-limited focusing and subwavelength resolution imaging. *Science (80-.).* **352**, 1190–1194 (2016).
157. Huang, Y., Xu, H., Lu, Y. & Chen, Y. All-Dielectric Metasurface for Achieving Perfect Reflection at Visible Wavelengths. *J. Phys. Chem. C* **122**, 13 (2018).
158. Koirala, I., Lee, S. & Choi, D. Highly transmissive subtractive color filters based on an all-dielectric metasurface incorporating TiO2 nanopillars. *Opt. Express* **26**, 18320 (2018).
159. Chen, W. T. *et al.* A broadband achromatic metalens for focusing and imaging in the visible. *Nat. Nanotechnol.* **13**, 220–226 (2018).
160. Wu, Y., Yang, W., Fan, Y., Song, Q. & Xiao, S. TiO2 metasurfaces: From visible planar photonics to photochemistry. *Sci. Adv.* **5**, eaax0939 (2019).
161. Zakharova, G. S. *et al.* Anatase nanotubes as an electrode material for lithium-ion batteries. *J. Phys. Chem. C* **116**, 8714–8720 (2012).
162. Lim, E., Shim, H., Fleischmann, S. & Presser, V. Fast and stable lithium-ion storage kinetics of anatase titanium dioxide/carbon onion hybrid electrodes. *J. Mater. Chem. A* **6**, 9480–9488 (2018).
163. Ortiz, G. F. *et al.* TiO2 nanotubes manufactured by anodization of Ti thin films for on-chip Li-ion 2D microbatteries. *Electrochim. Acta* **54**, 4262–4268 (2009).
164. Xu, J., Jia, C., Cao, B. & Zhang, W. F. Electrochemical properties of anatase TiO2 nanotubes as an anode material for lithium-ion batteries. *Electrochim. Acta* **52**, 8044–8047 (2007).
165. Liu, Y. & Yang, Y. Recent Progress of TiO 2-Based Anodes for Li Ion Batteries. *J. Nanomater.* **2016**,

(2016).
166. Wagemaker, M., van de Krol, R., Kentgens, A. P. M., van Well, A. A. & Mulder, F. M. Two Phase Morphology Limits Lithium Diffusion in TiO 2 (Anatase): A 7 Li MAS NMR Study. *J. Am. Chem. Soc.* **123**, 11454–11461 (2001).
167. Cava, R. J., Murphy, D. W., Zahurak, S., Santoro, A. & Roth, R. S. The crystal structures of the lithium-inserted metal oxides Li0.5TiO2 anatase, LiTi2O4 spinel, and Li2Ti2O4. *J. Solid State Chem.* **53**, 64–75 (1984).
168. Nuspl, G., Yoshizawa, K. & Yamabe, T. Lithium intercalation in TiO2 modifications. *J. Mater. Chem.* **7**, 2529–2536 (1997).
169. Wagemaker, M. *et al.* The Influence of Size on Phase Morphology and Li-Ion Mobility in Nanosized Lithiated Anatase TiO2. *Chem. - A Eur. J.* **13**, 2023–2028 (2007).
170. Shen, K., Chen, H., Klaver, F., Mulder, F. M. & Wagemaker, M. Impact of particle size on the non-equilibrium phase transition of lithium-inserted anatase TiO2. *Chem. Mater.* **26**, 1608–1615 (2014).
171. Atherton, P. D., Reay, N. K., Ring, J. & Hicks, T. R. Tunable Fabry-Perot Filters. *Opt. Eng.* **20**, 69–76 (1981).
172. Bozhevolnyi, S. I. Effective-index modeling of channel plasmon polaritons. *Opt. Express* **14**, 9467 (2006).
173. Moreau, A. *et al.* Controlled-reflectance surfaces with film-coupled colloidal nanoantennas. *Nature* vol. 492 86–89 (2012).
174. Zhao, M. *et al.* Investigation of the optical properties of LiTi_2O_4 and Li_4Ti_5O_12 spinel films by spectroscopic ellipsometry. *Opt. Mater. Express* **6**, 3366 (2016).
175. Johnson, P. B. & Christy, R. W. Optical constants of transition metals: Ti, V, Cr, Mn, Fe, Co, Ni, and Pd. *Phys. Rev. B* **9**, 5056–5070 (1974).
176. Johnson, P. B. & Christy, R. W. Optical Constants of the Noble Metals. *Phys. Rev. B* **6**, 4370 (1972).
177. Green, M. A. Self-consistent optical parameters of intrinsic silicon at 300 K including temperature coefficients. *Sol. Energy Mater. Sol. Cells* **92**, 1305–1310 (2008).
178. Querry, M. R. *Optical Constants*. https://apps.dtic.mil/sti/citations/ADA158623 (1985).
179. Mati, H., Pongpan, C. & Pichet, L. A spectroscopic ellipsometry study of TiO2 thin films prepared by dc reactive magnetron sputtering: Annealing temperature effect. *Chinese Phys. Lett.* **24**, 1505–1508 (2007).
180. Eiamchai, P., Chindaudom, P., Pokaipisit, A. & Limsuwan, P. A spectroscopic ellipsometry study of TiO2 thin films prepared by ion-assisted electron-beam evaporation. *Curr. Appl. Phys.* **9**, 707–712 (2009).
181. Wagemaker, M., Lützenkirchen-Hecht, D., Van Well, A. A. & Frahm, R. Atomic and electronic bulk versus surface structure: Lithium intercalation in anatase TiO2. *J. Phys. Chem. B* **108**, 12456–12464 (2004).
182. Giannozzi, P. *et al.* Quantum ESPRESSO toward the exascale. *J. Chem. Phys.* **152**, 154105 (2020).
183. Wagemaker, M., Kearley, G. J., Van Well, A. A., Mutka, H. & Mulder, F. M. Multiple Li positions inside oxygen octahedra in lithiated TiO2 anatase. *J. Am. Chem. Soc.* **125**, 840–848 (2003).
184. Weirich, T. E., Winterer, M., Seifried, S., Hahn, H. & Fuess, H. Rietveld analysis of electron powder diffraction data from nanocrystalline anatase, TiO2. *Ultramicroscopy* **81**, 263–270 (2000).
185. Hu, Z. & Metiu, H. Choice of U for DFT+ U calculations for titanium oxides. *J. Phys. Chem. C* **115**, 5841–5845 (2011).
186. Samat, M. H., Ali, A. M. M., Taib, M. F. M., Hassan, O. H. & Yahya, M. Z. A. Hubbard U calculations on optical properties of 3d transition metal oxide TiO2. *Results Phys.* **6**, 891–896 (2016).
187. Marini, A., Hogan, C., Grüning, M. & Varsano, D. yambo: An ab initio tool for excited state calculations. *Comput. Phys. Commun.* **180**, 1392–1403 (2009).
188. Södergren, S. *et al.* Lithium intercalation in nanoporous anatase TiO2 studied with XPS. *J. Phys. Chem. B* **101**, 3087–3090 (1997).
189. Mansencal, T. *et al.* Colour. (2020).
190. Mathews, N. R., Morales, E. R., Cortés-Jacome, M. A. & Toledo Antonio, J. A. TiO2 thin films – Influence of annealing temperature on structural, optical and photocatalytic properties. *Sol. Energy* **83**, 1499–1508 (2009).
191. Pitna Laskova, B., Kavan, L., Zukalova, M., Mocek, K. & Frank, O. In situ Raman spectroelectrochemistry as a useful tool for detection of TiO2(anatase) impurities in TiO2(B) and TiO2(rutile). *Monatshefte fur Chemie* **147**, 951–959 (2016).
192. Frank, O. *et al.* Raman spectra of titanium dioxide (anatase, rutile) with identified oxygen isotopes (16, 17, 18). *Phys. Chem. Chem. Phys.* **14**, 14567–14572 (2012).
193. Niilisk, A. *et al.* Structural study of TiO2 thin films by micro-Raman spectroscopy. *Cent. Eur. J. Phys.* **4**,

105–116 (2006).
194. Macrae, C. F. *et al.* Mercury 4.0: from visualization to analysis, design and prediction. *urn:issn:1600-5767* **53**, 226–235 (2020).
195. Iatsunskyi, I. *et al.* Atomic layer deposition TiO2 coated porous silicon surface: Structural characterization and morphological features. *Thin Solid Films* **589**, 303–308 (2015).
196. Van De Krol, R., Goossens, A. & Meulenkamp, E. A. Electrical and optical properties of TiO2 in accumulation and of lithium titanata Li0.5TiO2. *J. Appl. Phys.* **90**, 2235–2242 (2001).
197. Lee, Y. *et al.* Full-Color-Tunable Nanophotonic Device Using Electrochromic Tungsten Trioxide Thin Film. *Nano Lett.* **20**, 6084–6090 (2020).
198. Wang, Z. *et al.* Towards full-colour tunability of inorganic electrochromic devices using ultracompact fabry-perot nanocavities. *Nat. Commun.* **11**, 302 (2020).
199. Zhu, J., Feng, J., Lu, L. & Zeng, K. In situ study of topography, phase and volume changes of titanium dioxide anode in all-solid-state thin film lithium-ion battery by biased scanning probe microscopy. *J. Power Sources* **197**, 224–230 (2012).
200. van de Krol, R., Goossens, A. & Schoonman, J. Spatial Extent of Lithium Intercalation in Anatase TiO 2. *J. Phys. Chem. B* **103**, 7151–7159 (1999).
201. Kim, Y. *et al.* Phase Modulation with Electrically Tunable Vanadium Dioxide Phase-Change Metasurfaces. *Nano Lett.* **19**, 3961–3968 (2019).
202. Gholipour, B., Zhang, J., MacDonald, K. F., Hewak, D. W. & Zheludev, N. I. An All-Optical, Non-volatile, Bidirectional, Phase-Change Meta-Switch. *Adv. Mater.* **25**, 3050–3054 (2013).
203. Hosseini, P., Wright, C. D. & Bhaskaran, H. An optoelectronic framework enabled by low-dimensional phase-change films. *Nature* **511**, 206–211 (2014).
204. Kavan, L., Grätzel, M., Gilbert, S. E., Klemenz, C. & Scheel, H. J. Electrochemical and photoelectrochemical investigation of single-crystal anatase. *J. Am. Chem. Soc.* **118**, 6716–6723 (1996).
205. Lunell, S., Stashans, A., Ojamäe, L., Lindström, H. & Hagfeldt, A. Li and Na diffusion in TiO2 from quantum chemical theory versus electrochemical experiment. *J. Am. Chem. Soc.* **119**, 7374–7380 (1997).
206. Moitzheim, S., De Gendt, S. & Vereecken, P. M. Investigation of the Li-Ion Insertion Mechanism for Amorphous and Anatase TiO 2 Thin-Films. *J. Electrochem. Soc.* **166**, A1–A9 (2019).
207. Pors, A. & Bozhevolnyi, S. I. Gap plasmon-based phase-amplitude metasurfaces: material constraints [Invited]. *Opt. Mater. Express* **5**, 2448 (2015).
208. Bozhevolnyi, S. I. & Søndergaard, T. General properties of slow-plasmon resonant nanostructures: nano-antennas and resonators. *Opt. Express* **15**, 10869 (2007).
209. Haque, S. M. *et al.* Plasmonic effect of diffused Ag nanoparticles in EB evaporated Ag/TiO2 bilayer thin films and role of oxygen pressure. *J. Alloys Compd.* **849**, 156553 (2020).
210. Zuo, J., Rao, J. & Eggeler, G. Interface reactions of Ag@TiO2 nanocomposite films. *Mater. Chem. Phys.* **145**, 90–98 (2014).
211. Ruiz-Clavijo, A. *et al.* Engineering a Full Gamut of Structural Colors in All-Dielectric Mesoporous Network Metamaterials. *ACS Photonics* **5**, 2120–2128 (2018).
212. Daqiqeh Rezaei, S. *et al.* Nanophotonic Structural Colors. *ACS Photonics* vol. 8 18–33 (2021).
213. Johnson, S. G. *et al.* Perturbation theory for Maxwell's equations with shifting material boundaries. *Phys. Rev. E* **65**, 066611 (2002).
214. Shaltout, A. M., Shalaev, V. M. & Brongersma, M. L. Spatiotemporal light control with active metasurfaces. *Science* vol. 364 648 (2019).
215. Eaves-Rathert, J. *et al.* Dynamic Color Tuning with Electrochemically Actuated TiO2 Metasurfaces. *Nano Lett.* **22**, 1626–1632 (2022).
216. Feigenbaum, E., Diest, K. & Atwater, H. A. Unity-order index change in transparent conducting oxides at visible frequencies. *Nano Lett.* **10**, 2111–2116 (2010).
217. Dahlman, C. J. *et al.* Electrochemically Induced Transformations of Vanadium Dioxide Nanocrystals. *Nano Lett* **16**, 2 (2016).
218. Yu, N. & Capasso, F. Flat optics with designer metasurfaces. *Nature Materials* vol. 13 139–150 (2014).
219. Khorasaninejad, M. *et al.* Visible Wavelength Planar Metalenses Based on Titanium Dioxide. *IEEE J. Sel. Top. Quantum Electron.* **23**, 43–58 (2017).
220. Devlin, R. C., Khorasaninejad, M., Chen, W. T., Oh, J. & Capasso, F. Broadband high-efficiency dielectric metasurfaces for the visible spectrum. *Proc. Natl. Acad. Sci.* **113**, 10473–10478 (2016).
221. Khorasaninejad, M. *et al.* Metalenses at visible wavelengths: Diffraction-limited focusing and subwavelength resolution imaging. *Science (80-.).* **352**, 1190–1194 (2016).

222. Checcucci, S. *et al.* Multifunctional Metasurfaces Based on Direct Nanoimprint of Titania Sol–Gel Coatings. *Adv. Opt. Mater.* **7**, 1801406 (2019).
223. Li, S. Q. *et al.* Phase-only transmissive spatial light modulator based on tunable dielectric metasurface. *Science (80-.).* **364**, 1087–1090 (2019).
224. Wu, Y., Yang, W., Fan, Y., Song, Q. & Xiao, S. TiO 2 metasurfaces: From visible planar photonics to photochemistry. *Sci. Adv.* **5**, eaax0939 (2019).
225. Kavan, L., Gra, M., Gilbert, S. E., Klemenz, C. & Scheel, H. J. Electrochemical and Photoelectrochemical Investigation of Single-Crystal Anatase.
226. Zhang, A. *et al.* Electrochemical Reductive Doping and Interfacial Impedance of TiO2 Nanotube Arrays in Aqueous and Aprotic Solvents. *J. Electrochem. Soc.* **164**, H91 (2017).
227. Pelouchova, H., Janda, P., Weber, J. & Kavan, L. Charge transfer reductive doping of single crystal TiO2 anatase. *J. Electroanal. Chem.* **566**, 73–83 (2004).
228. Berger, T., Lana-Villarreal, T., Monllor-Satoca, D. & Gómez, R. Charge transfer reductive doping of nanostructured TiO2 thin films as a way to improve their photoelectrocatalytic performance. *Electrochem. commun.* **8**, 1713–1718 (2006).
229. Zukalova, M., Bousa, M., Bastl, Z., Jirka, I. & Kavan, L. Electrochemical Doping of Compact TiO2 Thin Layers. *J. Phys. Chem. C* **118**, 25970–25977 (2014).
230. Joost, U. *et al.* Reversible Photodoping of TiO2 Nanoparticles for Photochromic Applications. *Chem. Mater.* **30**, 8968–8974 (2018).
231. Kormann, C., Bahnemann, D. W. & Hoffmann, M. R. Preparation and Characterization of Quantum-Size Titanium Dioxide. *J. Phys. Chem* **92**, 5196–5201 (1988).
232. Castellano, F. N., Stipkala, J. M., Friedman, L. A. & Meyer, G. J. Spectroscopic and excited-state properties of titanium dioxide gels. *Annu. Rev. Mater. Sci* **6**, 422 (1994).
233. Karst, J. *et al.* Electrically switchable metallic polymer nanoantennas. *Science (80-.).* **374**, 612–616 (2021).
234. Nagatsuka, N., Wilde, M. & Fukutani, K. Hydrogenation and hydrogen diffusion at the anatase TiO2(101) surface. *J. Chem. Phys.* **152**, 074708 (2020).
235. Prathapani, S. *et al.* TiO2 colloid-based compact layers for hybrid lead halide perovskite solar cells. *Appl. Mater. Today* **7**, 112–119 (2017).
236. Choi, W., Termin, A. & Hoffmann, M. R. The role of metal ion dopants in quantum-sized TiO2: Correlation between photoreactivity and charge carrier recombination dynamics. *J. Phys. Chem.* **98**, 13669–13679 (1994).
237. Lyon, L. A. & Hupp, J. T. Energetics of the Nanocrystalline Titanium Dioxide/Aqueous Solution Interface: Approximate Conduction Band Edge Variations between H 0 = −10 and H - = +26. *J. Phys. Chem. B* **103**, 4623–4628 (1999).
238. Valentin, C. Di & Fittipaldi, D. Hole Scavenging by Organic Adsorbates on the TiO2 Surface: A DFT Model Study. *J. Phys. Chem. Lett.* **4**, 1901–1906 (2013).
239. Luttrell, T. *et al.* Why is anatase a better photocatalyst than rutile? - Model studies on epitaxial TiO2 films. *Sci. Reports 2014 41* **4**, 1–8 (2014).
240. Manthiram, A., Vadivel Murugan, A., Sarkar, A. & Muraliganth, T. Nanostructured electrode materials for electrochemical energy storage and conversion. *Energy Environ. Sci.* **1**, 621–638 (2008).
241. Brus, L. Electronic wave functions in semiconductor clusters: Experiment and theory. *J. Phys. Chem.* **90**, 2555–2560 (1986).
242. Fox, M. *Optical Properties of Solids*. (Oxford University Press, 2010).
243. Zhang, Z., Hedhili, M. N., Zhu, H. & Wang, P. Electrochemical reduction induced self-doping of Ti3+ for efficient water splitting performance on TiO2 based photoelectrodes. *Phys. Chem. Chem. Phys.* **15**, 15637–15644 (2013).
244. Zuo, F. *et al.* Self-doped Ti3+ enhanced photocatalyst for hydrogen production under visible light. *J. Am. Chem. Soc.* **132**, 11856–11857 (2010).
245. Vaalma, C., Buchholz, D., Weil, M. & Passerini, S. A cost and resource analysis of sodium-ion batteries. *Nat. Rev. Mater.* **3**, 18013 (2018).
246. Shterenberg, I., Salama, M., Gofer, Y., Levi, E. & Aurbach, D. The challenge of developing rechargeable magnesium batteries. *MRS Bull.* **39**, 453–460 (2014).
247. Song, J., Sahadeo, E., Noked, M. & Lee, S. B. Mapping the Challenges of Magnesium Battery. *J. Phys. Chem. Lett.* **7**, 1736–1749 (2016).
248. Abraham, K. M. How Comparable Are Sodium-Ion Batteries to Lithium-Ion Counterparts? *ACS Energy*

Lett. **5**, 3544–3547 (2020).
249. Cohn, A. P., Muralidharan, N., Carter, R., Share, K. & Pint, C. L. Anode-Free Sodium Battery through in Situ Plating of Sodium Metal. *Nano Lett.* **17**, 1296–1301 (2017).
250. Tan, D. H. S. *et al.* Sustainable design of fully recyclable all solid-state batteries. *MRS Energy Sustain.* **7**, (2020).
251. Thyagarajan, K., Sokhoyan, R., Zornberg, L. & Atwater, H. A. Millivolt Modulation of Plasmonic Metasurface Optical Response via Ionic Conductance. *Adv. Mater.* **29**, 1701044 (2017).
252. Wang, G., Chen, X., Liu, S., Wong, C. & Chu, S. Mechanical Chameleon through Dynamic Real-Time Plasmonic Tuning. *ACS Nano* **10**, 1788–1794 (2016).
253. Peng, J. *et al.* Scalable electrochromic nanopixels using plasmonics. *Sci. Adv.* **5**, eaaw2205 (2019).
254. Xiong, K. *et al.* Switchable Plasmonic Metasurfaces with High Chromaticity Containing only Abundant Metals. *Nano Lett.* **17**, 7033–7039 (2017).
255. Xu, T. *et al.* High-contrast and fast electrochromic switching enabled by plasmonics. *Nat. Commun.* **7**, 10479 (2016).
256. König, T. A. F. *et al.* Electrically tunable plasmonic behavior of nanocube-polymer nanomaterials induced by a redox-active electrochromic polymer. *ACS Nano* **8**, 6182–6192 (2014).
257. Stockhausen, V. *et al.* Giant plasmon resonance shift using poly(3,4-ethylenedioxythiophene) Electrochemical switching. *J. Am. Chem. Soc.* **132**, 10224–10226 (2010).
258. Wu, J. *et al.* Flexible Electrochromic V 2 O 5 Thin Films with Ultrahigh Coloration Efficiency on Graphene Electrodes . *J. Electrochem. Soc.* **165**, D183–D189 (2018).
259. Zanotto, S. *et al.* Metasurface Reconfiguration through Lithium-Ion Intercalation in a Transition Metal Oxide. *Adv. Opt. Mater.* **5**, 1600732 (2017).
260. Zanotto, S. *et al.* Chiral Metasurfaces: Metasurface Reconfiguration through Lithium-Ion Intercalation in a Transition Metal Oxide (Advanced Optical Materials 2/2017). *Adv. Opt. Mater.* **5**, (2017).
261. Wang, Z. *et al.* Towards full-colour tunability of inorganic electrochromic devices using ultracompact fabry-perot nanocavities. *Nat. Commun.* **11**, 302 (2020).
262. Li, Y., Van De Groep, J., Talin, A. A. & Brongersma, M. L. Dynamic Tuning of Gap Plasmon Resonances Using a Solid-State Electrochromic Device. *Nano Lett.* **19**, 7988–7995 (2019).